ÉCOLE DOCTORALE
ENERGIE, MATERIAUX, SCIENCES DE LA TERRE ET DE L'UNIVERS

Laboratoire GREMI / Laboratoire PLASMANT

THÈSE EN COTUTELLE INTERNATIONALE présentée par :

Sotheara CHUON

soutenue le : 11 décembre 2019

pour obtenir le grade de :
Docteur de l'université d'Orléans
et de l'Université d'Anvers

Discipline : Physique

Simulation numérique multi-échelles du procédé de dépôt par pulvérisation cathodique magnétron

THÈSE dirigée par :

Jean-Marc BAUCHIRE	Professeur, GREMI, Université d'Orléans
Pascal BRAULT	DR CNRS, HDR, GREMI, Université d'Orléans / CNRS
Erik NEYTS	Professeur, PLASMANT, Université d'Anvers

JURY :

Jean-Marc BAUCHIRE	Professeur, GREMI, Université d'Orléans	
Pascal BRAULT	DR CNRS, HDR, GREMI, Université d'Orléans / CNRS	
Arnaud DELCORTE	Professeur, BSMA, Université Catholique de Louvain	
Khaled HASSOUNI	Professeur, LSPM, Université Paris-Nord	**Président du jury**
Stephanos KONSTANTINIDIS	Professeur, CHIPS, Université de Mons	
Erik NEYTS	Professeur, PLASMANT, Université d'Anvers	

Remerciements

Les travaux de cette thèse ont été réalisés au sein des groupes de recherche GREMI (Groupe de Recherche sur l'Energétique des Milieux Ionisés) à l'Université d'Orléans et PLASMANT (Plasma, Laser Ablation & Surface Modelling ANTwerp) à l'Université d'Anvers. C'est pourquoi je souhaiterais tout d'abord remercier Chantal LEBORGNE, Anne-Lise THOMANN, directrices du GREMI durant ma thèse, et également Annemie BOGAERTS, directrice de PLASMANT, de m'avoir accueillie et permis d'intégrer les laboratoires pour ces 4 années.

J'aimerais remercier mes directeurs de thèse, Jean-Marc BAUCHIRE, Pascal BRAULT et Erik NEYTS de m'avoir donné la clef de cette grande Aventure franco-belge et sans qui je n'aurais pu réaliser ces travaux. UN GRAND MERCI pour leurs conseils, leur aide et leur soutien durant toutes ces années qui m'ont été tellement enrichissantes.

Je souhaiterais également remercier Khaled HASSOUNI, Stephanos KONSTANTINIDIS et Arnaud DELCORTE d'avoir accepté de faire partie des membres du jury, pour leurs questions et remarques qui ont notamment permis d'enrichir ce manuscrit.

Merci aux membres du GREMI ainsi que de PLASMANT pour leur accueil et les moments que nous avons pu passer. Merci à Sylvie JAUFFRION, Corinne DELHAYE, Fabiana QUIROZ, Luc VAN'T DACK et Karel VENKEN pour toute les aides qu'ils ont pu m'apporter, à Eric MILLON, Sophie RAGER, Toufik BOUSHAKI, Nuno CERQUEIRA et Nadia PELLERIN pour les 3 années d'enseignement.

Je n'aurais, je pense, jamais pu arriver jusque là sans avoir également travaillé avec Olivier AUBRY, Dunpin HONG et Hervé RABAT. Merci ! Et encore MERCI à Nuno CERQUEIRA, qui a cru en moi et m'a permis de tracer mon chemin.

Enfin, pour tout ce que nous avons partagé que ce soit au bureau, ou autour d'un bon café, d'une fondue, de sushis, d'un cheese naan, d'un tawouk, d'une bonne bière à la cerise, ou d'un ballon lors de rares mercredis pour ma part, d'un escape game, ou d'un défi de rubiks cube … Pour toutes nos discussions et nos moments de rire, de peur, de joie et de confidence … « Poupipoupipoupidou » … UN GRAND GRAND MERCI à Abdou, Vincent, Fadi, Ronan, Gaëlle, Pierre, Edouard, Floriane, Arnaud, Caro, Yasmine, Safa, Vanessa, Xavier, Audoin, Vini, Cédric, Ana, Jiashu, Martin, William, Robin (je n'oublie pas les poissons), Augusto, Erik, Azadeh, Olga, Soso, Marie-Lyne, Jenifer, Noussaiba, Antoine, Nicolas, Thomas et Hervé.

Merci à Kristof, Stijn, Yannick et Jonas pour m'avoir accueillie dans leur bureau cette dernière année à Anvers et à Irina pour la visite de la ville à vélo.

Pour terminer cette page, j'aimerais remercier mes amis, plus particulièrement ma Rajae, Mamadou, Babacar, Ali et Elodie, ainsi que ma Famille et encore une fois, mon Amour, pour tout le soutien qu'ils m'ont apporté et qu'ils m'apportent encore aujourd'hui. Merci pour tout ♥

Summary

I. Introduction

1. Context

Since the 19th century, the different effects obtained by the application of electricity in a gas have been studied. It was in 1928 when the 'Plasma' term was first introduced in physics by Langmuir and Tonk to describe ionized gas in an electrical discharge [1]. Indeed, plasmas are composed by a collection of different particles such as electrons, free radicals, positive and negative ions, photons, free atoms and molecules in neutral and excited states which can makes one think of an analogy with the blood complexity.

These unique properties make it the fourth state of matter after solid, liquid and gaseous states. Plasmas are known as 99% of the matter in the Universe. It concerns natural plasmas which are stars, polar lights or lightning for example. In industries and in laboratory, artificial plasmas are applied. They are also mainly known as electrical or gas discharges [2]. These electrical discharges consist on supplying a sufficient energy in neutral gas to extract one or many electrons from atoms to be ionized. The charged particles contained in the plasma and their interactions make it very interesting and allow a wide variety of applications in different domains such as biomedical [3, 4], environmental [5–7] or agricultural [8]. In industries plasma processes were also developed for surface treatments [9].

Plasmas can be divided into two groups according electron temperature [2]. In one part, thermal plasmas are characterized by a unique temperature for electron and heavy particles. In other part, for non-thermal plasmas, electron temperature is much higher than the heavy particles one. Properties of non-thermal plasmas lead to many techniques and applications like

sputtering techniques for surface treatments. Sputter deposition process is part of Physical Vapour Deposition (PVD) [10] methods employed to synthesize thin films or coatings for applications in different fields like mechanic, optic, electronic, ... , for data storage, or also simply for decoration [11–15]. This method consists to produce a thin film or a coating on a surface material, which will be named the 'substrate', to give it properties of the sputtered material, the 'target'. Actually, the term 'sputtering' is defined by two aspects which are the erosion of the target surface, both physical and chemically assisted, by particle bombardment (sputter emission or sputter erosion) and the deposition of sputtered material onto the substrate (sputter deposition) [16].

There is a lot of sputtering sources as diode sputtering, triode, magnetron sputtering or ions beam sources [17, 18]. However, magnetron sputtering has many advantages for deposition.

This process being therefore the main technology used by industries for thin films deposition, it is interesting to investigate magnetron discharges. To better understand discharge phenomena, theoretical models were developed [19]. Thanks to the performance of computers, numerical simulations associated with experimental results become a reliable tool. Moreover, numerical simulations allow system behaviour prediction and thus to find optimal operating conditions for industrial processes. Consequently, using numerical simulations gives the possibility to reduce experimental testing and design costs.

2. Sputtering and Magnetron Sputtering

Sputtering phenomenon is in general defined by the solids surface erosion due to energetic particle bombardment. It was first observed in 1853 by Grove with the formation of a thin cathode's material layer onto the walls of a glass discharge tube during the establishment of an electrical discharge in vacuum [11, 20]. Then, several observations were made to understand sputtering [21, 22]. Thereby diode sputtering was developed.

Many materials were deposited by this technique. Nevertheless, low deposition rates, low ionization efficiency in the plasma and high substrate heating effects limit it. For some applications, the process was not economical because of the slowness of the deposition.

In 1936, Penning proposed to add a magnetic field, based on Hull works in 1921, to improve the process [23, 24]. It was in 1974, when a planar magnetron with closed magnetic field lines was invented by Chapin and made the possibility to overcome these limitations [25–27].

Indeed, the addition of a magnetic field allows higher collisions, an increase of deposition velocity and also the synthesis of dense coating by using low pressures [11, 28, 29].

2.1. Mechanism

The sputtering deposition mechanism [28], represented in **Figure 1**, consists in applying an electrical field between two electrodes in a low pressure gas, often composed of argon (Ar). Thus, pre-existing electrons are accelerated from the negative biased target to ionize the gas, neutral-electron collisions **(1)** create positive argon ions **(2)** which are accelerated and impact the target **(3)** to release target atoms **(4)** which fly to coat a substrate **(5)**. Secondary electrons are created by the ion impacts toward the target and make new collisions with neutrals. Secondary electrons then allow the discharge to be maintained by an avalanche process.

Coatings can be produced by sputtered atoms or also by growing molecules or clusters issued from the target sputtering during the transport to the substrate. For a magnetron sputtering source, a magnetic device is placed below the target and creates a magnetic field which confines electrons just above the cathode by closed electron-drift currents $\vec{E} \times \vec{B}$. Thus, it allows an increase of electrons collisions frequency and so an increase of ion density closed to the biased target.

As the ionization increases during magnetron sputtering, comparing to a basic sputtering system, the discharge can be maintained at lower operating pressures (typically, $P = 10^{-3}$ mbar compared to 10^{-2} mbar) and lower operating voltages (typically, $V_c =$ -500 V compared to -2 to -3 kV) [30].

Planar magnetron is one of the most common designs of magnetron sputtering device as in the following scheme.

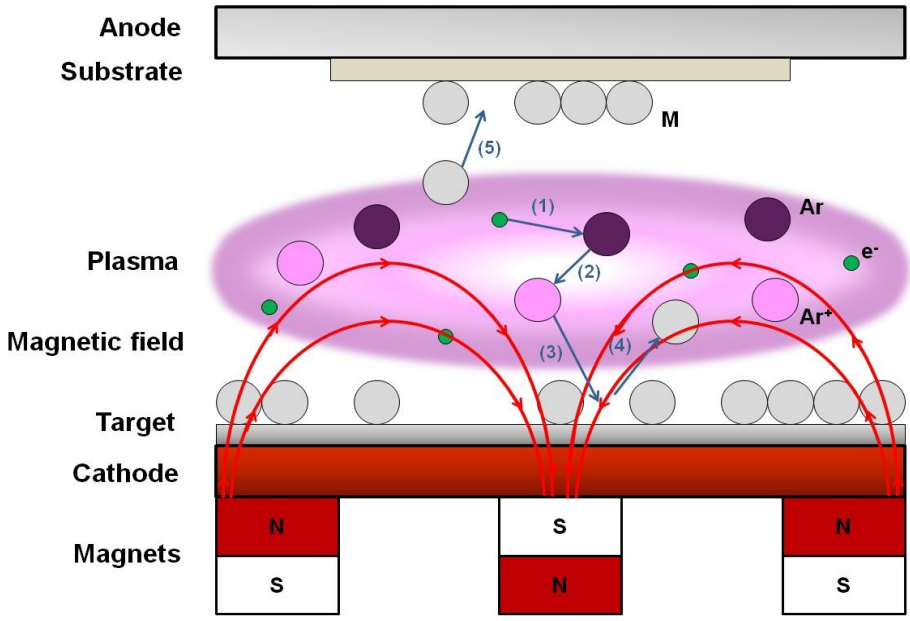

Figure 1: Magnetron sputtering mechanism. The color spheres of green, purple, pink and grey represent electrons, argon atoms, argon ions and target atoms respectively.

Many sputtering methods have been designed, from this mechanism, in order to improve the synthesis of specific thin films and coatings focused on main goals such as to get higher quality films, higher sputtering and deposition rates, and finally the ability to be scaled-up for industrial applications [31].

Magnetron systems have been introduced and overcome some sputtering techniques limitations as described in the next subsections [18, 32, 33].

2.2.Sputtering Processes

The following table lists the developed sputtering processes from DC diodes.

Process	Main characteristics
Non reactive DC sputtering[17, 18, 28, 31]	▪ Low plasma density ▪ Low ionization efficiency ▪ Low deposition rate ▪ Only conductive target materials
Non reactive RF sputtering[17, 18, 28, 31, 34]	▪ Insulating target material ▪ Dielectric films production with a radio frequency of 13.56 MHz ▪ Deposition rate lower than DC sputtering ▪ Treatment of small areas ▪ High cost for industrial scale
Magnetron sputtering	▪ High electron density ▪ High deposition rate ▪ Dense coating production using low pressure
Reactive sputtering[11, 17, 18, 28, 28, 35–38]	▪ Insulating and dielectric film deposition ▪ Oxide, nitride, carbide or compound films deposition ▪ Stability problems due to an hysteresis behaviour of the process depending on the reactive gas supply ▪ Poisoning target ▪ Arcing effect occurring by high charges accumulation ▪ Disappearing anode effect
Triode sputtering[18, 39]	▪ Increase of electrons density and ionization of a DC diode sputtering system ▪ Contamination of the growing film due to the filament erosion in reactive sputtering ▪ Problem of scaling up for industrial application
Ion Beam-Assisted Deposition (IBAD)[17, 40–45]	▪ Control of the deposition for specific coatings ▪ Slow growth rates ▪ Treatment of small area ▪ Treatment of large area samples thanks to CFUBM (Closed-Field Unbalances Magnetron)
Mid-frequency AC reactive sputtering[18, 37, 46–48]	▪ Typical frequencies between 10 and 100 kHz ▪ Control of the formation of insulating reactive compounds on electrodes ▪ Avoiding the formation of arc by charges accumulation ▪ Increase of the heat of the substrate compare to DC mode due to bombardments of both electrons and ions
Pulsed DC sputtering : Single Magnetron Sputtering (SMS)/Dual Magnetron Sputtering (DMS)[17, 18, 30, 31, 36, 49–51]	▪ Frequencies between 10 and 200 kHz ▪ SMS: - avoiding the accumulation of charges only on the target surface ▪ DMS: - avoiding arcing and prevents disappearing anode problem - high deposition rate for reactive puttering
High power pulsed magnetron (HPPMS) sputtering/High Power Impulse Magnetron Sputtering (HiPIMS)[18, 52–60]	▪ High pulsed target current from a short pulse duration ranging from 1µs to 1 s and frequency lower than 1 kHz ▪ Ultra dense plasma with higher electron density than in DC magnetron sputtering ▪ Higher ion current density and high plasma density ▪ Reduction of the hysteresis effect in reactive sputtering

Table 1: Sputtering processes.

Numerous techniques have been developed in order to improve DC diode sputtering. Triode sputtering adds a heat filament as a source of electrons to increase ionization. In reactive sputtering, the growing film can be contaminated due to the erosion of the filament from interactions with species of the reactive gas. Moreover, the scaling up of the system for industrial application could be a problem due to the thermionic emitter [18]. Magnetron sputtering allows high electron densities, therefore high deposition rates and the production of large area dense coatings using low pressures. The microstructure of the growing film can be controlled by providing added energy to the sputtered atoms from Ion beam-assisted deposition [41, 42]. This technique has main disadvantages as slow growth rate and small-area sample treatment. Insulating and dielectric films can be synthesized by RF sputtering or reactive sputtering. However, the high cost of power supplies limit applications of RF sputtering [31]. Reactive processes showed problems of stability and it was difficult to combine high deposition rate and true stoichiometry of the compound film [18, 28, 37, 38]. Actually, all reactive processes have an hysteresis behaviour depending on the reactive gas supply. A high supply of reactive gas causes reactive compounds which cover the target surface and also the walls of the chamber including the anode. Arcing effect can occur by a high charges accumulation. Therefore, control of reactive gases, AC and pulsed DC sputtering remedy these problems. Nevertheless, the AC mode increases the heat of the substrate due to bombardment of both electrons and ions [18]. High power impulse magnetron sputtering improves pulsed sputtering by using low frequency and allows to increase ionization and to reduce hysteresis effect due to poisoning of the target, thus to operate un stable process condition in reactive sputtering [56–60].

2.3.Magnetron sputtering systems

Planar magnetron was introduced in 1974 by Chapin [18, 26]. Due to the advantages it offered in sputtering, there is always an interest to develop and improve this configuration. Thus, different magnetron sputtering systems have been developed as presented in the table below. Unbalanced Magnetron (UM) was developed by Window and Savvides when they investigated the effect of charge particles fluxes by the variation of the magnet configuration from the Conventional Magnetron (CM) also called balanced magnetron. Thus, there are two type of UM according to the strengthened magnet [18, 41, 45]. Closed-Field Unbalanced Magnetron (CFUBM) uses multiples UM to form a trap for electrons in the plasma.

Compared to a CM, the plasma is less confined inside the target region for an UM and a CFUBM configurations and lead large area treatment as in IBAD [40–42, 45].

Systems	Characteristics
Conventional Magnetron (CM)	▪ Identical inner and outer magnets strength ▪ Closed magnetic field lines ▪ Dense plasma confined inside the target region
Unbalanced Magnetron (UM): Type I/Type II[18, 41, 61]	▪ Type I: - Inner magnet stronger than the outer magnet - Unclosed magnetic field lines from the inner magnet directed towards the chamber walls - Decrease of ions and electrons fluxes to the substrate leading to low ions bombardments ▪ Type II: - Outer magnet stronger than the inner magnet - Unclosed magnetic field lines from outer magnet directed towards the substrate - Increase of ions bombardments on the substrate
Closed-Field Unbalanced Magnetron (CFUBM)[45, 62]	▪ Multiples UM with neighbouring magnetrons of opposite polarity ▪ Closed magnetic field lines in the plasma ▪ Dense plasma
Dual/Multiple magnetrons[30, 32, 42, 49]	▪ Multiple magnetrons (co-planar magnetrons, opposed magnetrons) ▪ Same target material or target of different materials (co-sputtering /co-deposition)

Table 2: Magnetron sputtering configurations.

The use of dual-magnetron or even multiple magnetron systems allows the deposition of high quality coatings, also hard coatings and multiple components coatings according to magnetron targets which can be of a different material [30, 63, 64].

3. Numerical simulation of magnetron sputtering erosion

Nowadays, the development of computer performance makes numerical simulations very widespread. Indeed, numerical simulations are yet much more employed by researchers to explain and to complement experimental results. Furthermore, main advantages of using

numerical simulations are to characterize discharges and predict system behaviour. Thus, it makes possible to optimize processes and hence to reduce design experiment cost.

The important use of magnetron sputtering by industries for the synthesis of thin films today makes it interesting to simulate entirely [65–67].

As defined by Bogaerts and co-workers, a complete simulation of magnetron sputtering includes modelling of magnetic field, magnetron discharge, particle-target interaction and sputtering, transport of sputtered particle through the gas phase, deposition and film growth at the substrate [67]. Finally, this leads to models of magnetron discharge, sputtering erosion and deposition processes.

Many models have been developed in 1D, 2D and 3D, using analytic, continuum or fluid, kinetic, particle, microscopic and also hybrid approaches to understand the physical processes which are involved in the system [68, 69]. These different approaches used to simulate the magnetron discharge and the sputtering erosion, are presented in the following subsections.

3.1. Magnetron discharge

Numerous studies have been carried out to investigate the magnetron sputtering discharge for determination of basic plasma parameters [70–73]. The simulation of magnetron discharge includes the study of the electric potential, the plasma density with non-reactive or reactive gas composed of neutrals and charged particles densities, temperatures and energies distributions in a magnetic field. Different approaches were applied to model the magnetron sputtering discharge such as fluid, kinetic, particle and hybrid.

3.1.1. Magnetic field

Analytical and numerical approaches used to model the magnetic field distribution are based on the equation of the magnetic flux conservation [68, 70, 74, 75].

As presented by Kondo and Nanbu, the magnetic field is defined in the permanents magnets by [70]:

$$B = \mu_0 H + M \tag{I-1}$$

where B is the magnetic flux density, H is the magnetic field, M is the magnetization and μ_0 is the permeability of free space.

The governing equation for the permanent magnets is

$$\frac{1}{\mu_0}\nabla \times B = j_m \tag{I-2}$$

where j_m is the magnetizing current.

$$j_m = \frac{1}{\mu_0}\nabla \times M \tag{I-3}$$

Since $\nabla \cdot B = 0$, the vector potential A can be introduced as:

$$B = \nabla \times A \tag{I-4}$$

Finally, the governing equation can be written as:

$$\frac{1}{\mu_0}\nabla \times (\nabla \times A) = j_m \tag{I-5}$$

3.1.2. Particle approach

The Particle-In-Cell/Monte Carlo Collision (PIC/MCC) is the most common approach to simulate a magnetron discharge.

This particle approach consists on treatment of individual particles as electrons, ions and neutrals represented by ensembles referred to as macroparticles. The trajectories of these macroparticles are calculated according to equations of Newton, in electric field, solved by Poisson's equation, and magnetic field. The particle collisions are described using the technique of Monte Carlo (MC) [76].

The equation of motion of charged particles is given by [70, 74, 77]:

$$m\frac{dv}{dt} = q(E + v \times B) \tag{I-6}$$

where m is the mass, v is the velocity, t is the time, q is the charge, E and B represent respectively the electric field and the magnetic field.

The electric field is obtained by solving the Poisson's equation:

$$\nabla^2\phi = -\frac{\rho}{\epsilon_0} \tag{I-7}$$

$$E = -\nabla\phi \tag{I-8}$$

where ρ is the charge density and ϵ_0 is the permittivity of free space.

The velocity and the position may change depending on whether a collision occurs or not. Thus, assuming a background gas of argon, the collisions between electron and argon atom e^--Ar, including ionizing and elastic collisions and also exciting collisions, and the collisions between argon ion and argon atom Ar^+-Ar, including elastic collision and resonant charge exchange, are considered.

Then, the probability that the e^--Ar collision occurs is given by:

$$P_e(k) = N_A \sigma_k(\varepsilon) \left(\frac{2\varepsilon}{m_e}\right)^{1/2} \Delta t_e \tag{I-9}$$

where k is the number of the event, Δt_e is the electron time step, N_A is the number density of argon gas, σ_k is the e^--Ar collision cross section, ε is the electrons energy and m_e is the electron mass.

The probability of Ar^+-Ar collisions is given by:

$$P_i = 4\pi\beta_\infty^2 \left(\frac{a}{M_A}\right)^{1/2} N_A \Delta t_i \tag{I-10}$$

where Δt_i is the ion time step, β_∞ is the cut-off of the dimensionless impact parameter, M_A is the ion mass and $a = \alpha_d e^2/(32\pi^2\epsilon_0^2)$ where α_d is the polarizability and e is the electronic charge.

Many magnetron discharge models have been performed in 1D, 2D and 3D by PIC/MCC. As in most cited, Van der Straaten and co-workers developed a 1D model of a DC cylindrical post-cathode magnetron discharge [78]. 3D and 2D axisymmetric models of a DC planar magnetron discharge have been studied by Nanbu and Kondo [70, 74, 77]. PIC/MCC simulations of plasma density and potential distribution have also been combined to kinetic simulations to obtain particles velocity information for erosion and deposition, as in works of Shon and Lee [79].

However, the statistic aspect due to MC requires a lot of particles treatment and implies a significant computation time and also computer memory allocation.

3.1.3. Kinetic approach

The kinetic model is based on the resolution of Boltzmann's equation in order to determine particles distribution functions [80–82].

Guimarães and co-workers developed a DC planar magnetron discharge by solving Boltzmann's equation for the Electron Energy Distribution Function (EEDF) in the magnetized region of the discharge, written as [80]:

$$\frac{\partial n(\varepsilon,t)}{\partial t} = -\left[\frac{\partial J_{el}}{\partial \varepsilon}\right]_{e-A} + \left[\frac{\partial J_{el}}{\partial \varepsilon}\right]_{e-e} + J_{exc} + J_{ion} + S + L + P \quad \text{(I-11)}$$

where $n(\varepsilon,t)d\epsilon$ is the number density of electrons having an energy in the range $[\varepsilon, \varepsilon + d\varepsilon]$, t is the time, $\left[\frac{\partial J_{el}}{\partial \varepsilon}\right]_{e-A}$ and $\left[\frac{\partial J_{el}}{\partial \varepsilon}\right]_{e-e}$ correspond respectively to the elastic electron-atom (or electron-molecule) and electron-electron Coulomb collisions, J_{exc} and J_{ion} correspond respectively to the inelastic and ionization collisions, S is the source term, L is the loss term and P takes account of Penning electrons. The term $S(\varepsilon)$ corresponds to the averaged density number of electrons, which leave the cathode and enter in the glow, over the magnetized volume.

The EEDF depends on plasma parameters such as the current, the voltage and the gas pressure. Its solution allows the calculation of ionization and excitation frequencies.

Moreover, this kinetic model was also coupled with a Collisional-Radiative (CR) for an argon plasma by [80]:

$$\frac{dn_i}{dt} = \sum_{j\neq i} n_e n_j C_{ji}^e + \sum_{j>i} n_j A_{ji} - n_i \left[n_e \sum_{j\neq i} C_{ij}^e + n_e C_i^e + \sum_{j<i} A_{ij} + k_p \sum_j n_j + \frac{D_i}{\Lambda^2} \right] \quad \text{(I-12)}$$

where n_i is the density of state i, n_j is the density of state j, n_e is the electron density at time t, C_{ij}^e is the inelastic (or superelastic) electronic collision rate for transition $j \rightarrow i$ (also calculate at time t), C_i^e is the ionization rate for state i, A_{ij} is the transition probability from state i to state j, D_i is the diffusion coefficient for the i state and Λ is the characteristic diffusion length defined by:

$$\Lambda = \left[\frac{\pi^2}{h^2} + \left(\frac{2.405}{R} \right)^2 \right]^{-1/2} \quad \text{(I-13)}$$

where the associate geometry of metastable is approximated to a disc of a radius R and a height h.

$$k_p = 6.4 \times 10^{-10} \times \left(T_g / T_0 \right)^2 \quad \text{(I-14)}$$

where T_g and T_0 are the actual gas temperature and the ambient temperature 300 K respectively.

3.1.4. Fluid approach

The fluid model consists in the treatment of charged particles and neutrals transport by the resolution Boltzmann's equation, continuity (I-15), momentum transfer (I-16) and mean energy transfer (I-17), coupled with Poisson's equation (I-18) [83]:

$$\frac{\partial n_s}{\partial t} + \nabla . \overrightarrow{\Gamma_s} = S_s \tag{I-15}$$

$$m_s n_s \left[\frac{\partial \overrightarrow{v_s}}{\partial t} + (\overrightarrow{v_s} . \nabla)\overrightarrow{v_s}\right] = q_s n_s \left(\vec{E} + \overrightarrow{v_s} \times \vec{B}\right) - \nabla \overrightarrow{\overrightarrow{P_0}} - m_s n_s f_{ms} \overrightarrow{v_s} \left(1 + \frac{S_s}{n_s f_{ms}}\right) \tag{I-16}$$

$$\frac{\partial (n_s \varepsilon_s)}{\partial t} + \nabla . \overrightarrow{\Gamma_{\varepsilon s}} = -\overrightarrow{\Gamma_s} . \vec{E} - \theta_s n_s \tag{I-17}$$

$$\Delta V = -\frac{e}{\varepsilon_0}(n_i - n_e) \tag{I-18}$$

where s is the type of particle ($s = e$ for electron and i for ion), $n_s$is the density, t is time, $\overrightarrow{\Gamma_s}$ is the particles flux, $\overrightarrow{v_s}$ is the velocity, $S_s$is the source term, m_s is the mass, $q_s$is the particle charge, $\vec{E}$ is the electric field, $\vec{B}$ is the magnetic field, $\overrightarrow{\overrightarrow{P_0}}$ is the pressure tensor, f_{ms} is the total momentum transfer frequency for specie s-neutral collisions, $\varepsilon_s$is the mean energy, $\overrightarrow{\Gamma_{\varepsilon s}}$ is the energy flux, θ_s is the energy loss rate for s-neutral collisions, V is the electric potential, e is the constants of elementary charge and ε_0 is the permittivity of free space.

In this approach, electrons and ions are considered as two fluids allowing less computation time than for particle approach. Studies treated the magnetron discharge by fluid approach in 1D as Bradley and Lister [84, 85]. A 2D axisymetric model of DC planar magnetron discharge was also developed by Costin and co-workers [71, 83, 86]. However, Computational Fluid Dynamic (CFD) is not the method of choice by researchers to simulate a magnetron discharge. This can be explained by the effect of an inhomogeneous and strong magnetic field to charged particles. Furthermore, it is also limited for low-pressure magnetron sputtering discharge modelling, due to assumption which must be taken into account for fluid applicability. Fluid model is not valid in low pressures when the discharge characteristic length is exceeded by charged particles mean free path [72, 87]. In fact, although the magnetron discharge uses low pressures, the application of the magnetic field reduces the

effective distance covered by the electrons between two collisions, and allows in some case to fulfill the hydrodynamic hypothesis [83].

3.1.5. Hybrid approach

Numerous models result from the combination of particle and fluid approaches which forms the hybrid model.

The main interest of modelling a magnetron sputtering discharge with a hybrid model is, of course, to reduce computation time drawbacks obtained by PIC/MCC technique. Indeed, as PIC/MCC is very used to describe non-equilibrium process, hybrid model are performed by using particle model, in one part, to treat fast electrons in order to obtain individual movement of highly non-equilibrium electron expression and fluid model, on the other side, to describe ions and bulk electrons for the calculation of charged particles spatial distribution.

This method has been presented in the hybrid models of Shidoji and co-workers [88, 89] also Kolev and Bogaerts [87]. Another method consists in a hybrid model of magnetron discharge in which all the electrons are treated by the particle model and all the ions by the fluid model as studied by Shidoji and Makabe [90], then by Jimenez, Kageyama and their co-workers [69, 91], for example.

3.2.Sputtering

The sputtering phenomenon depends on characteristics of the discharge and chemical and physical properties of the target. Material surfaces can be eroded by particles such as energetic ions, recoil atoms, also electrons and photons according to the nature of the materials of concern (metal, ceramic, polymers, ...). Sputtering experiments have been performed with different geometries in order to study parameters such as ion energy, ion dose, ion-target combination, target temperature, target structure. Most of them were based on sputtering yield measurement according to different methods [92]. The sputtering yield is defined by the ratio of the number of sputtered atoms from the target surface per incident particles, here the ions.

Among several hypotheses concerning the origin of sputter erosion, Stark presented sputtering as a sequence of binary collision events due to one sputtering ion at a time [21, 93]. Thus, sputtering was described as an elastic collision process of single collision then of multiple

collisions which causes a moving target atoms cascade. The multiple collisions cascade can end according to two ways such as a linear cascade and a spike. Finally, this leads to different cases of sputtering events as presented by Sigmund [21] and reported in the **Figure 2**. There are three sputtering situations in this context: the single-knockon regime, the low-density linear cascade and the high-density spike cascade [16, 21, 94, 95]. The single-knockon regime is characterized by the ejection of target atoms which get sufficient energy from sputtering ions to overcome the surface binding forces. In the case of collisions cascade, the recoil atoms get sufficient energy to generate secondary and higher-generation recoils. The linear cascade is characterized by the loss of a recoil atom remaining kinetic energy into heat when its energy reaches the lattice binding energy. The spike cascade defines when alternatively the cascade is so dense and the chance to hit a moving target atom is small.

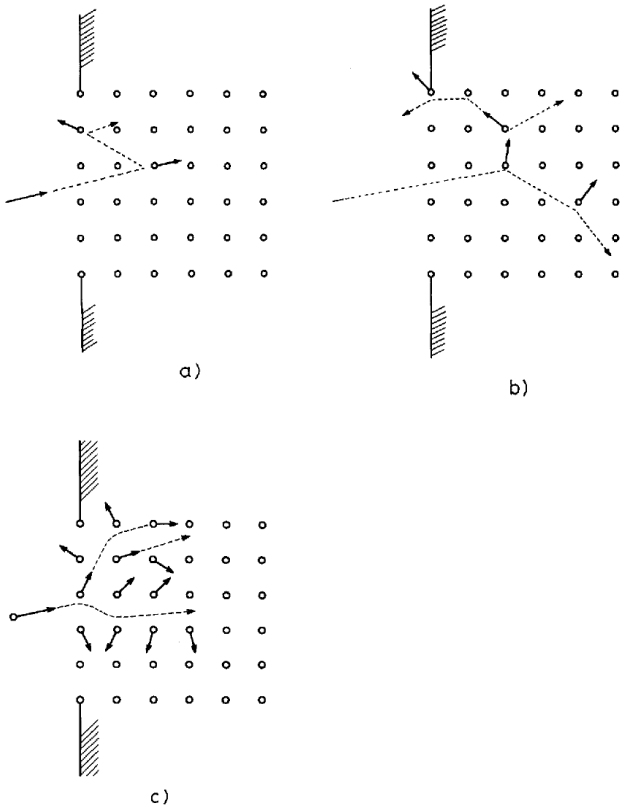

Figure 2: Three regimes of sputtering by elastic collisions, (a) The single-knockon regime. Recoil atoms from ion-target collisions receive sufficiently high energy to get sputtered, but not enough to generate recoil cascades. (b) The linear cascade regime. Recoil atoms from ion-target collisions receive sufficiently high energy to generate recoil cascades. The density of recoil atoms is sufficiently low so that knock-on collisions dominate and collisions between moving atoms are infrequent. (e) The spike regime. The density of recoil atoms is so high that the majority of atoms within a certain volume (the spike volume) are in motion [21]

The theory of collision cascades of nonlinear and linear regimes became a reference for sputtering process description. Works from Sigmund and Thompson allowed an available sputtering transport theory of linear cascade [96].

Sputtering erosion of a surface material is mainly characterized by the sputtering yield calculation [1, 97, 98]. Furthermore, this parameter can be calculated with good accuracy according to the linear collision cascade. Thus, analytical approaches and numerical models of Binary Collision Approximation (BCA) and Molecular Dynamics (MD) models have been developed in order to simulate the two regimes of sputtering and to calculate yields within the frame of the linear collision cascade theory.

3.2.1. Binary collision approximation

The BCA method consists on modelling atomic collision of a sputtering cascade in a solid material characterized as a radiation damage which is approximated by a series of independent binary collisions between two particles, an incident ion and a target atom at rest. In BCA, the moving ion energy loss and the energy transferred to the recoil atom are determined from the conservation of energy and momentum, and the scattering angle of the moving ion and the recoil atom angle are determined from the conservation of angular momentum [99]. Thus, the scattering angle in the center-of-mass system is given by Eckstein and Urbassek by [99]:

$$\theta = \pi - 2p \int_R^\infty \left[r^2 / \sqrt{1 - \frac{V(r)}{E} - \frac{p^2}{r^2}} \right] dr \qquad \text{(I-19)}$$

where p is the impact parameter, $V(r)$ is the interaction potential, E is the kinetic energy of the moving atom, r is the distance between the two colliding atoms and R is the apsis (closest distance) of the collision calculated from [100]:

$$1 - \frac{V(R)}{E_c} - \left(\frac{p}{R}\right)^2 = 0$$

with E_c is the center-of-mass energy given by:

$$E_c = \frac{m_b}{m_a + m_b} E$$

where m_a and m_b are respectively the incident ion and the target atom masses, E is the moving atom kinetic energy.

The scattering of the ion determines the energy transferred to the recoil atom by [100]:

$$T = 4\frac{m_a m_b E}{(m_a+m_b)^2} sin^2\frac{\theta}{2} \quad \text{(I-20)}$$

Different codes based on binary collision approximation have been developed such as MARLOWE, ACAT (Atomic Collisions in Amorphous Targets) and TRIM (Transport of Ions in Matter) using simple MC technique [94, 101].

MARLOWE allows the simulation of atomic collision of linear cascade in a crystalline target and also in a random target [94, 101, 102]. Atomic collision in amorphous target can be treated by ACAT. TRIM simulations treat atomic collision in random targets [101, 102]. In these codes, the possible many-body effects occurring in the cascade were neglected [103]. Then, programs were modified in order to improve the simulation of sputtering collision cascade and subsequently to take into account the effects due to collisions by using dynamical Monte Carlo [94, 102, 104]. Among them, ACOCT is the Atomic Collisions in a Crystalline Target version similar to ACAT code except for collision process in order to study atomic collision in monocrystalline target [102]. DYACAT is the DYnamical simulation of Atomic Collisions in a Crystalline Target using a nonlinear MC code similar to ACAT in a dynamical mode [104]. In this code, the dynamic mode considers many-body collisions between a moving particle and several target atoms. Furthermore, TRIM.SP is the sputtering version of TRIM which treats atomic collision in amorphous target and allows the following of recoil atoms and ions. As a dynamic version of TRIM, TRIDYN code takes into account effects due to collision and target changes [100, 105, 106]. Also, SDTrimSP (where SD stands for Static-Dynamic) has been developed to improve TRIDYN [106–108].

These Monte Carlo codes based on binary collision approximation are known to be fast and allow simulations of sputtering cascade in large space and timescales.

3.2.2. Molecular dynamics

Molecular dynamics is a powerful tool for describing plasma-surface interactions. Thus, it makes it possible to simulate linear and also nonlinear collision cascades of sputtering [109, 110]. In contrary to MC method in binary collision approximation, collisions between incident particles and a system of particles are treated in time evolution using classical

mechanics. The system can be studied at time from femtoseconds to nanoseconds and sometimes to microseconds.

The method of molecular dynamics consist on solving Newton's equations of motion for each particle to simulate the dynamic of the system of particles [111–113]:

$$\overrightarrow{F_i} = m_i \overrightarrow{a_i} = m_i \frac{d\overrightarrow{v_i}}{dt} = m_i \frac{d^2\overrightarrow{r_i}}{dt^2} \quad \text{(I-21)}$$

where $\overrightarrow{F_i}$ is the force applied on atom i exerted by some external agent, m_i is the mass of the atom, $\overrightarrow{a_i}$ is the acceleration, $\overrightarrow{v_i}$ is the velocity and $\overrightarrow{r_i}$ is the position.

In sputtering, ions are released toward the target surface with a velocity corresponding to the energy obtained from the target bias voltage, and impact the target. Then, the particles velocities and accelerations are obtained from forces applied on atoms and give new particles positions. These forces are specified from interatomic potential.

The simulations are therefore primarily based on calculation of interaction force between the particles [114]:

$$F_i = -\nabla_{r_i} V\big(r_1(t), \dots, r_N(t)\big) = m_i \frac{d^2 r_i(t)}{dt^2} \quad \text{(I-22)}$$

where V is the potential energy function governing all interatomic interactions.

Thus, moving atoms and changes of the target during the calculation are considered in molecular dynamics by the accuracy of the interatomic potential [114, 115]. Some interatomic potentials and force fields have been developed from quantum mechanics and chemistry [114, 116]. The force calculation can be performed according to different time steps and can therefore consume more calculation time depending on the applied potential.

Calculations are limited in the size of the model system by the high-energy of incident particles [101]. Indeed, the occurring collision cascade from the impact of high-energy may require too much atoms. Moreover, the calculation time of a MD model depends also on the number of particles in the system and can therefore be very long.

3.2.3. Sputtering yield theory

The erosion of a material by ions bombardment can be measured from the sputtering yield noted in the literature by S or Y. The sputtering yield is defined by the ratio of the number of

sputtered atoms from the target surface per incident ions. Thus, the yield is expressed here by Behrisch and Eckstein as [95]:

$$Y = \frac{average\ number\ of\ atoms\ removed}{incident\ particle} \quad \text{(I-23)}$$

Actually, sputtering measurement can be done according to three categories, as presented by Thompson [22], such as the yield S, the distribution in direction of the sputtered atoms $\frac{dS}{d\Omega}$ and the distribution in energy and direction $\frac{d^2S}{d\Omega dE}$ described by the differentials of sputtering yield. These parameters allow us to obtain information for the deposition velocity and the growing film [11, 117].

The variation of the yield then depends on the ion atomic number, the energy and the angle of incidence [11, 98, 106, 118]. From the theory of collision cascade, Sigmund developed a sputtering yield formula by solving the linearized equation of Boltzmann [21, 98, 119]. The sputtering yield is therefore described by Sigmund as a set of steps including the determination of the energy deposited by the particles near the surface, the conversion of this energy into a number of low-energy recoil atoms, the determination of the number of these recoil atoms come to the surface and finally the selection of atoms with a sufficient energy to overcome the binding forces of the surface [98]. These different steps can be described in the expression of sputtering yield by parameters of cross sections for ions and atoms high-energy also atoms low energy scattering and binding forces of the surface.

- Sigmund formula

The sputtering yield at perpendicular incidence is thus given by Sigmund [98]:

$$S(E) = 0.0420\alpha S_n(E)/U_0 \text{ Å}^2 \quad \text{(I-24)}$$

where the factor α is a function of mass ratio in the elastic collision region, U_0 is the height of the surface potential, $S_n(E)$ is the elastic stopping power.

$S_n(E)$ is expressed from Lindhard and calculated by assuming Thomas-Fermi interaction:

$$S_n(E) = 4\pi Z_1 Z_2 e^2 a_{12}[\, M_1/(M_1 + M_2)]s_n(\epsilon)$$

where ϵ is the reduced energy:

$$\epsilon = \frac{M_2 E/(M_1+M_2)}{Z_1 Z_2 e^2/a_{12}},$$

Z_1 and Z_2 are atomic number of incident particle and target atom respectively, M_1 and M_2 are atomic masses of incident particle and target atom respectively, a_{12} is the Thomas-Fermi screening radii:

$$a_{12} = 0.8853a_0\left(Z_1^{2/3} + Z_2^{2/3}\right)^{-1/2},$$

$s_n(\epsilon)$ is the universal function of reduced nuclear stopping cross section and a_0 is the Bohr radius.

Sputtering yield formulas of energy dependence at perpendicular incidence have been expressed based on the original formula from Sigmund.

- Bohdansky formula

Bohdansky proposed a formula of total sputtering yield at normal incidence for light ion and heavy ion above and for the threshold regime with MARLOWE and TRIM calculations [120]:

$$Y(E) = \frac{0.042}{U_0}\left(R_p/R\right)\alpha S_n(E)\left[1 - (E_{th}/E)^{2/3}\right] \times [1 - (E_{th}/E)]^2 \quad \text{(I-25)}$$

where E is an energy of primary particle, U_0 is the surface binding energy, R is the average path length, R_p is the projected range, α is the energy-independent function of the mass ratio between the target atom and the incident particle, S_n is the nuclear stopping cross section and E_{th} is the threshold energy [121].

The determination of the threshold energy must follow the condition $E_{th} + E_{sp} > E_{sb}/\gamma$ with $E_{sp}$the binding energy of the incident particle to the target surface, $E_{sb}$the surface binding energy and $\gamma = 4M_1M_2/(M_1{+}M_2)^2$ the binary collision energy transfer factor [92].

- Yamamura formula

A simple empirical formula was derived by Matsunami and co-workers [122]:

$$Y(E) = 0.042\frac{\alpha(M_2/M_1)}{U_s}S_n(E)\left[1 - (E_{th}/E)^{1/2}\right] \quad \text{(I-26)}$$

where E is the incident particle energy, E_{th} is the threshold energy, α is the function of the mass ratio between the target atom and the incident particle, U_s is the surface binding energy and $S_n(E)$ is the nuclear stopping cross section..

From this formula, Yamamura developed an expression which describes the angular distribution of sputtered atoms by taking into account an anisotropic velocity distribution given by [122]:

$$S(E,\theta,E_0,\theta_0) =$$
$$0.042\,\frac{\alpha(M_2/M_1,\theta)S_n(E)}{U_s}\times\left[1-\frac{1}{2}(E_{th}/E)^{1/2}\times\left\{cos\theta\gamma(\theta_1)+\frac{3}{4}\pi sin\theta sin\theta_1 cos\phi\right\}\right] \qquad \text{(I-27)}$$

where

$$\gamma(\theta_1)=\frac{3sin^2\theta_1-1}{sin^2\theta_1}+\frac{cos^2\theta_1(3sin^2\theta_1+1)}{2sin^3\theta_1}\times ln\left(\frac{1+sin\theta_1}{1-sin\theta_1}\right),$$

θ and θ_1 are angles of incidence, and ϕ is a scattering angle. The threshold energy E_{th} is determined by:

$$E_{th}=4U_s/\gamma.$$

The **Figure 3** below represents the angular distributions calculated by Yamamura for Ni sputtered atoms by Hg ions impact at normal incidence for different energies. The results were compared to experimental results from Wehner [122].

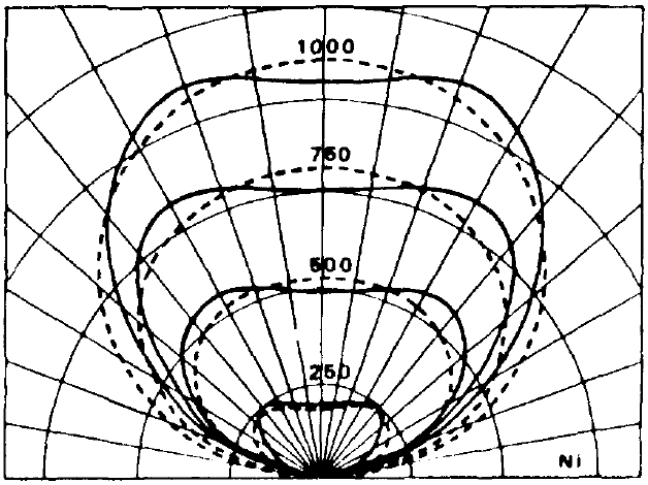

Figure 3: Angular distributions of sputtered atoms from Ni by normally incident Hg+ ions, ———— Wehner's experimental results; — — — calculated results from Eq. I-27 [122].

Then, a new empirical formula was developed by Yamamura using ACAT given by [123], [124]:

$$Y(E) = 0.042 \frac{Q(Z_2)\alpha^*(M_2/M_1)}{U_s} \frac{S_n(E)}{1+\Gamma k_e \epsilon^{0.3}} \times \left[1 - \sqrt{\frac{E_{th}}{E}}\right]^s \quad \text{(I-28)}$$

where Q is a fit parameter which includes the effect of the electronic stopping, Z_2 is the atomic number of target atom, α^* is the function of the mass ratio M_2/M_1:

$$\alpha^* = 0.249(M_2/M_1)^{0.56} + 0.0035(M_2/M_1)^{1.5} \qquad M_1 \leqslant M_2 ,$$
$$= 0.0875(M_2/M_1)^{-015} + 0.165(M_2/M_1) \qquad M_1 \geqslant M_2$$

k_e is the Lindhard electronic stopping coefficient, ϵ is the reduced energy:

$$\epsilon = E \frac{M_1}{M_1+M_2} \frac{a_L}{Z_1 Z_2 e^2} ,$$

Γ is a factor:

$$\Gamma = \frac{W(Z_2)}{1+(M_1/7)^3} ,$$

$Q(Z_2)$ and $W(Z_2)$ are parameters defined by using the Ziegler-Biersack-Littmark (ZBL) repulsive potential in Yamamura and Tawara [124] and s is the power equal to 2.8 by using the power approximation of $m = 1$ which corresponds to Rutherford scattering.

- Eckstein formula

Also, Eckstein and Preuss proposed a fit formula of sputtering yield at normal incidence with TRIM.SP given by [92, 125]:

$$Y(E_0) = q s_n^{KrC}(\varepsilon_L) \frac{\left(\frac{E_0}{E_{th}}-1\right)^\mu}{\lambda/w(\varepsilon_L)+\left(\frac{E_0}{E_{th}}-1\right)^\mu} \quad \text{(I-29)}$$

where $s_n^{KrC}(\varepsilon_L)$ is the nuclear stopping power for KrC Wilson-Haggmark-Biersack (WHB) potential given by:

$$s_n^{KrC}(\varepsilon_L) = \frac{0.5 ln(1+1.2288\varepsilon_L)}{w(\varepsilon_L)} ,$$

$$w(\varepsilon_L) = \varepsilon_L + 0.1728\sqrt{\varepsilon_L} + 0.008{\varepsilon_L}^{0.1504} ,$$

ε_L is the reduced energy given by:

$$\varepsilon_L = E_0 \frac{M_2}{M_1+M_2} \frac{a_L}{Z_1 Z_2 e^2} = E_0/\varepsilon \,,$$

a_L is the Lindhard screening length given by:

$$a_L = \left(\frac{9\pi^2}{128}\right)^{1/3} a_B \left(Z_1^{2/3} + Z_2^{2/3}\right)^{-1/2} ,$$

a_B is the Bohr radius, Z_1 Z_2 and $M_1 M_2$ are the atomic numbers and atomic masses of incident particle and target atom, E_{th} is the threshold energy which is a fitting parameter as well as q for the absolute yield, λ for the decrease of the yield at low energies towards the threshold and μ for the strength of this decrease [92].

4. Outline

Since Grove's discovery, several sputtering techniques have been introduced in order to improve the production of thin films and coatings. Researchers have been focussed on main goals such as sputtering of various targets of conductive or insulating material, producing compound and hard coatings, deposition of high quality and dense films and coatings, increasing of sputtering and deposition rates, enlarging area samples treatment, and finally applying the process in industrial scale. Among them, magnetron sputtering process is used in GREMI for studies of growing films thanks to the simplicity of the system and the advantages it offers in term of control of composition and microstructure and sputtering and deposition rates. Moreover, it is today the process of choice by industries to deposit thin films for a wide range of applications.

The desire to synthesize more and more complex materials of high quality leads researchers to understand the mechanism involved in the atomic-scale process for studying growing films as well as the plasma-surface interactions that cannot be directly studied by experiments. With development of computers and numerical simulations, magnetron sputtering models have been developed in order to study the different mechanisms involved and optimize the process.

Thus, the motivation of this work is to contribute to the build of a multi-scale model coupling fluid and molecular dynamic approaches to represent a real magnetron sputtering system. Indeed, it consists on the simulation of a DC planar magnetron discharge in first part whose

results will then be coupled for sputtering and deposition process in following parts in order to obtain an important numerical tool of magnetron sputtering process.

A previous work based on the simulation of sputtering deposition and thin film growth was achieved by Xie [126]. In this thesis we are interested on the magnetron discharge itself and sputtering erosion modelling.

In the **Chapter 2** we study the simulation of a DC planar magnetron discharge in a cylindrical geometry using a CFD model performed with COMSOL Multiphyics® software.

Then, in the **Chapter 3** the sputtering erosion of a pure titanium (Ti) target in neutral gas of Ar and in reactive gas of Ar-O_2 is modelled by MD. Long time scale modelling of sputtering using the force-bias Monte Carlo (fbMC) method is also implemented to account for possible long relaxation times. For both methods, we are interested in calculating the sputtering yields and argon retention rates.

Finally, this manuscript will be ended with a conclusion and some perspectives.

II. The magnetron sputtering discharge

1. Introduction

Numerical simulations are very used today to characterize and to predict discharge phenomena involved in a process in order to optimize it. Therefore, it allows the determination of parameters such as, for a magnetron sputtering discharge, the electric potential, the plasma density in non-reactive or in reactive gas, the charged particles densities, temperatures and energy distributions with the presence of a magnetic field.

Different models have been developed using particle, fluid or hybrid approaches to simulate a magnetron discharge. Among them, the PIC/MCC method is the most common despite computation time drawbacks.

Fluid model is interesting to use due to the acceptable computation time it requires. Nevertheless, it is much discussed in the case of low-pressure magnetron sputtering discharge modelling. Indeed, fluid conditions must be verified with low-pressures. Moreover, the effect of an inhomogeneous magnetic field to charged particles could not be easy to describe when they are considered as fluid. However, some models of magnetron discharge based on CFD have been developed as in the Ph. D. works of Costin [83].

In this chapter, we are interested on the modelling of a DC planar magnetron discharge, based on the theoretical model from Costin, solved by COMSOL Multiphysics® software. The main objective of this part is to obtain plasma parameters information with acceptable computation time for our multi-scale model and finally to apply the model to a configuration that we control for experiments.

2. The theoretical model

The model from Costin presents a DC non-reactive and reactive magnetron discharges with argon and a mixture of argon-oxygen developed by a "home-made" code using a fluid approach. The validity of this fluid model is justified firstly by the choice to study the discharge in a region close to the target which allows a macroscopic representation of electrons Boltzmann's equation. Indeed, due to the large electron density, the Boltzmann's equation can describe the electron kinetics. Then, the presence of the magnetic field must reduce the effective distance of electrons between two collisions as for an increase of the pressure [71]. Moreover, it has been chosen to work with a solved model, such as Costin's one, because it is a first work on this subject for us and this allows comparison with our results deduced from a different solver. Actually, among the few presented fluid models of magnetron discharge, it is one of the few to offer a detailed description of the model and good quantity of results [71, 83].

2.1. Basic equations

Theoretical fluid model is based on the resolution of moments of Boltzmann's equation coupled with Poisson's equation in order to describe the transport of charged particles.
In this model, two types of particles, the electrons and the ions, are treated in a region close to the target by solving the three moments of Boltzmann's equation such as the continuity, the momentum transfer and the mean energy transfer. This last one is only calculated for electrons.

- Continuity

$$\frac{\partial n_s}{\partial t} + \nabla . \overrightarrow{\Gamma_s} = S_s \qquad \text{(II-1)}$$

with s: type of particle ($s = e$ for electron and i for ion), n_s: particle density, t: time, $\overrightarrow{\Gamma_s} = n_s \overrightarrow{v_s}$: flux of particles, $\overrightarrow{v_s}$: velocity, and S_s: source term of continuity equation

- Momentum transfer

$$m_s n_s \left[\frac{\partial \overrightarrow{v_s}}{\partial t} + (\overrightarrow{v_s}.\nabla)\overrightarrow{v_s}\right] = q_s n_s\left(\vec{E} + \overrightarrow{v_s} \times \vec{B}\right) - \nabla\overrightarrow{\overrightarrow{P_0}} - m_s n_s f_{ms} \overrightarrow{v_s}\left(1 + \frac{S_s}{n_s f_{ms}}\right) \qquad \text{(II-2)}$$

with m_s: mass, q_s: charge of the particle, $\vec{E}$: electric field, $\vec{B}$: magnetic field, $\overrightarrow{\overrightarrow{P_0}}$: pressure tensor and f_{ms}: total momentum transfer frequency for specie s-neutral collisions.

- Mean energy transfer

$$\frac{\partial(n_s\varepsilon_s)}{\partial t} + \nabla.\overrightarrow{\Gamma_{\varepsilon s}} = -\overrightarrow{\Gamma_s}.\vec{E} - \theta_s n_s \quad \text{(II-3)}$$

with ε_s: mean energy, $\overrightarrow{\Gamma_{\varepsilon s}} = n_s\langle\varepsilon_s\overrightarrow{v_s}\rangle$: energy flux and θ_s: energy loss rate for s-neutral collisions.

- Poisson's equation

$$\Delta V = -\frac{e}{\varepsilon_0}(n_i - n_e) \quad \text{(II-4)}$$

with V: electric potential and constants of elementary charge e and permittivity of free space ε_0.

These equations allow the calculation of charged particles transport and the determination of parameters such as the electric potential, the charged particles densities and the mean energy distributions. However, they use transport coefficient or properties which depend on variables. Finally, the system of equations is highly non-linear and highly coupled as shown in **Figure 4**, at the end of this part, which represents how different parameters are related. This characteristic makes the resolution of the system much more difficult.

2.2. Hypotheses and approximations

The theoretical model from Costin is based on assumptions and approximations which simplify the system of equations to solve. In fact, the simple cylindrical configuration on which it is applied gives the possibility to define an axial symmetry which thus allows writing equations in cylindrical coordinates $(r,\ \varphi,\ z)$ and supposing null the azimuthal components of electric and magnetic fields. By neglecting instabilities of azimuthal drift current, the component of particles fluxes $\Gamma_{s\varphi}$ generated by the presence of $E \times B$ drift is expressed according to Γ_{sr} and Γ_{sz}. The model is therefore reduced in two dimensions $(r,\ z)$.

With regard to electrons transport, the term of inertia $m_e n_e \left[\frac{\partial \overrightarrow{v_e}}{\partial t} + (\overrightarrow{v_e} \cdot \nabla)\overrightarrow{v_e}\right]$ is negligible due to the low mass of electrons and the ionization frequency f_{iz} is negligible by the total quantity of electron-neutral momentum transfer frequency f_{me}. Moreover, by supposing an isotropy of electrons distribution function, the pressure tensor is considered as scalar $P_e = n_e k T_e$ with k Boltzmann constant and T_e electrons temperature.

The electrons momentum transfer equation can be written as:

$$n_e \overrightarrow{v_e} = -\mu_e n_e \vec{E} - \nabla(D_e n_e) - n_e \overrightarrow{v_e} \times \frac{\overrightarrow{\Omega_e}}{f_{me}} \tag{II-5}$$

where q_e is replaced by $-e$, $\overrightarrow{\Omega_e} = \frac{e\vec{B}}{m_e}$ is the electrons cyclotron frequency, $\mu_e = \frac{e}{m_e f_{me}}$ is the electrons mobility and $D_e = \frac{kT_e}{m_e f_{me}}$ is the electrons diffusion coefficient.

The reduced electrons flux coefficients can be written from the approximation of the EEDF $f(\vec{r}, u)$ by [127]:

$$\mu_e(\vec{r})N = -\frac{1}{3}\sqrt{\frac{2e}{m_e}}\int_0^\infty \frac{u}{\sigma_{me}(u)}\frac{\partial f_0(\vec{r},u)}{\partial u}du \tag{II-6}$$

$$D_e(\vec{r})N = \frac{1}{3}\sqrt{\frac{2e}{m_e}}\int_0^\infty \frac{u}{\sigma_{me}(u)} f_0(\vec{r},u)\,du \tag{II-7}$$

where $u = \frac{m_e v^2}{2}$ is the electron kinetic energy, σ_{me} is the total momentum-transfer cross-section for electron-neutral collisions, $N = \frac{p}{kT}$ is the gas density and $f_0(\vec{r}, u)$ is the isotropic part of $f(\vec{r}, u)$ which satisfies the normalization condition $\int_0^\infty f_0(\vec{r},u)\,u^{1/2}du = 1$.

The study of the discharge in a region close to the target allows the application of the magnetic field only in electrons transport. Thus, the electron flux can be expressed by:

$$\overrightarrow{\Gamma_e} = \overrightarrow{\Gamma_e^0} + \overrightarrow{\Gamma_e^1} \tag{II-8}$$

where $\overrightarrow{\Gamma_e^0} = -\mu_e n_e \vec{E} - \nabla(D_e n_e)$ is the classical drift-diffusion flux of electrons and where $\overrightarrow{\Gamma_e^1} = -n_e \overrightarrow{v_e} \times \frac{\overrightarrow{\Omega_e}}{f_{me}} = -\overrightarrow{\Gamma_e} \times \frac{\overrightarrow{\Omega_e}}{f_{me}}$ is the flux which contains the magnetic field.

In the same way, the electrons energy flux can be expressed by:

$$\overrightarrow{\Gamma_{\varepsilon e}} = \overrightarrow{\Gamma_{\varepsilon e}^0} + \overrightarrow{\Gamma_{\varepsilon e}^1} \tag{II-9}$$

with $\overrightarrow{\Gamma_{\varepsilon e}^{0}} = -\mu_{\varepsilon e} n_e \varepsilon_e \vec{E} - \nabla(D_{\varepsilon e} n_e \varepsilon_e)$ and $\overrightarrow{\Gamma_{\varepsilon e}^{1}} = -n_e \langle \varepsilon_e \overrightarrow{v_e} \rangle \times \frac{\overrightarrow{\Omega_e}}{f_{me}} = -\overrightarrow{\Gamma_{\varepsilon e}} \times \frac{\overrightarrow{\Omega_e}}{f_{me}}$.

The reduced coefficients of electrons energy flux are written from the approximation of the EEDF by:

$$\mu_{\varepsilon e}(\vec{r})N = -\frac{1}{\varepsilon_e(\vec{r})}\frac{1}{3}\sqrt{\frac{2e}{m_e}}\int_0^{\infty}\frac{u}{\sigma_{me}(u)}\frac{\partial f_0(\vec{r},u)}{\partial u}du \qquad \text{(II-10)}$$

$$D_{\varepsilon e}(\vec{r})N = \frac{1}{\varepsilon_e(\vec{r})}\frac{1}{3}\sqrt{\frac{2e}{m_e}}\int_0^{\infty}\frac{u}{\sigma_{me}(u)} f_0(\vec{r},u)\,du \qquad \text{(II-11)}$$

The spatial variation of these parameters can be obtained according to the approximation of the local mean energy by introducing the spatial dependence of the EEDF with the electrons mean energy profile $\varepsilon_e(\vec{r})$.

The high density of the plasma allows the use of a Maxwellian distribution instead of the calculation of Boltzmann equation solution for electrons:

$$f_0(\vec{r},u) = f_0[\varepsilon_e(\vec{r}),u] \equiv \frac{2}{\sqrt{\pi}}\left[\frac{2\varepsilon_e(\vec{r})}{3}\right]^{-\frac{3}{2}} exp^{-\frac{3u}{2\varepsilon_e(\vec{r})}} \qquad \text{(II-12)}$$

The electrons energy loss rate is also determined according to the approximation of the EEDF [127]:

$$\theta_e(\vec{r}) = N\frac{2m_e}{M_n}\sqrt{\frac{2e}{m_e}}\int_0^{\infty}\sigma_{en}^{el}(u) f_0(\vec{r},u)\,u^2 du + \sum_k^{inel} W_k f_{ke}(\vec{r}) \qquad \text{(II-13)}$$

where M_n is the mass of neutral atoms, σ_{en}^{el} is the elastic cross-section of electron-neutral collisions, W_k is the energetic threshold for the inelastic process k which is characterized by the collision frequency f_{ke}:

$$f_{ke}(\vec{r}) = N\sqrt{\frac{2e}{m_e}}\int_0^{\infty}\sigma_{ke}(u) f_0(\vec{r},u) u du \qquad \text{(II-14)}$$

Actually, for ions transport, the radius of cyclotron gyration is higher than the linear dimension of the studied region. Therefore, the magnetic field has a negligible influence on the ions. The separation of movements of drift, for ions velocity, and thermal, for diffusion, allows the use of a scalar ionic pressure $P_i = n_i k T_i$ with T_i ions temperature.

The ions momentum transfer equation is thus written as:

$$n_i\vec{v_i} = \mu_i n_i \vec{E} - \nabla(D_i n_i) - \frac{n_e}{n_i}\frac{f_{iz}}{f_{mi}} n_i \vec{v_i} - \frac{1}{f_{mi}} n_i \left[\frac{\partial \vec{v_i}}{\partial t} + (\vec{v_i} \cdot \nabla)\vec{v_i}\right] \quad \text{(II-15)}$$

where $\mu_i = \frac{e}{m_i f_{mi}}$ is ions mobility and $D_i = \frac{kT_i}{m_i f_{mi}}$ ions diffusion coefficient.

The flux of ions can be simplified into drift-diffusion expression with the introduction of an effective field by identification. Ions are then in equilibrium with this effective field given by:

$$\frac{\partial \vec{E}^{eff}}{\partial t} = f_{mi}\left(\vec{E} - \vec{E}^{eff}\right) - f_{iz}\frac{n_e}{n_i}\frac{\vec{v_i}}{\mu_i} - \frac{1}{\mu_i}(\vec{v_i} \cdot \nabla)\vec{v_i} \quad \text{(II-16)}$$

Finally, the source term is determined by considering electrons and ions created only by ionization due to electron-neutral collisions $S_e = S_i = f_{iz} n_e$ with f_{iz}: ionization frequency by electron-neutral impact.

2.3.Boundary conditions

In order to solve the different equations, boundary conditions are imposed for charged particles fluxes and electric potential. These ones are applied on the reactor walls as well as on the axis of the discharge. The detailed geometry of the reactor is given in paragraph **3.1.2** entitled “Computational domain”. The general boundary conditions that can be applied whatever the reactor geometry is however given here.

For the resolution of Poisson’s equation, a negative voltage is applied to the cathode and the anode is grounded. The radial electric field is null due to the symmetry on the discharge axis.

With regard to charged particles transport, the conductive metallic walls of the reactor entirely absorb the charges. Consequently, all parallel fluxes $\Gamma_s^{\parallel}$ to the walls are null.

In the absence of a magnetic field, on the anode, the electrons flux is expressed by:

$$\Gamma_e^{\perp} = \frac{1}{2} n_e \langle v_e \rangle \quad \text{(II-17)}$$

where $\langle v_e \rangle$ is electrons mean velocity on the wall.

By integrating the velocity on the EEDF, $\langle v_e \rangle$ is written as $\langle v_e \rangle = \sqrt{\frac{2e}{m_e}} \int_0^{\infty} f_0(\vec{r}, u) u du$

This condition includes drift-diffusion effects of electrons movement.

The electrons energy flux is:

$$\Gamma_e^{\perp} = \frac{1}{2} n_e \langle \varepsilon_e v_e \rangle \quad \text{(II-18)}$$

On the cathode, the electrons flux is composed by two components. One contains electrons from the discharge $\frac{1}{2}n_e\langle v_e\rangle$. This one is negligible due to the low electron density in the cathode fall with respect to the other one which is specified by secondary electrons from ions impact $-\gamma_i\Gamma_i^{\perp}$ with γ_i the coefficient for secondary electron emission.
Finally, with the presence of a magnetic field, the electrons flux is written on the cathode by:

$$\Gamma_e^{\perp} = -\gamma_i\Gamma_i^{\perp}\left(1 - \frac{{\Omega_{er}}^2}{{f_{me}}^2+{\Omega_e}^2}\right) \quad \text{(II-19)}$$

The electrons energy flux on the cathode is the product of the secondary electrons flux and the mean output energy ε_0:

$$\Gamma_{\varepsilon e}^{\perp} = \Gamma_e^{\perp}\varepsilon_0 = -\gamma_i\Gamma_i^{\perp}\left(1 - \frac{{\Omega_{er}}^2}{{f_{me}}^2+{\Omega_e}^2}\right)\varepsilon_0 \quad \text{(II-20)}$$

The ions flux on walls is the sum of thermal flux for an isotropic ionic distribution function and drift flux with effects of effective field:

$$\Gamma_i^{\perp} = \frac{1}{4}n_i v_{thi} + \delta q_i\mu_i n_i E^{eff\perp} \quad \text{(II-21)}$$

where $v_{thi} = \sqrt{\frac{8kT_i}{\pi m_i}}$ is the ions thermal velocity, $\delta = 1$ when ions are accelerated towards the surface by $E^{eff\perp}$ otherwise $\delta = 0$.
Furthermore, the densities of charged particles are constant on the discharge axis.

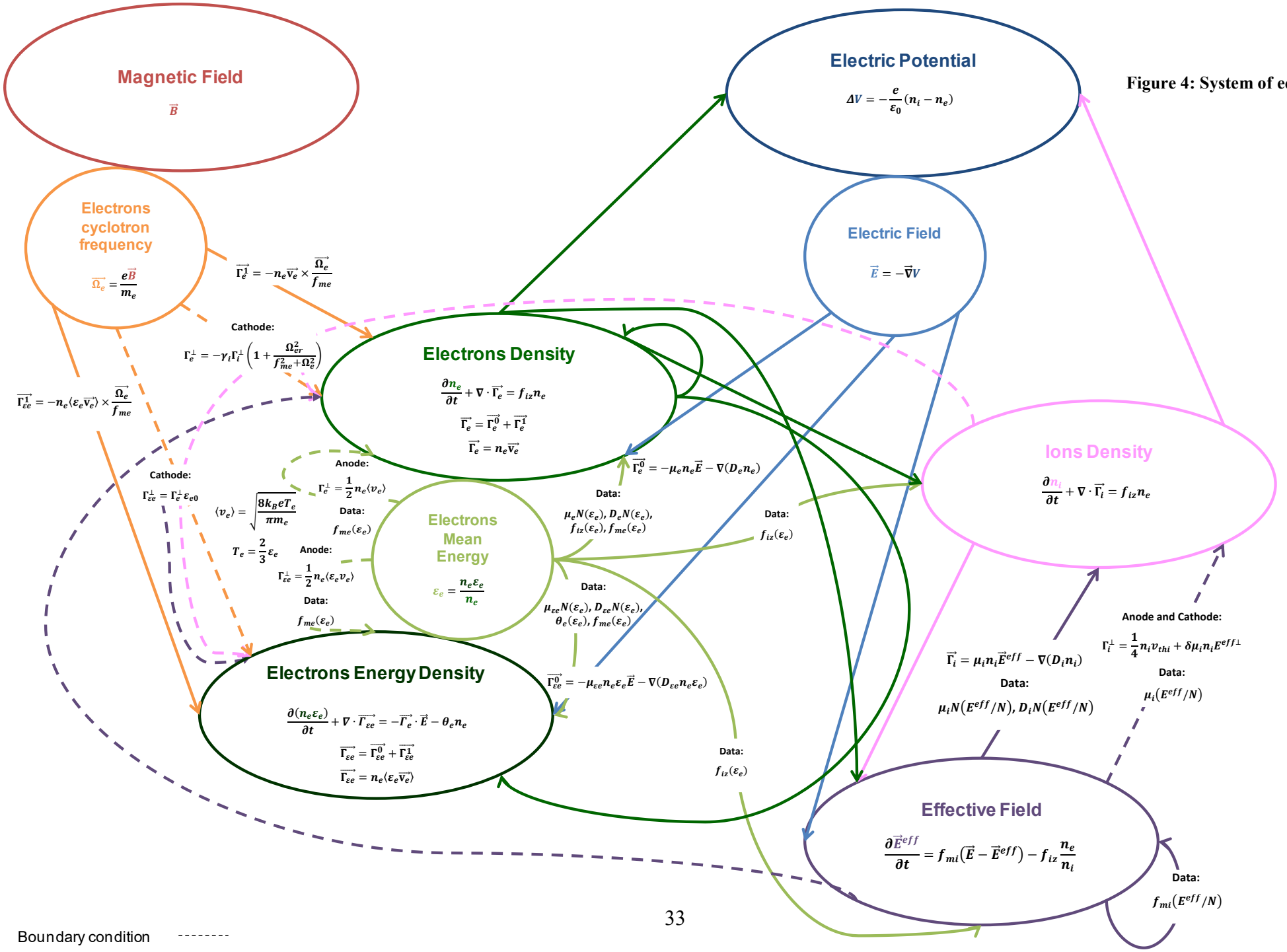

Figure 4: System of equations.

3. Implementation in COMSOL Multiphysics®

COMSOL Multiphysics® software is a performing tool of multiphysics modelling in 1D, 2D and 3D for engineering applications, scientist development and research [75]. This numerical tool consists of solving Partial Differential Equations (PDEs) by the Finite Element Method (FEM). It is composed by diverse modules of application including mathematics and physics modules for specific applications modelling.

These modules are applied to a geometry which is directly designed with the tool or which can also be imported into the software.

The mathematics module gives the possibility to implement freely PDE by choosing a representation among 'Weak Form', 'General Form' and 'Coefficient Form' expressions. In contrary, PDEs in physics modules are already predefined according to diverse domains of application such as for example in diffusion, in electromagnetic and in plasma physics. Modules can then be coupled to build a multiphysics approach to represent a real system [128].

In our case, in order to implement in details the theoretical model of Costin, we will use the mathematics module to simulate the magnetron discharge. Furthermore, the magnetic field is emitted by permanent magnets and thus is considered constant. This therefore allows two studies. Indeed, the first study is stationary with the calculation of the magnetic field distribution and the second is time-dependent with the treatment of charged particles.

Our interest of using this commercial tool is mainly due to advantages of accessibility and portability in addition to the powerful solver tool that is COMSOL. However, simulations may require some adjustments difficult to add in the resolution system. Actually, it is not possible to have a real control of the solver due to standardization of software which makes COMSOL as a 'black box'.

3.1. Configuration

The model, on which we based ourselves to start, describes a DC planar magnetron discharge in argon gas, in a cylindrical reactor. The description of the discharge is translated into different expressions of PDEs mentioned previously which cannot be solved by analytical method. However the solution of these equations can be approximated numerically. The finite element method, used in COMSOL, is one of the numerical methods of discretization for

PDEs approximation like the Finite Difference Method (FDM) used in Costin's works. Application of discretization techniques requires the definition of a mesh in order to subdivide the studied region. The FEM has the particularity of using linear piecewise mesh which form triangular elements.

3.1.1. Finite Element Method

The finite element method (FEM) consists on subdivide the studied region by finite elements to replace the governing PDE of the problem on each elements by a system of linear equations. A global system regroups all the linear equations system of the finite elements in order to obtain an approximation of the PDE solution according to the boundary conditions.

Actually, FEM was first suggested by Courant in 1943 with the idea to define trial linear functions on triangular elements formed by the diagonals of squares of the mesh of the subdivided region and was later developed in 1960's to become a very effective numerical technique [129–131].

This method is interesting to use for applications in complex geometry because it does not require a uniform distribution of elements as presented in the figure below from COMSOL engineering guide [132].

The function u is approximated with u_h given by $u_h = \sum u_i \psi_i$.

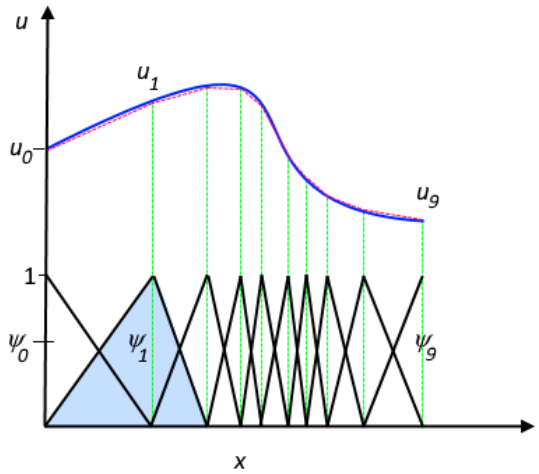

Figure 5: Principle of FEM in 1D problem [132].

The function u (solid blue line) is approximated with uh (dashed red line), which is a linear combination of linear basis functions (ψ_i is represented by the solid black lines). The coefficients are denoted by u0 through u9.

3.1.2. Computational domain

The cylindrical geometry of the system allows the treatment of the discharge from 3D to a 2D-axisymmetric configuration according to (r,z) [83]. The discharge is modelled in a region closed to the target of a radius and a height of 26.95 mm. The target is a metallic disc with a radius of 16.50 mm represented by the cathode. The thickness of the target depends on material which constitutes it. For a non-magnetic material the target thickness is between 1.27 and 5.88 mm otherwise it is between 1.27 and 3.175 mm. The metallic walls of the reactor are grounded and form the anode. An insulating gap of 0.25 mm is located between the anode and the cathode. The magnetic device is composed by a central cylindrical magnet and an outer ring magnet. The central magnet has a diameter of 12.50 mm and a height of 12 mm. The ring has inner and outer diameters of 24 mm and 30 mm respectively and a height of 13 mm.
The polarities of the magnets are opposite in order to obtain a CM closed magnetic field lines.
The following **Figure 6** represents the geometry of the system designed with COMSOL.

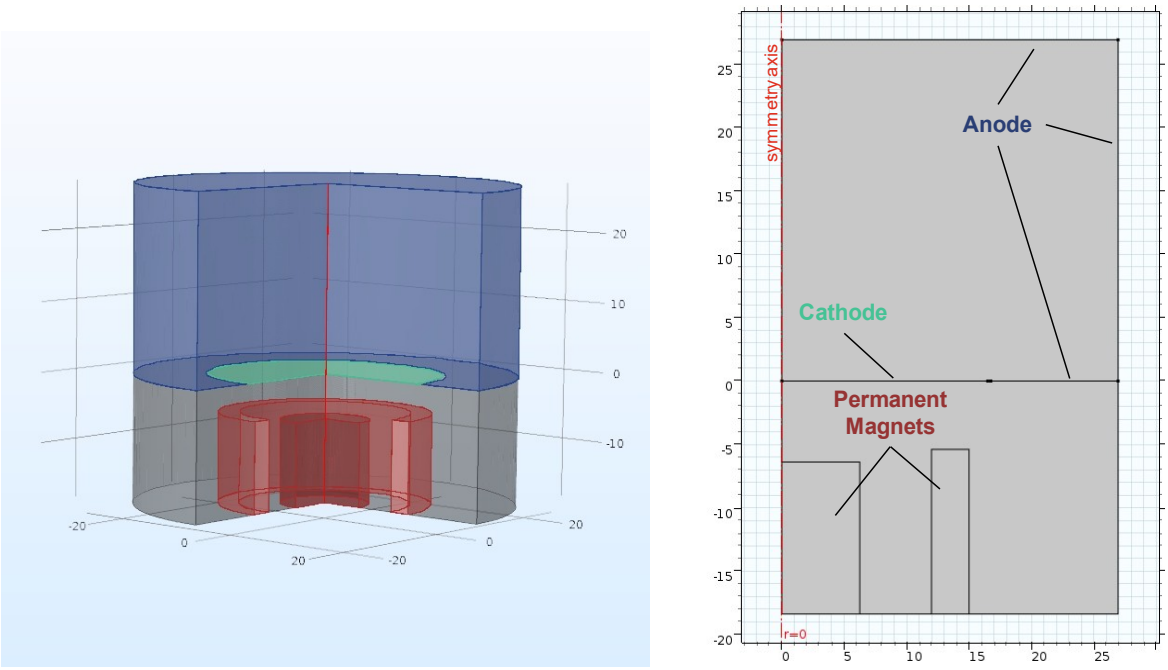

Figure 6: Geometry of the model. The reactor configuration is presented in 3D (left) and in 2D-axisymmetry (right).

3.1.3. Computation limits

Conditions of the spatial mesh distance Δx and the time step Δt must be respected to solve correctly the model equations [83].

Δx must be chosen small enough in order to consider constant the local density of scattering particles for a distance equal to Δx.

Δx also must be higher than Debye length to treat plasma density on mesh nodes.

Δt must verify condition of stability such as $\Delta t < min(t_M, t_{CFL})$ with times of Maxwell t_M and Courant-Friedrichs-Lewy (CFL) t_{CFL}.

Indeed, the velocity of physical magnitudes temporal variation limits the time step. The stability of charge space and electric field is guaranteed for values of Δt lower than time of Maxwell of dielectric relaxation:

$$\Delta t = \frac{\varepsilon_0}{e(n_e\mu_e + n_i\mu_i)} \quad \text{(II-22)}$$

The Courant-Friedrichs-Lewy stability criterion limits the covered distance of a particle in a time step according to spatial mesh dimension Δx:

$$\Delta t \leq \frac{\Delta x}{\langle v \rangle} \quad \text{(II-23)}$$

with $\langle v \rangle$ the mean velocity of particle.

3.1.4. Mesh

The 2D-axisymmetric configuration used in this model allows a spatial discretization of the problem on a uniform mesh according to (r,z). Costin studied two size of mesh composed of quadrilateral elements with number of elements on r and z axis $N_r \times N_z$ of 50×50 which gives a spatial mesh distance $\Delta x = 0.55$ mm and 72×72 with $\Delta x = 0.38$ mm.

In COMSOL, mesh using triangular elements can be predefined according to the desired quality, including coarse and fine distributions. These predefined meshes were applied on the geometry of the model from ‘Extremely Coarse’ type with 52 triangular elements and an average quality of 0.8646 to ‘Extremely Fine’ type with 9577 triangular elements and an average quality of 0.9862 in the domain of the discharge as presented in the following figure.

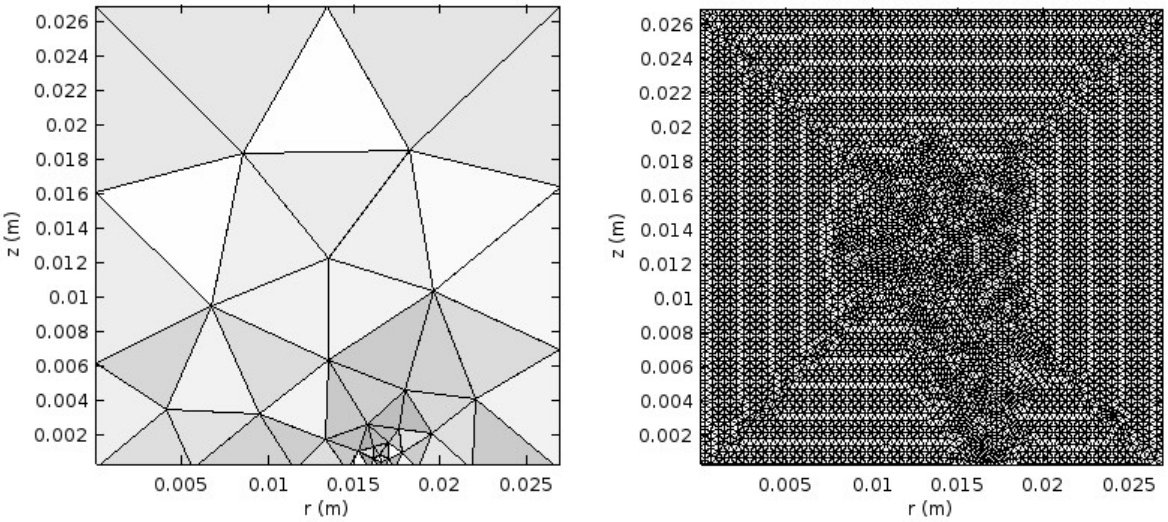

Figure 7: Extremely Coarse (left) and the Extremely Fine (right) meshes.

All the predefined meshes were applied to our model with respect to the resulting Gaussian density for a study on density diffusion coefficient.

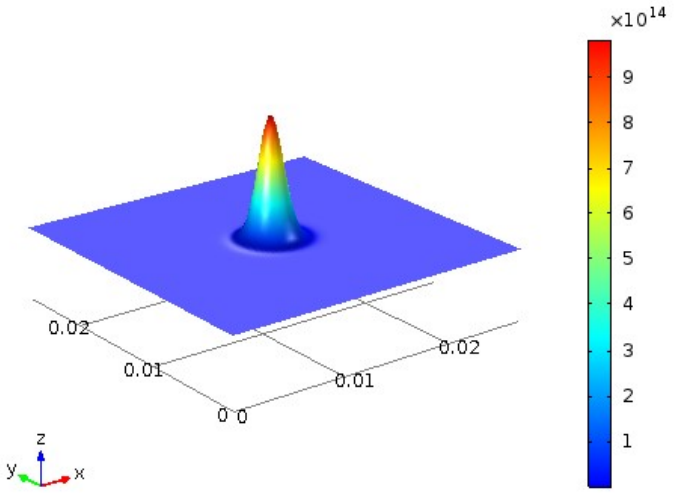

Figure 8: Gaussian density ($1/m^3$).

The following figures represent the profile of this density according to r-axis for five predefined meshes.

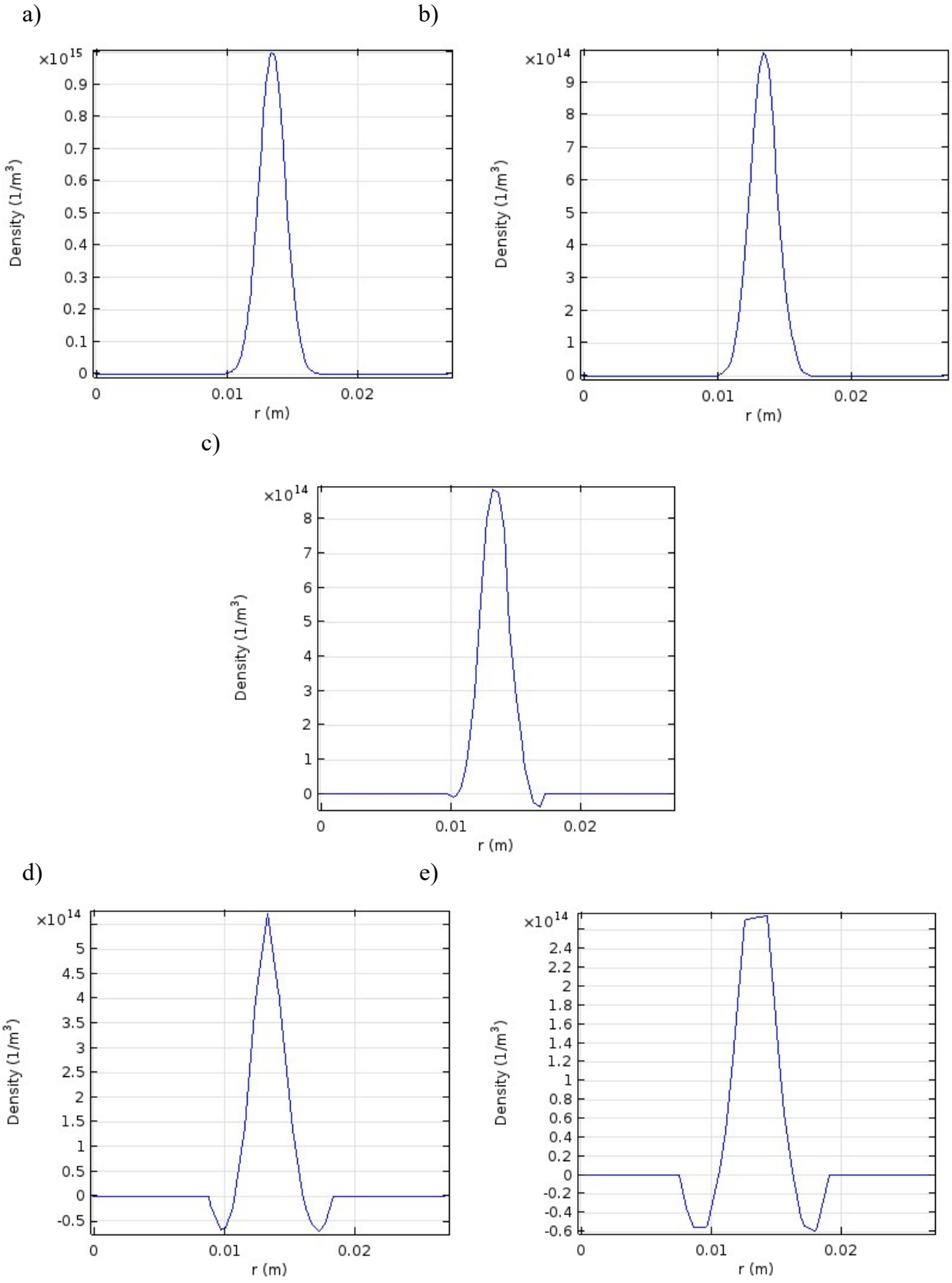

Figure 9: The profile of Gaussian density according to different meshes: a) Extremely Fine mesh, b) Finer mesh, c) Normal mesh, d) Coarser mesh and d) Extremely Coarse mesh.

It is also possible to restructure the predefined mesh with quadrilateral elements by choosing the ‘Mapped’ mesh option proposed by the software. This gives the possibility to design a mesh almost similar to the one used in Costin’s model although the method of discretization remains different from that used by Costin. Thus, the geometry of the model is composed by 2450 quadrilateral elements in the discharge domain with an average quality of 0.9943.

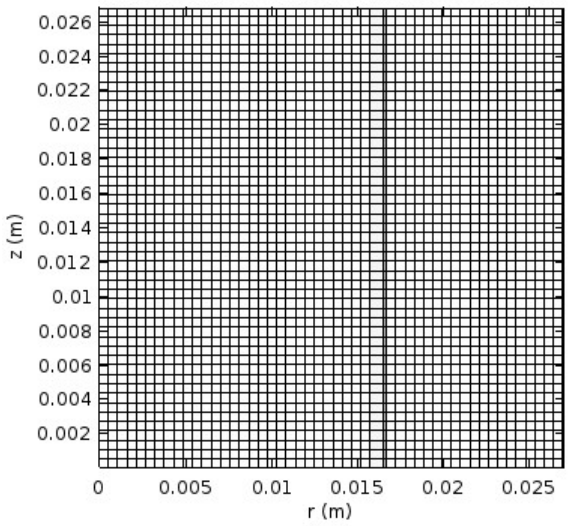

Figure 10: Mapped mesh of 50×50.

Then, by applying this mesh to the Gaussian density, the results obtained is equivalent to Extremely Fine mesh.

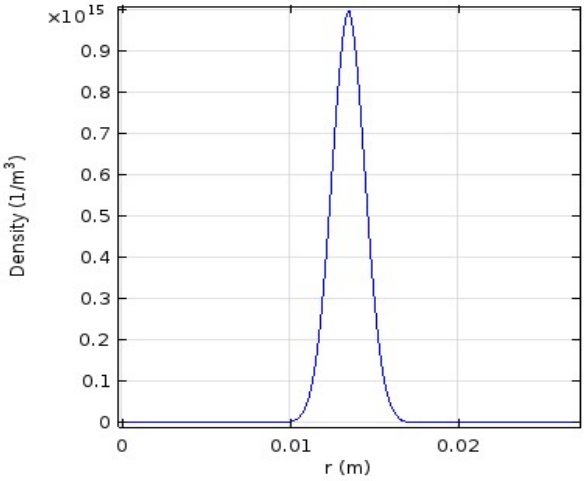

Figure 11: Finer mesh.

In order to have a good compromise between quality of plotted results and computation time, we chose to compute our model according to the 'Finer' predefined mesh. Indeed, the density plotted with this mesh is close to the one obtained with the most precise mesh. The geometry is then composed by 747 elements in the domain of the discharge with an average quality of 0.9771.

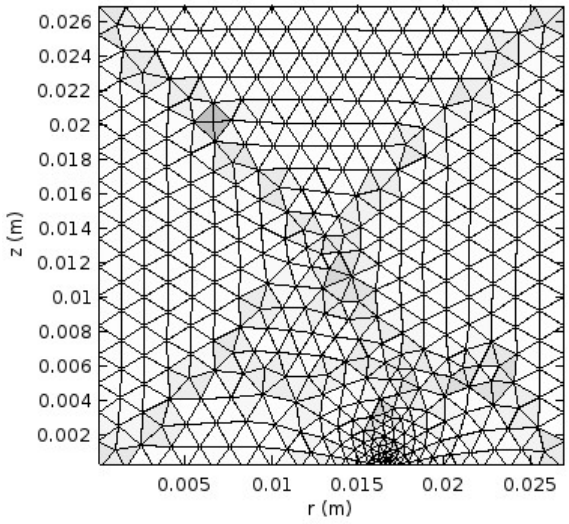

Figure 12: Finer mesh.

3.2.Magnetic field

For the first part of the magnetron discharge modelling, we are interested in the representation of the magnetic field distribution. As permanent magnets are used in the model, the magnetic field is therefore constant and it allows us to study it in a stationary case.

The magnetic field of permanent magnets can be calculated in COMSOL with the 'Magnetic Fields, No Currents' interface in the 'ACDC' module. This physics interface consists on computation of magnetic field density B by solving Gauss' law $\nabla \cdot B = 0$ and based on magnetic flux conservation.

In the absence of electric currents, the Maxwell-Ampère's law is $\nabla \times H = 0$. Therefore, the magnetic field H can be defined as scalar magnetic potential V_m from the relation $H = -\nabla V_m$. Considering the constitutive relation $B = \mu_0(H + M)$, the Gauss's law can be written as:

$$-\nabla \cdot (\mu_0 \nabla V_m - \mu_0 M) = 0 \qquad \text{(II-24)}$$

with μ_0: the permeability of vacuum and M: the magnetization of the magnet.

In 2D planar, the distance d in the z direction is involved in the formulation giving:

$$-\nabla \cdot d(\mu_0 \nabla V_m - \mu_0 M) = 0 \qquad \text{(II-25)}$$

In the model, the magnetizations of the central and the outer magnets are defined by M_0 and $-M_0$ respectively. However, in the absence of information, the values of M_0 and d are determined in order to obtain the same magnetic field distribution than the one used in the model of Costin [83].

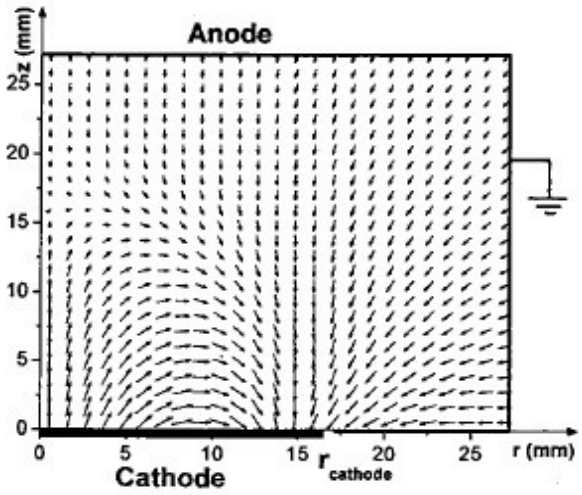

Figure 13: Magnetic field map used in Costin's model [83].

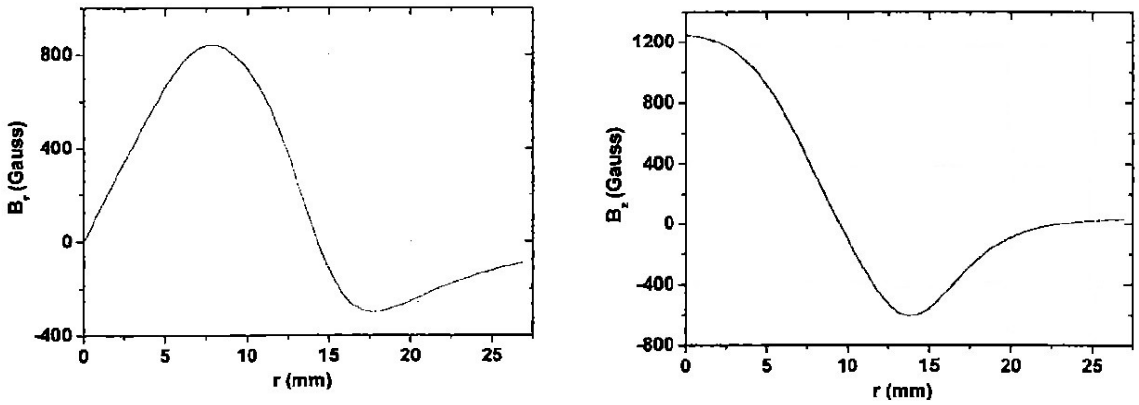

Figure 14: Radial variation of magnetic field radial component B_r (left) axial component B_z (right) [83].

The magnetic field thus depends on the couple $(M_0\,, d)$.

We therefore specify the magnetization M_0 referred to our own magnets and the distance d as the thickness of the target according to the values given in the subpart **3.1.2**.

The obtained results will then be used as parameters for the resolution of electrons transport and electrons energy equations in the second part of the work.

3.3.Magnetron discharge

The magnetron discharge is characterized by the treatment of two charged particles as the electrons and the ions. The charged particles transport is described in this model by the three first moments of Boltzmann's equation coupled with Poisson's equation. All of these equations are implemented in this work in COMSOL using the 'Coefficient Form PDE' interface of the 'Mathematics' module.

Our interest to use this interface is due to the possibility to specify each coefficient of the PDE such as the mass coefficient e_a, the damping or mass coefficient d_a, the diffusion coefficient c, the conservative flux convection coefficient α, the conservative flux source γ, the convection coefficient β, the absorption coefficient a and the source term f [75].

For a variable u, the PDE is thus expressed by:

$$e_a \frac{\partial^2 u}{\partial t^2} + d_a \frac{\partial u}{\partial t} + \nabla \cdot (-c\nabla u - \alpha u + \gamma) + \beta \cdot \nabla u + au = f \qquad \text{(II-26)}$$

Conservative flux

with $\nabla = \left[\frac{\partial}{\partial r}, \frac{\partial}{\partial z}\right]$

The generalized Neumann boundary condition is defined by:

$$n \cdot (c\nabla u + \alpha u - \gamma) = g - qu + h^T \mu \qquad \text{(II-27)}$$

with g: the boundary source term, q: the boundary absorption coefficient and $h^T \mu$ is a reaction term which imposes the general constraint $R = 0$.

The Dirichlet boundary condition, used to specify a value of u on the boundary, is simply determined by:

$$u = r \qquad \text{(II-28)}$$

Finally, the magnetron discharge modelling from Costin's model is based on the resolution of a time-dependent system of five PDEs which includes the equation of Poisson, the charged

particles continuity, the mean energy transfer of electrons and the effective field for ions transport.

- Poisson's equation

The Poisson's equation allows the calculation of the discharge electric potential. This equation is part of classical PDE's in the mathematical module of COMSOL. However, these classical PDE's are not automatically included in the case of a 2D-axisymmetric configuration. In the model, the source term of this equation evolves according to the density of charged particles. It is thus defined in COMSOL by:

$$\nabla \cdot (-\nabla V) = -\frac{e}{\varepsilon_0}(n_i - n_e) \tag{II-29}$$

The variation of the electric potential gives the electric field which is necessary for the resolution of electrons transport and also effective field for the transport of ions:

$$\vec{\mathrm{E}} = -\nabla V \tag{II-30}$$

- Electrons continuity

The electrons density and electrons flux can be obtained by solving the following electrons continuity equation.

Referring to the Equation II-8, the components of the flux $\overrightarrow{\Gamma_e^1}$ can be expressed according to $\overrightarrow{\Gamma_e^0}$:

$$\begin{pmatrix} \Gamma_{er}^1 \\ \Gamma_{e\varphi}^1 \\ \Gamma_{ez}^1 \end{pmatrix} = \frac{1}{{f_{me}}^2 + {\Omega_\mathrm{e}}^2} \begin{pmatrix} -{\Omega_\mathrm{ez}}^2 & \Omega_{er}\Omega_{ez} \\ \Omega_{ez} f_{me} & -\Omega_{er} f_{me} \\ \Omega_{er}\Omega_{ez} & -{\Omega_\mathrm{er}}^2 \end{pmatrix} \begin{pmatrix} \Gamma_{er}^0 \\ \Gamma_{ez}^0 \end{pmatrix} \tag{II-31}$$

The equation of electrons continuity can thus be written as:

$$\frac{\partial n_e}{\partial t} + \nabla \cdot \left(\left(1 + \frac{1}{{f_{me}}^2 + {\Omega_\mathrm{e}}^2} \begin{pmatrix} -{\Omega_\mathrm{ez}}^2 & \Omega_{er}\Omega_{ez} \\ \Omega_{ez} f_{me} & -\Omega_{er} f_{me} \\ \Omega_{er}\Omega_{ez} & -{\Omega_\mathrm{er}}^2 \end{pmatrix} \right) \begin{pmatrix} \Gamma_{er}^0 \\ \Gamma_{ez}^0 \end{pmatrix} \right) = f_{iz} n_e \tag{II-32}$$

with $\overrightarrow{\Gamma_e^0} = -\mu_e n_e \vec{E} - \nabla(D_e n_e)$ the classical drift-diffusion flux of electrons.

- Electrons mean energy transfer

The resolution of the electrons mean energy transfer equation allows us to determine the electron mean energy ε_e according to the electrons density obtained with the previous equation. Values of ε_e are necessary for the application of many input data functions used in equations.

Referring to the equation (II-9), as for electrons flux, the components of the flux $\overrightarrow{\Gamma_{\varepsilon e}^{1}}$ can be written according to $\overrightarrow{\Gamma_{\varepsilon e}^{0}}$. Therefore, the equation of electrons mean energy transfer can be done by:

$$\frac{\partial n_e \varepsilon_e}{\partial t} + \nabla \cdot \left(\left(1 + \frac{1}{f_{me}{}^2 + \Omega_e{}^2} \begin{pmatrix} -\Omega_{ez}{}^2 & \Omega_{er}\Omega_{ez} \\ \Omega_{ez} f_{me} & -\Omega_{er} f_{me} \\ \Omega_{er}\Omega_{ez} & -\Omega_{er}{}^2 \end{pmatrix} \right) \begin{pmatrix} \Gamma_{\varepsilon er}^{0} \\ \Gamma_{\varepsilon ez}^{0} \end{pmatrix} \right) = -\overrightarrow{\Gamma_e} \cdot \vec{E} - \theta_e n_e \qquad \text{(II-33)}$$

with $\overrightarrow{\Gamma_{\varepsilon e}^{0}} = -\mu_{\varepsilon e} n_e \varepsilon_e \vec{E} - \nabla(D_{\varepsilon e} n_e \varepsilon_e)$.

- Ions continuity

By introducing an effective field, the ions flux can be written as a classical drift-diffusion formulation:

$$\overrightarrow{\Gamma_i} = \mu_i n_i \vec{E}^{eff} - \nabla(D_i n_i) \qquad \text{(II-34)}$$

Thus, the equation of ions continuity is expressed by:

$$\frac{\partial n_i}{\partial t} + \nabla \cdot \left(\mu_i n_i \vec{E}^{eff} - \nabla(D_i n_i) \right) = f_{iz} n_e \qquad \text{(II-35)}$$

- Effective field

The effective field is finally defined by:

$$\frac{1}{f_{mi}} \frac{\partial \vec{E}^{eff}}{\partial t} = \vec{E} - \left(1 + \frac{f_{iz}}{f_{mi}} \frac{n_e}{n_i} \right) \vec{E}^{eff} \qquad \text{(II-36)}$$

As previously presented in the theoretical model from Costin, boundary conditions are imposed on charged particles fluxes and electrodes applied voltage values.

In the Coefficient Form PDE interface, these boundary conditions can be defined by 'Flux/Source' and 'Dirichlet Boundary Condition' functions. Indeed, the 'Flux/Source' function, for boundary condition on fluxes, is determined for a variable u by:

$$-n \cdot (-c\nabla u - \alpha u + \gamma) = g - qu \tag{II-37}$$

with $\nabla = \left[\frac{\partial}{\partial r}, \frac{\partial}{\partial z}\right]$

For the resolution of Poisson's equation, the grounded anode and the applied voltage on the cathode V_0 are specified using Dirichlet condition.

Furthermore, a compensation term must be used in order to solve correctly in cylindrical coordinates the different PDEs with the COMSOL mathematics module. Indeed, the divergence of a vector u in a cylindrical 2D-axisymmetric system is expressed by:

$$\nabla \cdot u = \frac{\partial u_r}{\partial r} + \frac{u_r}{r} + \frac{\partial u_z}{\partial z} = \frac{1}{r}\frac{\partial (r u_r)}{\partial r} + \frac{\partial u_z}{\partial z} \tag{II-38}$$

with $u = [u_r, u_z]$

However, in the mathematics module and PDE interface it is actually defined by:

$$\nabla \cdot u = \frac{\partial u_r}{\partial r} + \frac{\partial u_z}{\partial z} \tag{II-39}$$

Therefore, the missing term related to the curvature of the coordinate system must be compensated in the different expressions of equations and boundary conditions.

3.4. Input data

The equations of the model include parameters which are defined in COMSOL as functions from data tables such as reduced mobility, reduced diffusion, momentum transfer frequency, collisions frequency and electrons energy loss rate.

The reduced coefficients of electrons and electrons energy fluxes such as $\mu_e N$, $\mu_{\varepsilon e} N$, $D_e N$ and $D_{\varepsilon e} N$ are obtained according to the electron mean energy ε_e from the Equations II-6, II-10, II-7 and II-11 respectively.

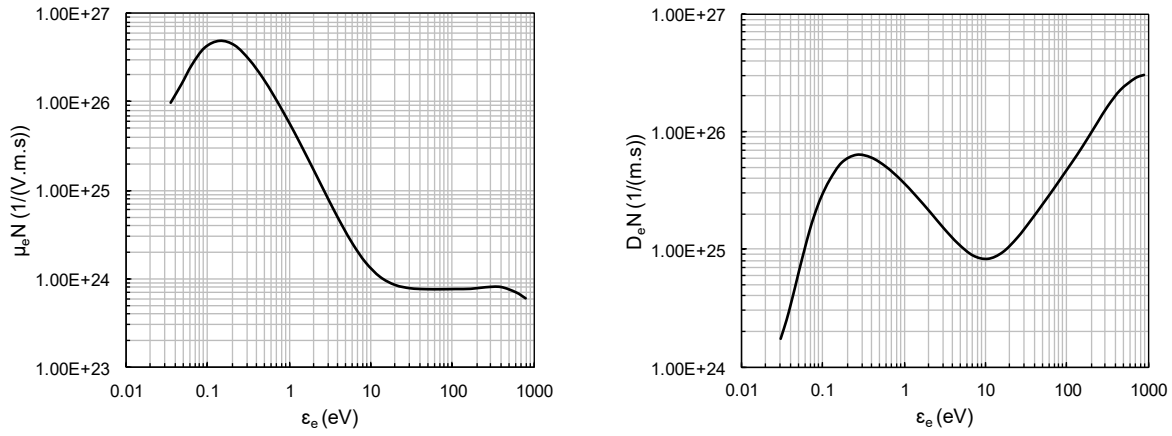

Figure 15: Reduced coefficients of electrons mobility (left) and diffusion (right).

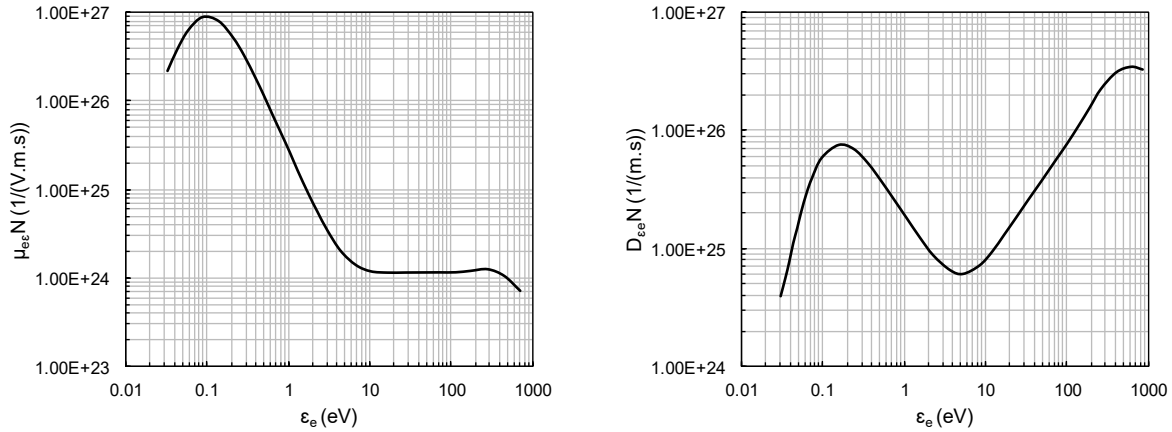

Figure 16: Reduced coefficients of electrons energy mobility (left) and diffusion (right).

These transport coefficients depend on the total momentum-transfer cross-section for electron-neutral collisions σ_{me}.

The total frequency of momentum transfer for electron-neutral collisions f_{me} can be determined from electrons mobility by:

$$f_{me} = N \frac{e}{m_e(\mu_e N)} \qquad \text{(II-44)}$$

The ionization frequency f_{iz} is thus defined from the fraction with f_{me} :

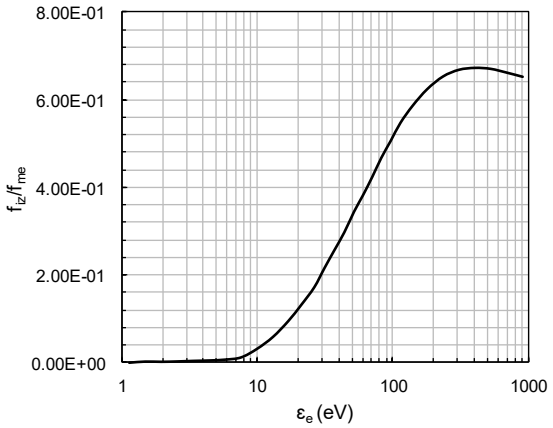

Figure 17: Value of f_{iz}/f_{me}.

Furthermore, the electron energy loss rate θ_e/N is also given according the electrons mean energy ε_e from the Equation II-13 by:

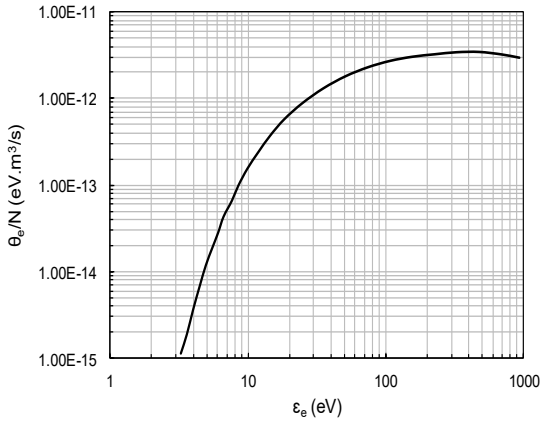

Figure 18: Electron energy loss rate.

The ions transport coefficients are solution of the reduced electric field E/N. However, the electric field E is replaced by the effective field E^{eff} in which ions are in equilibrium.

The reduced coefficient of ions diffusion D_iN can be obtained from ions reduced mobility μ_iN by:

$$D_iN = \mu_iN\frac{kT_i}{e} \qquad \text{(II-45)}$$

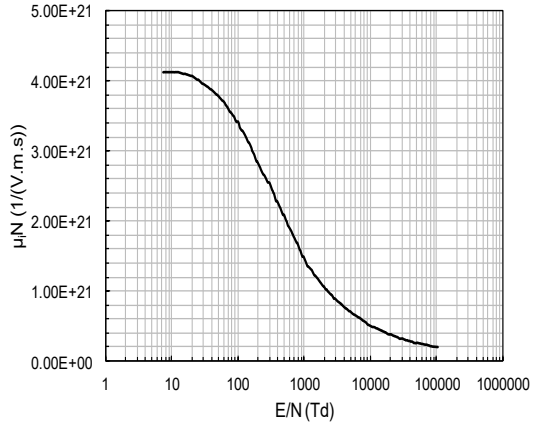

Figure 19: Ions mobility.

Moreover, the total frequency of momentum transfer for ions-neutral collisions f_{mi} can be determined by:

$$f_{mi} = N\frac{e}{m_i(\mu_i N)} \tag{II-46}$$

4. Results

The resolution of the model is composed of two studies as stationary for the magnetic field calculation and time-dependent for the treatment of charged particles and the electric potential. However, the solutions of the model are typically stationary. In fact, due to the highly non-linear and highly coupled system of equations, a time-dependent resolution is applied in order to help the solutions to converge to their stationary situation using flux expressions. The transport of charged particles is then characterized by the classical drift-diffusion fluxes. Moreover in a magnetron sputtering discharge, electrons are trapped in the magnetic field lines, thus implying a contribution of the magnetic field in the electrons transport equation by a flux containing the magnetic field.

In numerical simulations, the validation of a model is essential for its use in order to obtain coherent results close to the reality. Numerical results are therefore mainly compared to experimental results. In this work, the resolution of the model using COMSOL tool will be validate according to the results presented by Costin.

Different studies were carried out in order to verify the application of the model in COMSOL. The following results were obtained according to the model from Costin based on setting parameters of gas temperature T_{Ar} of 300 K, pressure p_0 of 10 mTorr and cathode applied voltage V_0 of -200 V [86].

4.1.Magnetic field

The magnetic field distribution depends on the magnets magnetization parameter and on the distance in which the magnetic device is active. We will relate the determination of this distance to the choice of the target thickness. The target material is considered non-magnetic. Hence, the target thickness d must therefore be chosen between 1.27 and 5.88 mm [83].
As the parameters are not specified by Costin, we chose to use a magnet magnetization of $M_0 = 915$ kA/m corresponding to the magnetization of magnets used in a reactor in GREMI. The characteristics of the magnetic fields resulting for the thicknesses of 1.27 and 5.88 mm are compared below to those corresponding to the magnetic field used by Costin.

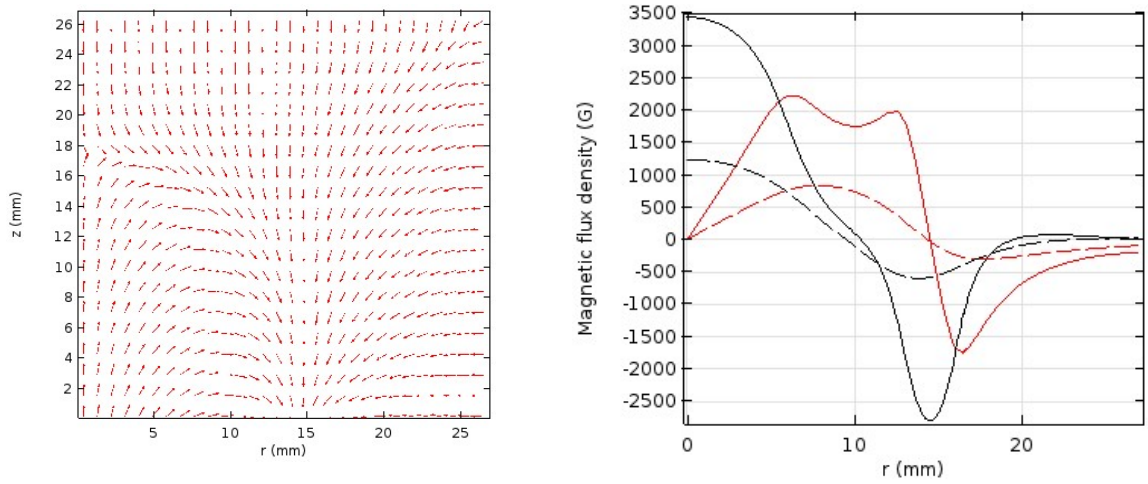

Figure 20: Magnetic field map (left) and radial variation of B_r in red and B_z in black (right) for d = 1.27 mm. The dashed lines represent Costin' results.

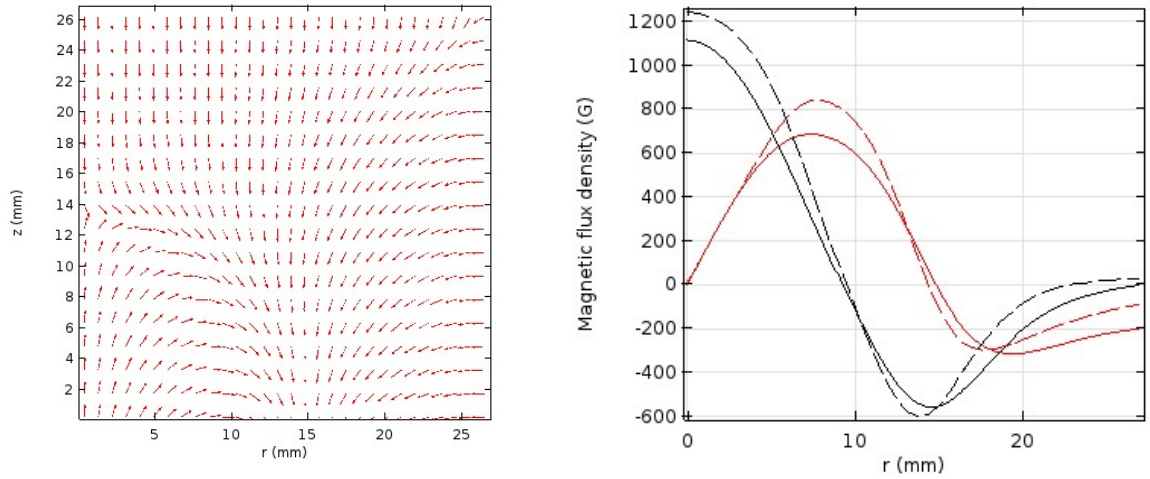

Figure 21: Magnetic field map (left) and radial variation of B_r in red and B_z in black (right) for d = 5.88 mm. The dashed lines represent Costin's results.

The strength of the magnetic field at the cathode surface increases when the thickness of the target is small. Moreover, by comparing the results obtained with those used by Costin, the strength of the magnetic field is higher with a target thickness of 1.27 mm and weaker with a thickness of 5.88 mm. Thus, the target thickness must be closer to 5.88 than 1.27 mm.

The figure below presents our results of the magnetic field that are closest to those of Costin.

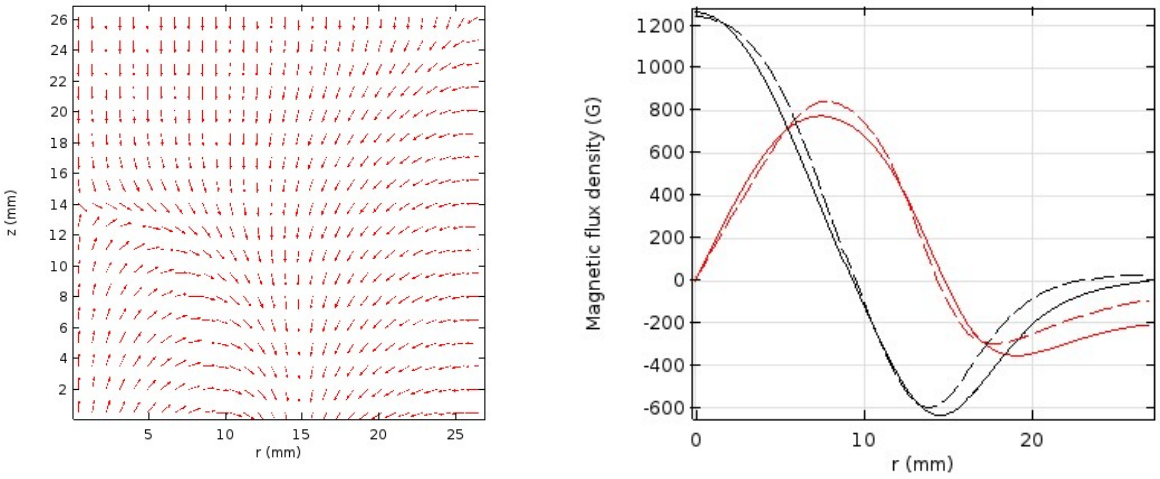

Figure 22: Magnetic field map (left) and radial variation of B_r in red and B_z in black (right) for d = 5.4 mm. The dashed lines represent Costin's results.

The magnetic field lines are parallel to the cathode surface at $r \approx 9.5$ mm. The components of magnetic field radial variation are similar to ones of Costin. The characteristics of this magnetic field will then be used as parameters for electrons transport in our model.

4.2. Electric potential

The discharge is created from an electric field determined by the gradient of the potential obtained according to the equation of Poisson. The Poisson's equation is one of the classical PDEs known in COMSOL. However, it is not directly implemented for 2D-axisymmetric geometry due to the missing term of the divergence which must be taken into account. The implementation of the equation must therefore be verified.

In the model, the Poisson's equation is a function of the charged particles densities variation ($n_i - n_e$). The **Figure 20** presents the electric potential obtained by Costin.

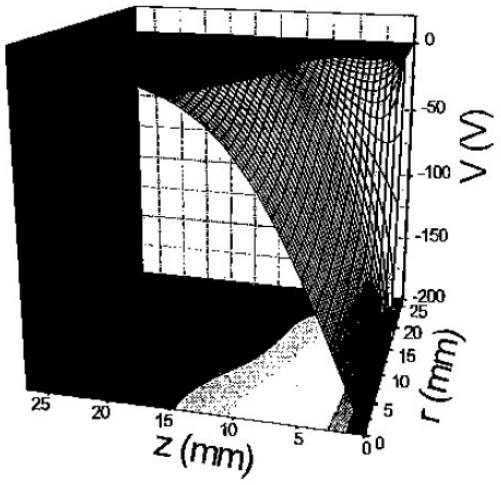

Figure 23: Costin's electric potential [86].

Initially, the density of ions and the density of electrons are considered equal ($n_i = n_e = 1.10^{14}$ m^{-3}). The electric potential is then obtained from $\Delta V = 0$.

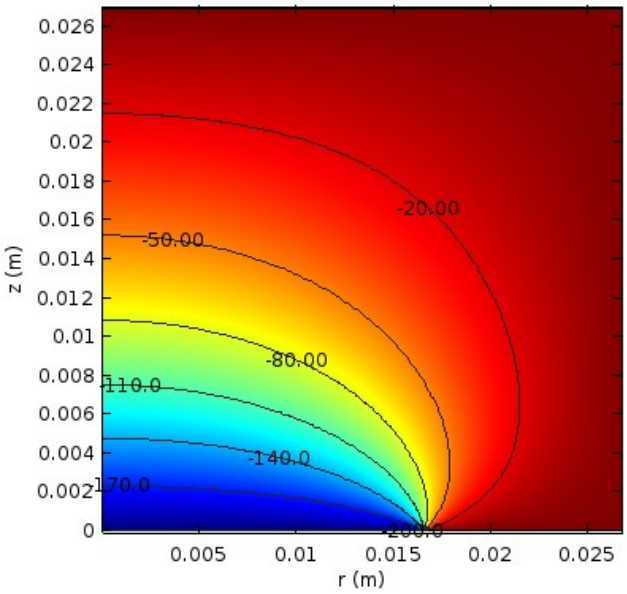

Figure 24: Initial electric potential.

The potential evolves linearly from the negative bias voltage of -200 V at the cathode to the grounded anode as we can observe in the following figure. The **Figure 25** plots the electric potential over a distance separating the cathode and the anode on the r-axis at z = 0.

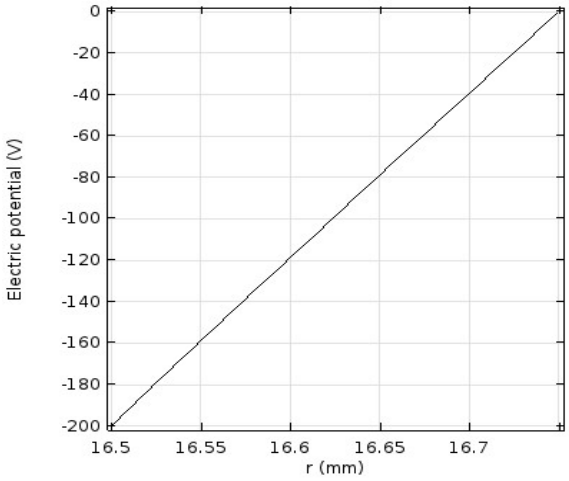

Figure 25: Evolution of the electric potential over the cathode-anode distance at z =0.

According to the **Figures 24** and **25**, the electric potential is initially correctly solved. However, this is true when considering the same density of electrons and ions.

In order to take into account the charged particles densities variation in our calculation and finally to validate the implementation and the resolution of the electric potential using COMSOL, we chose to integrate the charged particles densities obtained by Costin. This allows us to simplify the resolution of the equations system based on only one variable, here, the potential V.

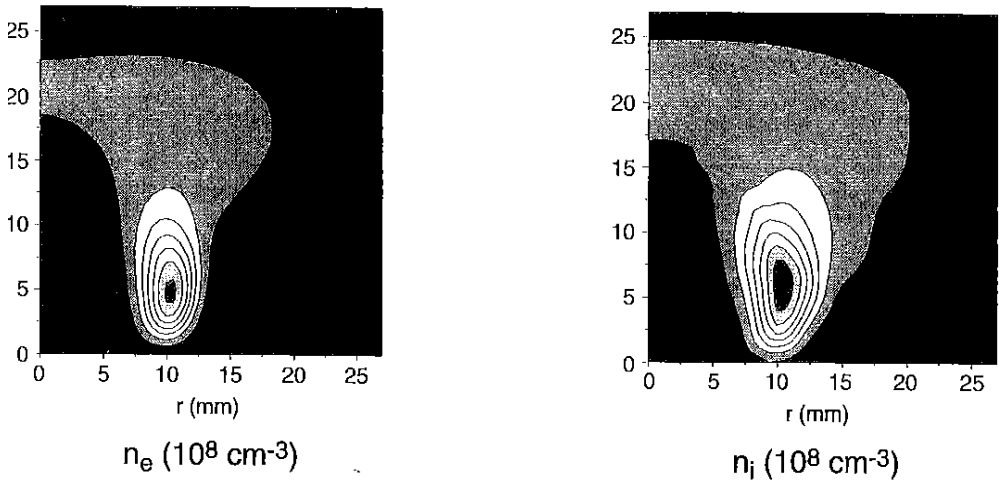

Figure 26: Costin's electrons density (left) and ions density (right) [86].

The densities from Costin's results were treated with Matlab® and set in COMSOL using the 'Image' tool. The input densities are then given by the **Figure 27**.

Figure 27: Electrons (left) and ions (right) densities input profiles.

By specifying the expression determining the color scale of the images, the charged particles densities used in our calculations are presented in the **Figure 28**.

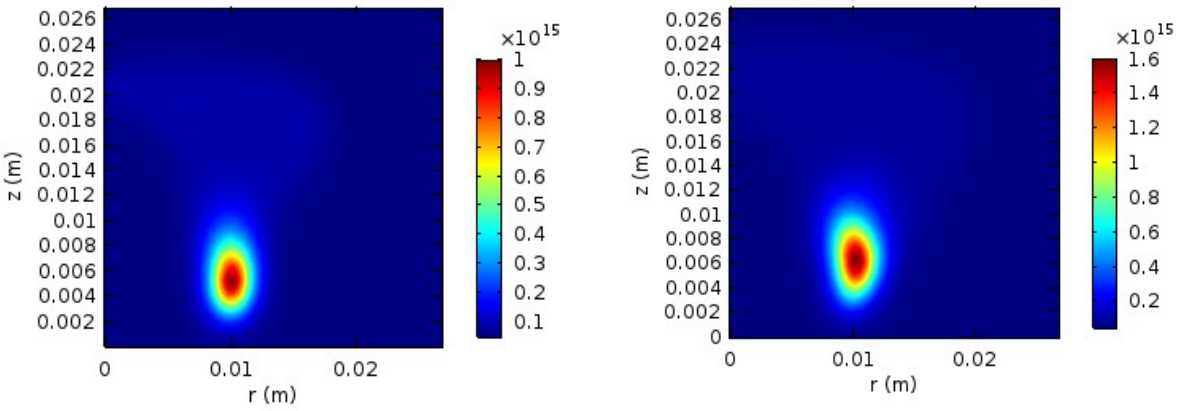

Figure 28: Input electrons (left) and ions (right) densities (1/m^3).

Finally, by considering the variation of the charged particles densities, the electric potential resulting from our calculation is similar to the one obtained by Costin (see **Figure 23**).
Thus, as presented in the **Figure 29**, the equation of Poisson of the model is correctly solved by the COMSOL solver.

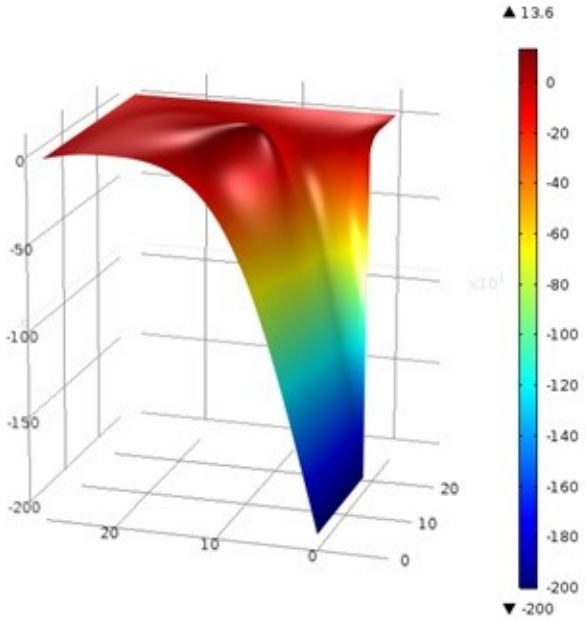

Figure 29: Electric potential distribution *V* (V).

The electric potential varies from -200 V at the cathode surface to 0 V for the grounded anode and is equal to a few volts depending on the charged particles densities variation where the electrons are trapped by the magnetic field thus increasing ionization.

4.3. Charged particles densities and electron mean energy

In the model, the discharge is described by the transport of electrons and ions based on the resolution of the moments of Boltzmann equation, such as continuity, momentum transfer and mean electron energy transfer. The system of equations contains five variables as the electric potential V, the electrons density n_e, the electrons energy density $n_e\varepsilon_e$, the ions density n_i and the effective field E^{eff} with which the ions are in equilibrium.

As the resolution of the electric potential has already been validated, also due to the few results presented by Costin, in this study, we will focused on the calculation of the charged particles densities and electrons mean energy. This will allow us to validate the implementation as well as the resolution of the charged particles continuity and the electrons mean transfer energy using COMSOL.

The charged particles densities obtained by Costin are presented in the previous **Figure 26** and the electrons mean energy is given in the **Figure 30** below.

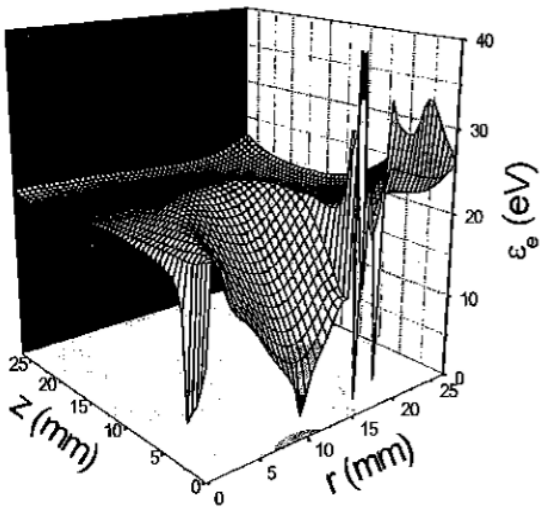

Figure 30: Costin's electrons mean energy ε_e (22 eV) [86].

The electrons mean energy is an important parameter in the resolution of equations. Actually, the electrons transport coefficients and properties of equations based on input data depend on it.

The resolution of the equations system is not the simplest, as presented in the **Figure 4**, due to the coupling of all the equations. The validation of the implementation of each equation in COMSOL is not possible without taking into account all the equations.

In order to help the system to converge to its solution, we chose to use the charged particles densities obtained by Costin as initial values. The initial electrons energy density is applied to $n_e\varepsilon_e = 2.2.10^{15}$ kg/m/s^3/A.

Thus, the charged particles densities and the electrons mean energy resulting from our calculations are presented in the following figures.

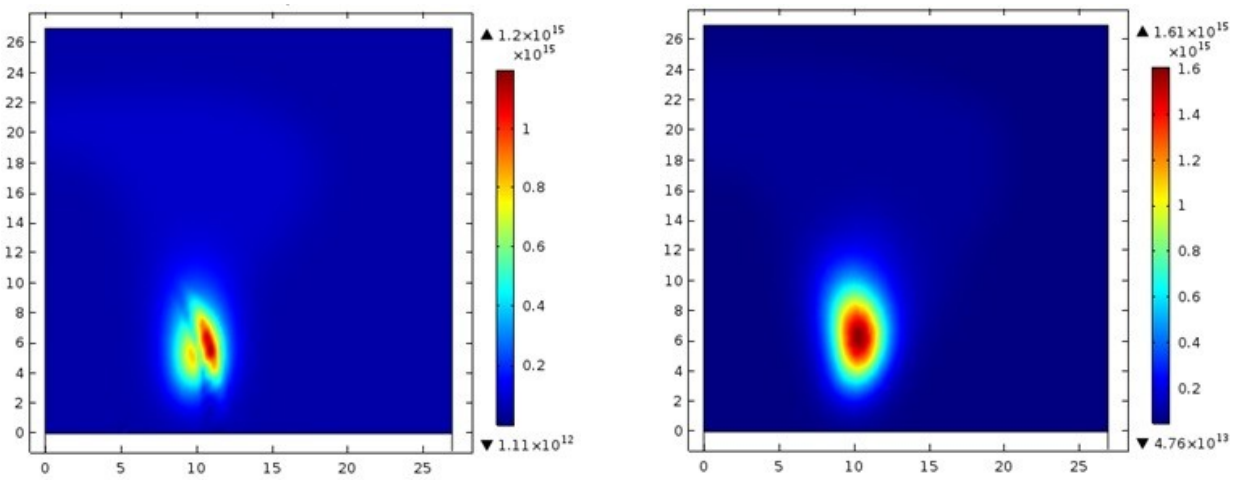

Figure 31: Electrons (left) and ions (right) densities (1/m^3).

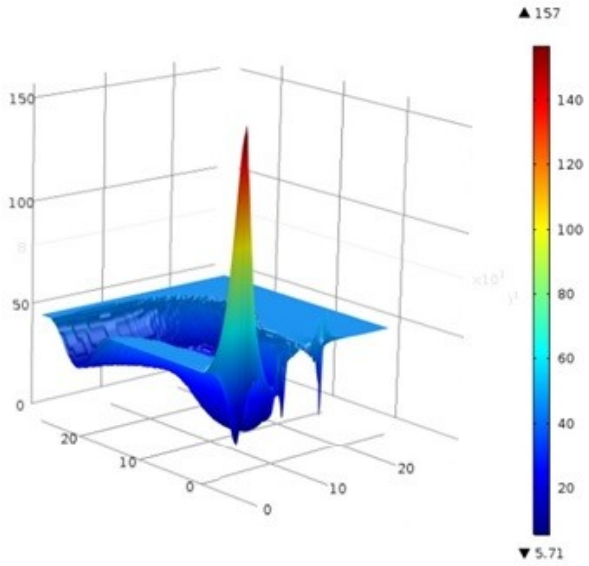

Figure 32: Electrons mean energy (eV).

By comparing the results obtained in the **Figures 31** and **32** with those presented by Costin in the **Figures 26** and **30**, modification of electrons density profile and high electrons mean

energy values (40 eV instead of 22 eV) can be observed. Moreover, above the cathode surface, the means energy reaches the anomalous value of 157 eV. These results could be explained by the contribution of a strong magnetic field to the electrons. Indeed, the contribution of the magnetic field to the electrons transport equation is important and makes the resolution of the electrons continuity and mean transfer energy more difficult. This did not allow us to perform our calculations until convergence to the stationary situation. Nevertheless, the calculations were performed for a physical time of 2 fs. This physical time is small compared to the ions velocity. Hence, the ions density obtained is similar to the initial one.

In order to study the influence of the magnetic field strength on the model we chose to apply two others magnet magnetizations values corresponding to $\frac{M_0}{10} = 91.5$ kA/m and $\frac{M_0}{100} = 9.15$ kA/m.

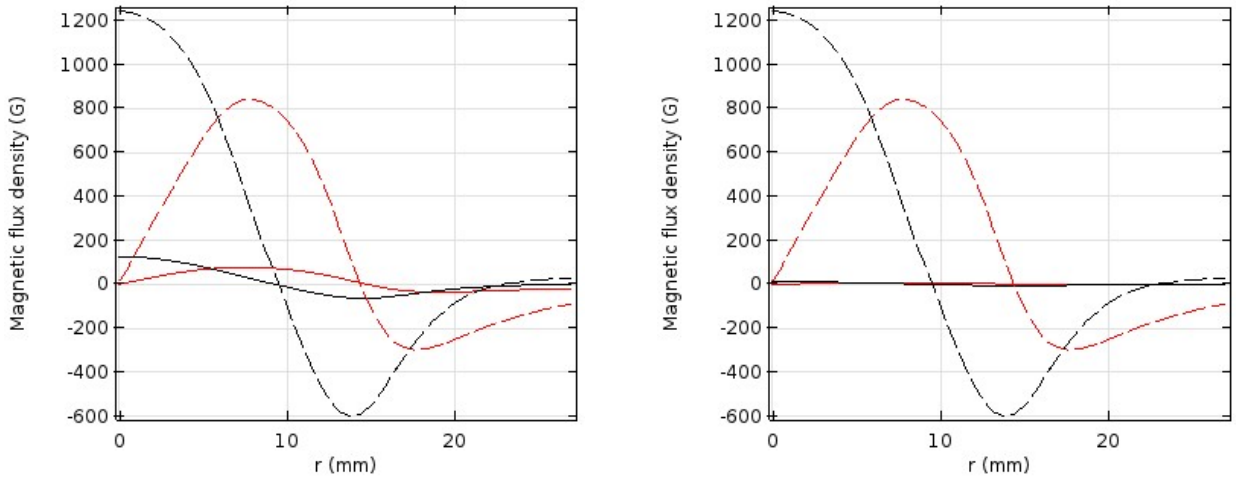

Figure 33: Radial variation of B_r in red and B_z in black for $M_0/10$ (left) and for $M_0/100$ (right). The dashed lines represent Costin's results

As presented in the **Figure 33**, the magnetic fields corresponding to these magnetization values are thus very small compared to the magnetic field used by Costin.

The charged particles densities and the electrons mean energy resulting from the calculations are given in the **Figures 34** and **35** for a magnets magnetization of 91.5 kA/m and in the **Figures 36** and **37** for a magnets magnetization of 9.15 kA/m.

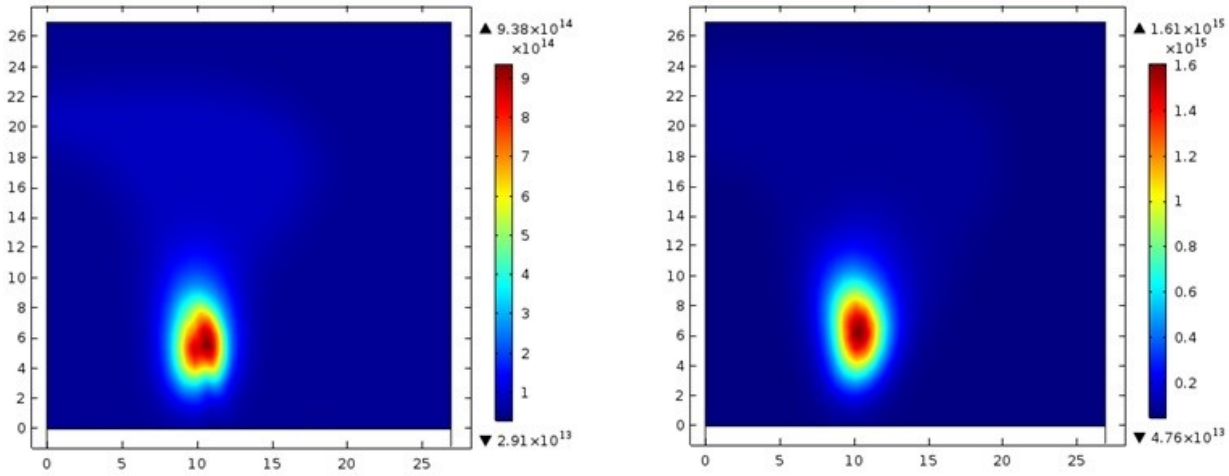

Figure 34: Electrons (left) and ions (right) densities for a magnetization of $M_0/10$ (1/m^3).

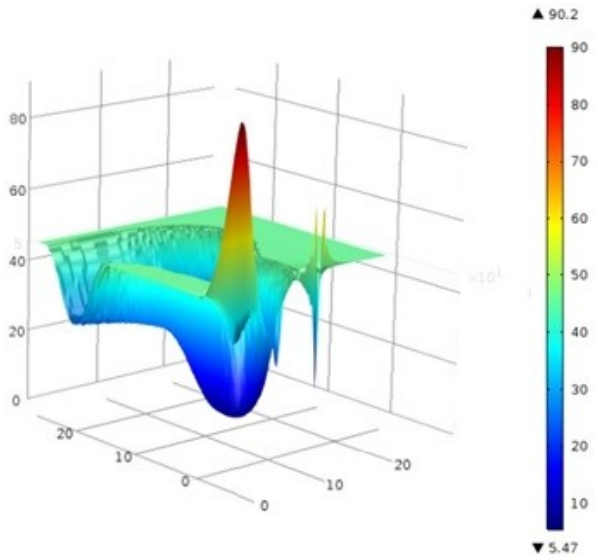

Figure 35: Electrons mean energy for a magnetization of $M_0/10$ (eV).

By dividing the magnet magnetization by 10, the calculations were performed for a physical time of 20 fs. The electrons density profile is slightly modified by the magnetic field lines and the electrons mean energy values are still high than those obtained by Costin. However, above the cathode surface, the value of the mean energy is 90.2 eV which is lower than those resulting with a magnets magnetization of 915 kA/m. The ions density is still similar to the initial one.

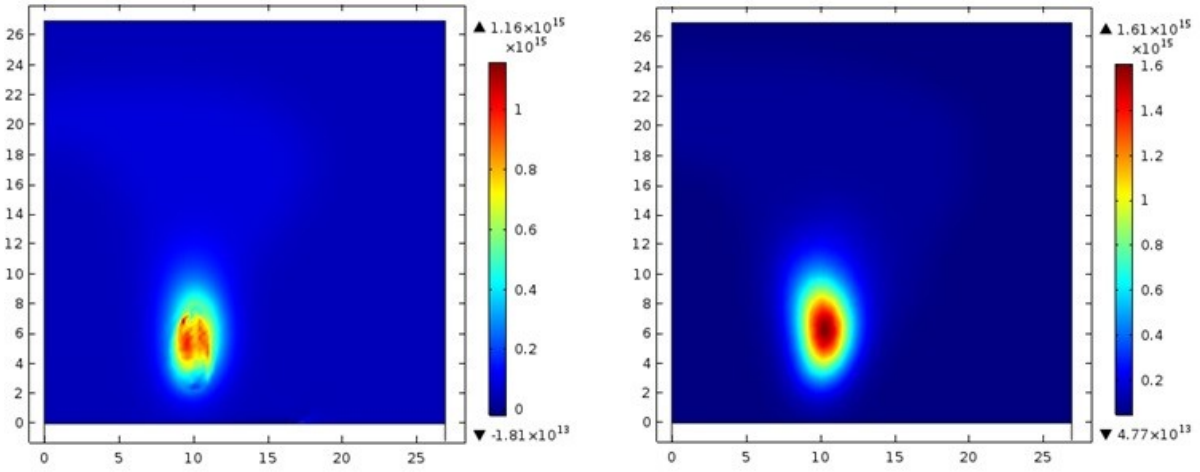

Figure 36: Electrons (left) and ions (right) densities for a magnetization of $M_0/100$ (1/m^3).

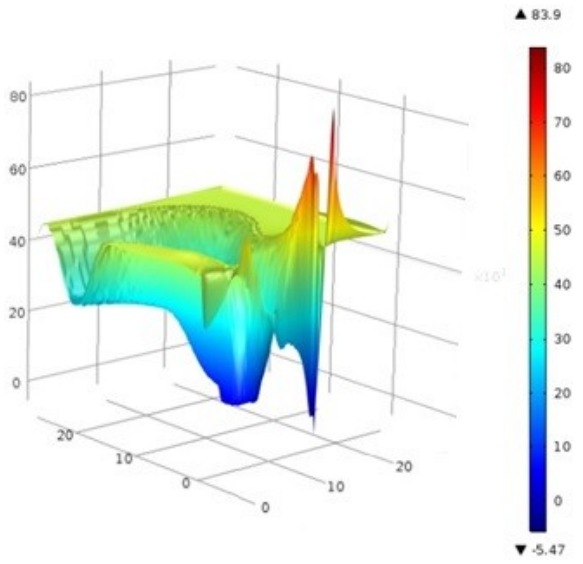

Figure 37: Electrons mean energy for a magnetization of $M_0/100$ (eV).

By dividing the magnetization by 100, the results are obtained according to a physical time of 2 ps. The electrons density is also modified by the magnetic field lines and the ions density does not change. The values of the electrons mean energy are higher than those presented by Costin. Moreover, the high values of electrons mean energy are located on the distance between the cathode and the anode according to z=0. This is similar to the results obtained by Costin. However these values are too high and negative values are also observed. This distance is characterized by important variations due to the electric field that affect the values

of electrons mean energy, such as negative values, and give therefore unrealistic results which also does not allows us to perform our calculations until convergence.

4.4.Conclusion

In this work, the magnetic field and electric potential calculation are correctly performed using COMSOL. Nevertheless, the calculation of charged particle transport remains questionable.

The resolution of equations such as charged particle continuity, electrons mean transfer energy and effective field cannot be study independently. As results presented by Costin correspond to charged particles densities and electron mean energy, we were focused on the first three equations. Due to the coupling of the non-linear equations, we chose to use charged particle densities obtained by Costin as initial values to help the results to converge to their stationary situation in order to validate the implementation and the resolution of the equations with COMSOL.

However, the electrons transport and electron mean transfer energy calculation limited our study. Indeed, the contribution of the magnetic field close to the one used by Costin did not allow us to perform the calculation until convergence and led to a physical time too small for ions transport treatment. In fact, a strong magnetic field implies high values of electrons mean energy in which parameters of electrons and ions transport equations are dependent. This could therefore distort the values of these parameters and give unrealistic results. Moreover, by decreasing the magnetic field strength, high values of electron mean energy above the cathode surface decrease. This allows us to observe high values of electrons mean energy on the short distance between the cathode and the anode at z=0. In this distance the variation of the electric potential is important. Therefore, negative values are also observed and do not allows the convergence of the system.

Finally, the resolution of the model is difficult due to highly non-linear and highly coupled equations system and also due to the solver used in COMSOL in which some adjustments could be necessary to help the system to converge.

5. Conclusion

The magnetron discharge model is implemented in COMSOL Multiphysics® based on the theoretical model from Costin which consists on a two-dimensional (r,z) time-dependent fluid model of an axis-symmetric DC planar magnetron discharge in argon [71, 83, 86].

Our interest to work with COMSOL software, in addition to the powerful solver that it is, is due to the possibility to apply the model on different geometries such as those of the reactor used for experiments. However, the simulation of plasma magnetron discharge is not recommended using COMSOL solver due to the strong anisotropy of electrons transport coefficient caused by the contribution of the magnetic field. Therefore, we chose to base on Costin's model because it presents some results with which we could compare in order to validate our calculations.

In this model, two types of charged particles are treated such as the electrons and the ions. The expression of electron flux is separated into two parts as classical drift-diffusion flux and a term which contains the magnetic field. The application of an effective electric field allows the classical drift-diffusion form for ions flux expression.

The resolution of the equations is presented according to two studies as stationary for the magnetic field calculation and time-dependent for the electric potential and the transport of charged particles.

In this work, we obtained a correct resolution of the magnetic field and the electric potential. Nevertheless, the charged particles transport equations showed limitations due to the contribution of a strong magnetic field. The difficulty to solve the model could be explained by the complexity of the system of equations and also by the black box that characterizes the COMSOL solver. Indeed, some adjustment in the solver could be necessary to perform a calculation. A comprehensive study especially on solver setting could therefore be interesting. Moreover, COMSOL solver is continually improved and could more easily solve the model in the future.

III. Sputtering erosion of Titanium

1. Introduction

Sputtering phenomena can be studied by the molecular dynamics approach, since the process is of atomic nature.

Indeed, molecular dynamics is a powerful tool which allows us to obtain the dynamics properties of a solid, liquid or gas system [112, 114, 115, 133, 134].

In this chapter, we work on MD simulations of sputtering erosion of a material with the example of titanium by argon ions bombardments using LAMMPS (Large-Atomic/ Molecular Massively Parallel Simulator) code[1]. The sputtering mechanism based on both physical and chemical processes is thus studied at atomic scale by MD allowing a description of plasma-surface interactions for a large number of atoms in a system. In addition, we are also interested in long time scale modelling by using a hybrid approach which combines MD and MC simulations.

Titanium material is interesting to use due to its properties of high mechanical strength, thermal stability, corrosion resistance and biocompatibility [9, 135]. Furthermore, coatings based on titanium, as titanium oxides (TiO_x) and nitrides, showed desirable properties for applications in fields as optic, electronic, mechanic or also as decorative coatings. The synthesis of titanium oxides thin films is much achieved by magnetron sputtering techniques for their properties of photocatalysis, semiconducting and refractivity such as those of titanium dioxide thin films (TiO_2) [11, 136–146].

[1] https://lammps.sandia.gov

Thus, we study the sputtering erosion of a pure titanium target in neutral gas with argon and in reactive gas composed by a mixture of argon and oxygen regarding the influence of the target temperature by mimicking a hot target [147, 148].

2. Molecular Dynamics

The technique of classical molecular dynamics allows the study of the dynamic of many-particle systems. The first published work using MD was realized by Alder and Wainwright in the late 1950s with the study of hard spheres interactions in a system [149–151].

Molecular dynamics became an effective tool for plasma-surface interactions modelling at the atomic scale and in a time scale up to the nanosecond. Thus, the sputtering process was first investigated with MD by Harrison and co-workers in the case of a copper target irradiated by Ar^+ and Xe^+ bombardments [152].

The method describes the motion of individual particles in time evolution by classical mechanics based on solving Newton's equations of motion [113]:

$$\overrightarrow{F_i} = m_i \overrightarrow{a_i} = m_i \frac{d\overrightarrow{v_i}}{dt} = m_i \frac{d^2\overrightarrow{r_i}}{dt^2} \quad \text{(III-1)}$$

where $\overrightarrow{F_i}$ is the force applied on atom i exerted by some external agent, m_i is the mass of the atom, $\overrightarrow{a_i}$ is the acceleration, $\overrightarrow{v_i}$ is the velocity and $\overrightarrow{r_i}$ is the position.

Therefore, a model is treated by MD according to the forces between atoms, particles positions, velocities and orientation in a defined (x, y, z) referential, in time evolution.

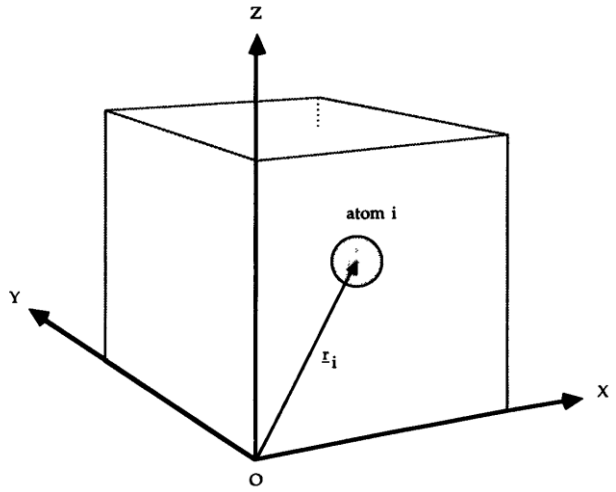

Figure 38: Cartesian, laboratory-fixed reference frame (X,Y,Z) used to define a position vector r_i that locates atom i in a system [151].

In molecular dynamics, the forces between particles are calculated at each time-step. The velocities and accelerations of individual particles are determined from forces in Newton's equations. The particles are then moved to new positions. Finally, a new atomic configuration is obtained where the forces are recalculated.
So MD simulations are calculating the full particle trajectories provided the forces at each times and initial positions and velocities are known.

2.1.Verlet algorithms

In molecular dynamics simulations, the most simple integration method, to calculate the particles trajectories, is the Verlet algorithm developed in 1967 [153].
This algorithm is based on the Taylor series expansions and gives at times $t + \Delta t$ and $t - \Delta t$ by:

$$\vec{r}(t + \Delta t) = \vec{r}(t) + \vec{v}(t)\Delta t + \frac{1}{2}\vec{a}(t)\Delta t^2 + \frac{1}{3!}\frac{d^3\vec{r}}{dt^3}\Delta t^3 + \cdots \quad \text{(III-2)}$$

$$\vec{r}(t - dt) = \vec{r}(t) - \vec{v}(t)\Delta t + \frac{1}{2}\vec{a}(t)\Delta t^2 - \frac{1}{3!}\frac{d^3\vec{r}}{dt^3}\Delta t^3 + \cdots \quad \text{(III-3)}$$

where $\vec{r}$ is the position vector, $\vec{v}$ is the velocity and $\vec{a}$ is the acceleration and Δt is the integration time step.
Then by summing the two equations, the velocity is cancelled and the position at time $t + dt$ is calculated by:

$$\vec{r}(t + \Delta t) = 2\vec{r}(t) - \vec{r}(t - \Delta t) + \vec{a}(t)\Delta t^2 \quad \text{(III-4)}$$

The Verlet algorithm is suitable for the study of conservative systems using positions and acceleration.
At each step the velocity is calculated by:

$$\vec{v}(t) = [\vec{r}(t + \Delta t) - \vec{r}(t - \Delta t)]/2\Delta t \quad \text{(III-5)}$$

This equation leads to a significant error, of the order of 1/1000, and causes small irregularities in the total energy which should be strictly constant in average [153].
Thus, the Velocity Verlet algorithm using positions, velocities and accelerations is most generally employed [154]:

$$\vec{r}(t+\Delta t) = \vec{r}(t) + \vec{v}(t)\Delta t + \frac{1}{2}\vec{a}(t)\Delta t^2 \quad \text{(III-6)}$$

$$\vec{v}(t+\Delta t) = \vec{v}(t) + \frac{1}{2}[\vec{a}(t) + \vec{a}(t+\Delta t)]\Delta t \quad \text{(III-7)}$$

This algorithm is known to be stable over very long times and only limited by machine truncation errors.

2.2.Interatomic potentials

The forces between particles are derived from their interatomic potential energies which are calculated from classical empirical potentials or force fields.
The time evolution of the system is then obtained by [114]:

$$\vec{F_i} = -\vec{\nabla}_{r_i} V\big(r_1(t), \dots, r_N(t)\big) = m_i \frac{d^2\vec{r_i}(t)}{dt^2} \quad \text{(III-8)}$$

where $V\big(r_1(t), \dots, r_N(t)\big)$ is the interatomic potential.
Thus, interatomic interactions are described by nonreactive or reactive potentials or force fields determined from quantum mechanics or chemistry taking into account the electronic structure of atoms.
Nonreactive potentials allow the modelling of interactions which are non-bonded and are reliable near equilibrium. Reactive potentials use bond-order concepts depending on the local chemical environment. These potentials allow dissociation and creation of chemical bond and thus are available for conditions far from equilibrium or for chemical change [155].
Firstly, two-body potentials or pair potentials have been developed as the Lennard-Jones (LJ) potential describing van der Waals interactions is the most popular used for liquids and polymers [116]:

$$V_{ij}(r_{ij}) = 4\varepsilon\left[\left(\frac{\sigma}{r_{ij}}\right)^{12} - \left(\frac{\sigma}{r_{ij}}\right)^{6}\right] \quad \text{(III-9)}$$

where ε is the minimum potential energy and σ is the distance where $V = 0$ corresponding to the hard sphere diameter.
Coulombics potentials also describe charged particles interactions. Thus, potentials as Molière or also ZBL, follow the universal form of the screened Coulomb potential which is given by [156]:

$$V(r) = Z_1 Z_2 e^2 \phi(r)/r \quad \text{(III-10)}$$

where Z_1 and Z_2 are the atomic numbers of the two colliding particles, e is the electron charge and $\phi(r)$ is the screening function.

These potentials are used for high energy particles, ions in plasma and laser-surfaces interactions modelling. In sputtering modelling, this type of potentials is adequate to describe the forces between atoms for models of collision cascade represented by a series of binary collisions [114].

Many-body potentials are expressed as a sum over interactions of more than two and three clusters nearby atoms in order to take into account many-body effects. Main relevant force fields are COMB (Charged-Optimized Many-Body) and ReaxFF (Reactive Force Field) force fields [157]. These two force fields have also the advantage to calculate the partial charge on each atom at each time step.

In order to describe the sputtering erosion of a titanium target in inert and in reactive gas, we chose to use the Molière potential for the interactions between Ar-Ti, Ar-Ar and Ar-O combined with the ReaxFF force field for Ti-Ti and Ti-O interactions.

2.1.1. Molière potential

The pairwise repulsive potential of Molière is obtained in the Thomas-Fermi statistical picture of the atom. It is thus written in a simple form of the screened Coulomb potential by [112], [116]:

$$V_M(r_{ij}) = \frac{Z_1 Z_2 e^2}{4\pi\varepsilon_0 r_{ij}} \sum_{i=1}^{3} c_i exp\left(-d_i \frac{r_{ij}}{a_F}\right) \quad \text{(III-11)}$$

where c_i, d_i and a_F are parameters the potentials screening functions with

$\{c_i\} = \{0.35, 0.55, 0.1\}$

$\{d_i\} = \{0.3, 1.2, 6.0\}$

determined by Bourque and Terreault for i ranging from 1 to 3 [156],

and $a_F = \frac{0.83\left(\frac{9\pi^2}{128}\right)^{1/3} a_B}{\left(Z_1^{1/2} + Z_2^{1/2}\right)^{2/3}}$ (III-12)

where the Bohr radius $a_B = 0.529177$ Å.

2.1.2. ReaxFF force field

ReaxFF has been chosen for this study, since it is well documented for Ti and TiO_2.
ReaxFF was developed by Van Duin and co-workers [158–160]. This method uses bond-order/bond-distance relations. The significant bond orders are kept at transition-state geometries. It allows the description of reaction process with bond formation and bond breaking according to realistic conditions and the investigation of the energies for various reactions intermediates, reactant and products.
The general expression of the total energy is given by [161]:

$$E_{system} = E_{bond} + E_{over} + E_{under} + E_{lp} + E_{val} + E_{vdWalls} + E_{Coulomb} \quad \text{(III-16)}$$

where E_{bond} are bond energies, E_{over} and E_{under} are respectively energies to penalize overcoordination and to stabilize undercoordination of atoms, $E_{lp}$are the lone pair energies, E_{val} are valence angle energies, $E_{Coulomb}$ and $E_{vdWalls}$ are terms to handle nonbonded Coulomb and van der Waals interaction energies.
E_{bond}, E_{over}, E_{under}, E_{lp} and E_{val} are dependent on bond order and on the local environment of each atom. The Coulomb energy is calculated according to a geometry-dependent charge distribution which is determined from the electronegativity equalization method. The van der Waals energy also includes the nonbonded interactions of short-rage Pauli repulsion and long-range dispersion.
Parameters of Ti/O are treated in ReaxFF force fields from Monti and co-workers in a study of adsorption of glycine (Gly) on TiO_2 [162] and Kim and co-workers in a study of TiO_2 nanoparticles of anatase and rutile surfaces interactions with water, methanol, and formic acid [161]. From these parameters, Huygh and co-workers developed a force field for TiO_2-system which includes intrinsic point defects [163].

2.3. Thermostat

The sputtering process by MD and the sputtering yield results then obtained depend on the forces between the particles of the system and more precisely on the accuracy of the

interatomic potentials which are applied. Nevertheless, parameters of energy and ions accumulation in the target can cause fluctuations and must therefore be treated in order to properly model the process [114].

Modelling sputtering consists in releasing ions towards a surface (called the target) with a high enough velocity corresponding to the ion energy gained due to the bias voltage of the target. Thus, the velocity applied to ions is determined from the expression of the kinetic energy:

$$E_c = \frac{1}{2}mv^2 \quad \text{(III-17)}$$

where m and v are respectively the mass and velocity of the incoming ion.

Ions must be placed at a distance larger than the cutoff length above the surface of the target and are typically directed normal to the target in order to mimic their driven motion due to the bias induced electric field.

At each impact, the energy of the bombarding ion is transferred to the surface of the target and induces collision cascades which subsequently leads (or not) to the ejection of surface target atom(s).

At equilibrium, the temperature of the system is given by statistical mechanics:

$$\frac{3}{2}Nk_BT = \sum_i \frac{1}{2}m_i v_i^2 \quad \text{(III-18)}$$

where N is the number of atoms, k_B is the Boltzmann constant, m_i and v_i are the mass and velocity of the atom i.

A bombarding ion, when it obtains sufficient kinetic energy, can penetrate into the surface of the target and implant after impact. Therefore, the collisions with the target atoms will transform this energy into heat which is, in reality, dissipated by the lighter particles.

Actually, in simulation, the boundaries of the system can be used to dissipate this heat. However, the use of periodic boundaries does not allow it. Thus, the application of thermostats allows controlling the temperature of the particles as with the Langevin thermostat, used in our models, or also the Berendsen thermostat [164–166]. Moreover, it is necessary to choose a target sufficiently thick to prevent the collisions affect the atoms at the bottom of the target, thus allowing a correct description of collisions cascades.

The Langevin thermostat consists on a heat bath to regularize the temperature of a group of atoms. Indeed, it mimics collisions between the particles and much lighter particles with a Maxwellian velocity distribution at a given reference temperature. Thus, the equations of

motion associated to the particles are coupled with Langevin equations as given below by Schneider and Stoll [164, 167]:

The model is defined by a Hamiltonian for the conservation of the energy. The assumed collisions are described by a friction $-\Gamma p_l$ and a random force $\eta_l(t)$.

$$M\ddot{X}_l = -\frac{\delta\mathcal{H}}{\delta X_l} - \Gamma M\dot{X}_l + \eta_l(t) \quad \text{(III-19)}$$

where

$$\langle\eta_l(t)\eta_l(t')\rangle = 2M\Gamma k_B T\delta_{ll'}\delta(t-t') \quad \text{(III-20)}$$

M is the mass of the particle l, X_l, $\dot{X}_l$ and $\ddot{X}_l$ are position, velocity and acceleration, $\mathcal{H}$ is the Hamiltonian of the ferrodistortive model, k_B is the Boltzmann constant and T is the temperature of the bath.

According to the Langevin equation, the system must evolve in a time interval which is larger than $1/\Gamma$. Thus, in order to reduce the dynamic modifications and to conserve the energy, the damping term Γ must be chosen according to:

$$1/\Gamma \gg \tau_c \quad \text{(III-21)}$$

where τ_c is the characteristic times of the dynamics which can be chosen as the electron-phonon coupling time α in the case of free electron metals [168]:

$$\alpha = \frac{\Theta_D T_e L n e^2 k_B Z}{2m_e \kappa \varepsilon_F} \quad \text{(III-22)}$$

where Θ_D is the Debye temperature, T_e is the temperature of electrons, L is the Lorentz number, n is the density of electrons, e is the electron charge, Z is the valence, m_e is the electron mass, κ is the thermal conductivity and ε_F is the Fermi energy.

3. Combining MD/MC simulations

Molecular dynamics is a powerful technique of simulation well known for the dynamical behavior description of a system at atomic scale. This technique is widely used for material modeling such as in the synthesis of materials. However, the evolution of a material between different states of equilibrium i.e. the relaxation to equilibrium can be a very time-consuming

process. Moreover in MD simulations, the time step is limited due to the need to conserve energy and events can evolve in the range of picoseconds to nanoseconds. Therefore, it was desirable to find a method accelerating MD.

Monte Carlo techniques allow faster approach to equilibrium compared to molecular dynamics. Hence, the combination of MD simulations with MC is interesting to use in order to take into account longer timescale relaxation processes in a reduced number of numerical iterations [169].

Thus, the tfMC technique (time-stamped force-bias Monte Carlo), based on force-bias Monte Carlo (fbMC) method, is an alternative to the molecular dynamics derived from stochastic approaches and easily to implement in a MD simulation code.

3.1. Monte Carlo

The Monte Carlo simulations are based on the condition described by Neyts and Bogaerts as follow [169]:

$$W(r'|r)P(r) = W(r|r')P(r') \quad \text{(III-23)}$$

where $W(r'|r)$ is the transition probability of the particle to go from position r to position r', $P(r)$ is the probability of finding a particle at position r. If P follows a Boltzmann distribution, then:

$$\frac{W(r'|r)}{W(r|r')} = exp(-\beta \Delta U) \quad \text{(III-24)}$$

with $\beta = \frac{1}{k_B T}$

where ΔU is the change in potential energy of the system due to the displacement. W can be rewritten as:

$$W(r'|r) = A(r'|r)T_c(r'|r) \quad \text{(III-25)}$$

where $T_c(r'|r)$ is the probability distribution of new position r' from the old position r and $A(r'|r)$ is the probability of accepting this new position:

$$A(r'|r) = min[1, q(r'|r)\,] \quad \text{(III-26)}$$

where the quantity q is defined by:

$$q(r'|r) = \frac{T_c(r'|r)}{T_c(r|r')} exp(-\beta \Delta U) = \frac{T_c'}{T_c} exp(-\beta \Delta U) \quad \text{(III-27)}$$

The acceptance of the displacement from r to r' of a particle is determined by the value of q. The Metropolis Monte Carlo (MMC) technique defines T_c as:

$$T_c = \begin{cases} c & \text{if } r' \in D(r) \\ 0 & \text{if } r' \notin D(r) \end{cases} \quad \text{(III-28)}$$

where c is a constant and $D(r)$ is the domain of displacement. The quantity q is then given by:

$$q = exp(-\beta \Delta U) \quad \text{(III-29)}$$

The Equations III-26 and III-29 show that when $\Delta U < 0$, the displacement is always accepted and when $\Delta U > 0$ the probability of accepting the displacement is equal to $exp(-\beta \Delta U)$.

3.2. Force-bias Monte Carlo

The force-bias Monte Carlo approach is based on probabilistic description of the atomic motion by considering the forces acting on particles.

Different algorithms of fbMC have been developed in order to have a higher atomic displacement acceptance probability to MMC and to allow the system to reach the equilibrium more quickly. This method was first presented in simulations of water by Pangali and co-workers [170].

In fbMC, the transition matrix is written according to the x-coordinate as [169]:

$$T_{c,x} = \begin{cases} K_x^{-1} exp(\lambda \beta F_x \delta_x) & \text{if } x' \in D(x) \\ 0 & \text{if } x' \notin D(x) \end{cases} \quad \text{(III-30)}$$

where K_x^{-1} is a normalization constant, λ is a arbitrary parameter, $F_x$is the x-component of the force at position x and δ_x is the displacement given by $\delta_x = x' - x$.

If the domain $D(r)$ is represented by a cube centered around $r = (x, y, z)$ and sides $2\Delta \times 2\Delta \times 2\Delta$, then each displacement in a direction v is limited:

$$-\Delta \leq \delta_v \leq \Delta \quad \text{(III-31)}$$

Then, the displacement can be written as:

$$r' = r + \xi \cdot \Delta \tag{III-32}$$

The components $\xi_v \in [-1,1]$ from the vector $\xi = \{\xi_x, \xi_y, \xi_z\}$ can be computed based on a random number $\eta \in [0,1]$ as

$$\xi_v = \frac{1}{\gamma_v} ln\left[\eta\left(e^{|\gamma_v|} - e^{-|\gamma_v|}\right) + e^{-|\gamma_v|}\right] \tag{III-33}$$

$$\gamma_v = \lambda \beta F_v \Delta \tag{III-34}$$

Then in a study of the growth of amorphous silicon, Dereli proposed a modified method, the continuum Monte Carlo method, in which the transition of an atom is always accepted by using $\lambda = 1/2$ [171]. Grein and co-workers used this method for epitaxial growth simulation and called it dynamic Monte Carlo [172]. Finally, Timonova reviewed the method and thus the uniform-acceptance force-bias Monte Carlo (UFMC) method allows the simulation of physical processes in a reduced number of iterations compared to MD [173–175].

The time-stamped force-bias Monte Carlo is a method of fbMC derived from UFMC and basic thermodynamic principles. This approach, suggested by Mees and co-workers [176], includes an estimation of the effective time scale of the simulation. A simulation can be accelerated by tfMC according to the system and the process employed [177].

The conditional displacement probability of each atom i according to the Cartesian direction j is given by Bal and Neyts by [177]:

$$p(\xi_{i,j}) = \begin{cases} \frac{e^{\gamma_{i,j}\left(2\xi_{i,j}+1\right)} - e^{-\gamma_{i,j}}}{e^{\gamma_{i,j}} - e^{-\gamma_{i,j}}} & \xi_{i,j} \in [-1,0[\\ \frac{e^{\gamma_{i,j}} - e^{\gamma_{i,j}\left(2\xi_{i,j}-1\right)}}{e^{\gamma_{i,j}} - e^{-\gamma_{i,j}}} & \xi_{i,j} \in]0,1] \end{cases} \tag{III-35}$$

A pair of random number (ξ_v, p) is generated for each direction v, with $\xi_v \in [-1,1]$ and $p \in [0,1]$ for all atoms. If $p(\xi_v) > p$, the displacement of the atom is accepted and its new position is $r_{v,new} = r_{v,old} + \Delta\xi_v$ else if $p(\xi_v) < p$, a new random pair (ξ_v, p) is generated and its acceptance is reevaluated.

$$\gamma_{i,j} = \frac{F_{i,j}\Delta_i}{2k_B T} \tag{III-36}$$

The maximal displacement length Δ_i of an atom i is calculated from a system-wide parameter Δ, the mass of the atom m_i and the mass of the lightest element in the system m_{min}:

$$\Delta_{\mathrm{i}} = \Delta\sqrt{\frac{m_{min}}{m_i}} \quad \text{(III-37)}$$

Particularly in tfMC method, the notion of time can be expressed and allow a quantitative comparison with molecular dynamics [176]. Thus, the expression of the statistical time step per Monte Carlo iteration is given by:

$$\langle \Delta t \rangle = \frac{\Delta}{3} \cdot \sqrt{\frac{\pi m_{min}}{2k_B T}} \quad \text{(III-38)}$$

Δ is the maximal displacement length of the lightest element in the system and must be sufficiently small in order to comply with detailed balance [177]. In general, the value of Δ is between 5 and 10% of the nearest neighbor distance.

4. Simulations

This work focuses on the modelling of titanium sputtering by argon ions of various energies, in neutral and in reactive gas with oxygen, by MD and by combining MD with MC simulations.

The simulations are performed using LAMMPS GNU open-source code and KOKKOS package. LAMMPS, standing for Large-Atomic/ Molecular Massively Parallel Simulator, is a classical molecular dynamics program designed to run on parallel computers [111]. The KOKKOS package in LAMMPS allows running efficiently on different hardware the commands of pair, fix and atom styles. Moreover, it allows adjusting the memory layout of basic data structures used to store the atom coordinates, the forces or the neighbor lists for these commands, in order to optimize the performance of the computing system.

4.1. Model configuration

The model is composed of a target formed by 12000 titanium atoms, modelled by a (100) hexagonal closed packed crystal box of 15 × 10 × 20 lattice units cell which equal to 44.070 × 50.888 × 95.955 $Å^3$. This latter is delimited in two regions. The first is composed by 2 layers of immobilized atoms, for preventing substrate motion due to momentum transfer from ion

impact. In the second region, the temperature is sequentially controlled by the Langevin thermostat. The target thermal relaxation is fixed to 1.2 ps as calculated from Equation III-22. Argon ions are randomly created to impact the surface of the target. These ions are generated every 24000 timestep for MD simulations and every 29000 timestep by combining MD/MC, at a height of 38.382 Å above the target.

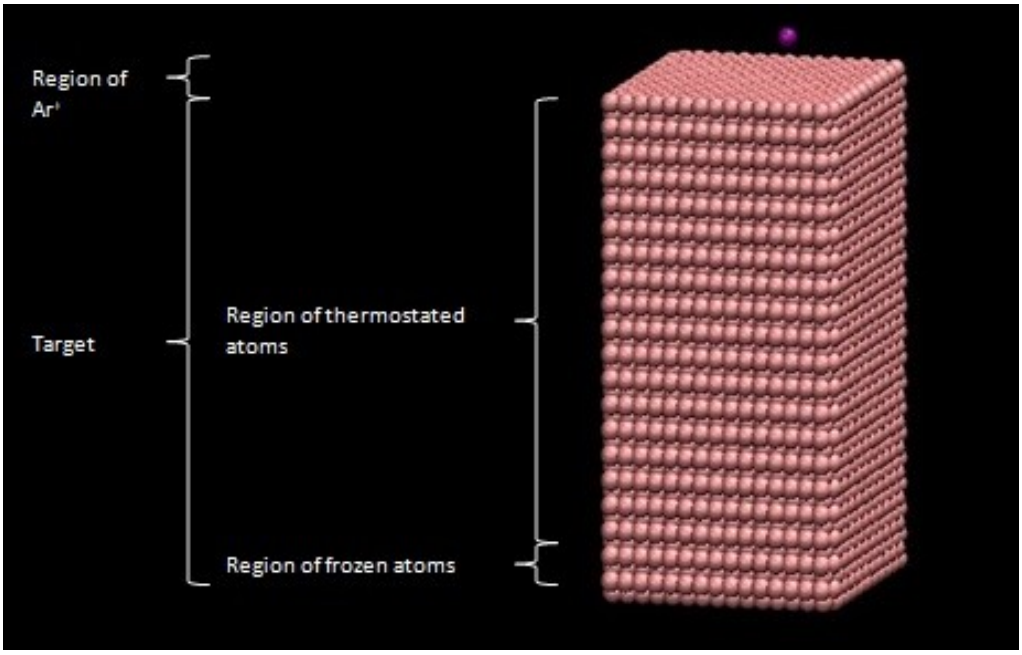

Figure 39: Initial configuration of the simulation of Ti sputtering. The color spheres of pink and purple represent Ti and Ar^+ respectively.

In the presence of a gas phase, these ions are placed at a height between 287.864 and 359.830 Å above the target.

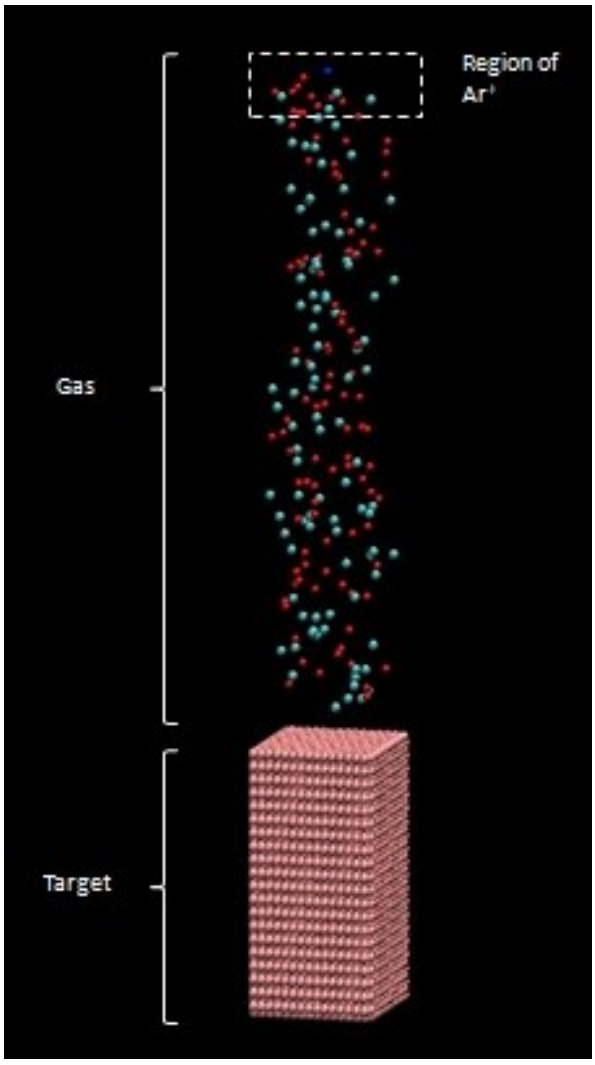

Figure 40: Initial configuration of the simulation of Ti reactive sputtering. The gas phase is composed of argon and oxygen. The color spheres of pink, red cyan and blue represent Ti, O, Ar and Ar^+ respectively.

The initial velocity of these ions is applied according to three kinetic energies of 200, 300 and 400 eV corresponding respectively to 311 $Å.ps^{-1}$ (0.311 $Å.fs^{-1}$), 381 $Å.ps^{-1}$ and 440 $Å.ps^{-1}$. These kinetic energies were chosen from the determination of the integration time step presented in the next subpart.

The velocities of the titanium target atoms follow a Maxwell-Boltzmann distribution at a target temperature of 300 K. Temperatures of 1000 and 2000 K are also chosen in order to study the influence of the target temperature on sputtering in the case of a hot target.

Furthermore, by considering a gas phase, the velocities of the atoms composing the gas are also chosen according to a Maxwell-Boltzmann distribution at a gas temperature of 300 K.

The maximum ion impact considered in this study is 100. It is a compromise between large computational time due to the reactive force fields and a reasonable precision of the obtained results. For example sputtering yields and retention rates precision is also due to the impact number. Statistical error is written as $\frac{\sqrt{N}}{N}$ where N is the ion impact number. So at 50 impacts error is 14% and at 100 impacts it is 10%.

The interactions between Ar-Ar and Ar-Ti and Ar-O are described using the Molière potential and the ReaxFF force field from Kim and van Duin is used for Ti-Ti, O-O and Ti-O interactions [161].

4.2. Time step

Some care must be taken in the choice of the integration time step. In fact, this parameter is limited by the requirement of energy conservation. The **Figure 41** represents the maximal deviation of the total energy of the system obtained after one impact, without thermostat application, for sputtering ion energies of 50, 100, 200, 300, 400, 500, 600 and 700 eV.

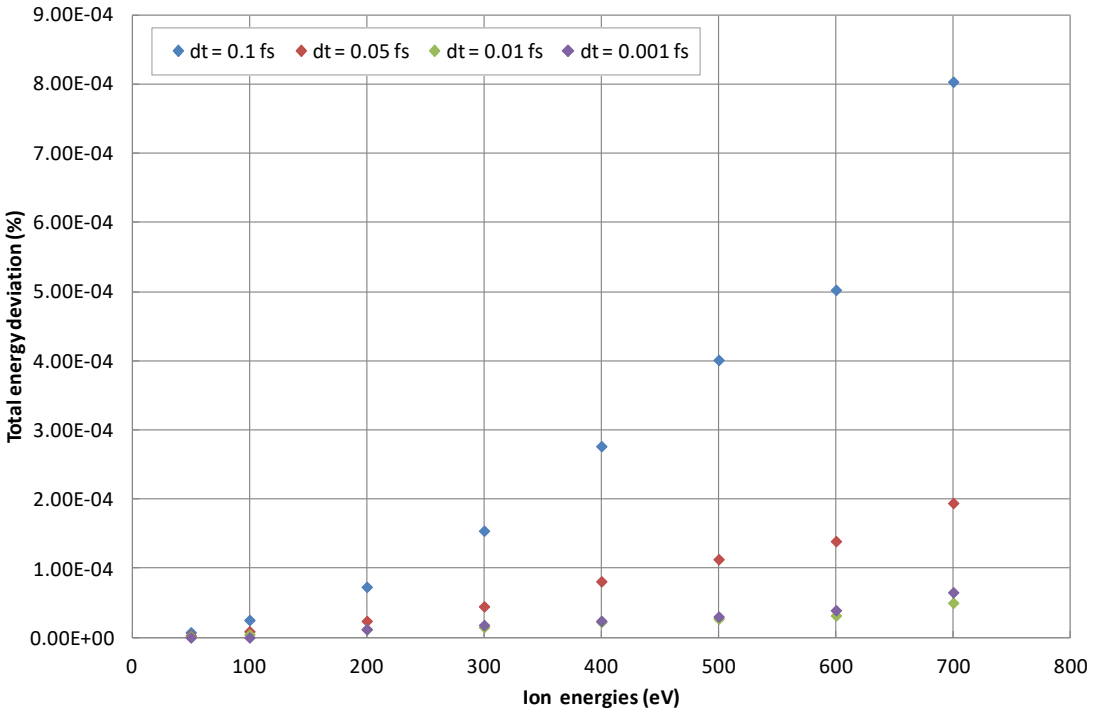

Figure 41: Maximum deviation of the total energy after impact for the different energies.

The deviation of the total energy is calculated by:

$\frac{|E_i - E_0|}{E_0} \times 100$ (III-39)

where E_i is the total energy given at time i and E_0 is the total energy at t = 0.

The maximum energy deviation must be smaller than 10^{-4}% to determine the applicable time steps for the corresponding energies. Therefore, in the **Figure 41**, the timestep must be smaller than 0.1 fs for energies of 50 and 100 eV, 0.05 fs for energies from 200 to 400 eV and 0.01 for energies from 500 to 700 eV.

The resulting computation times for each of these simulations are given below.

Energy	timestep	wall time
50 eV	0.1 fs	00:30:40
100 eV	0.1 fs	00:30:15
200 eV	0.05 fs	01:31:21
300 eV	0.05 fs	01:31:10
400 eV	0.05 fs	01:30:17
500 eV	0.01 fs	02:31:16
600 eV	0.01 fs	02:30:27
700 eV	0.01 fs	02:30:59

Figure 42: Computing time for one impact.

By taking into account the schemes of our simulations and the number of incoming ions which will be included in the calculations, we choose to base our model on the three kinetic energies of 200, 300 and 400 eV.

4.3.MD simulations

The time development of MD simulations follows the scheme below:

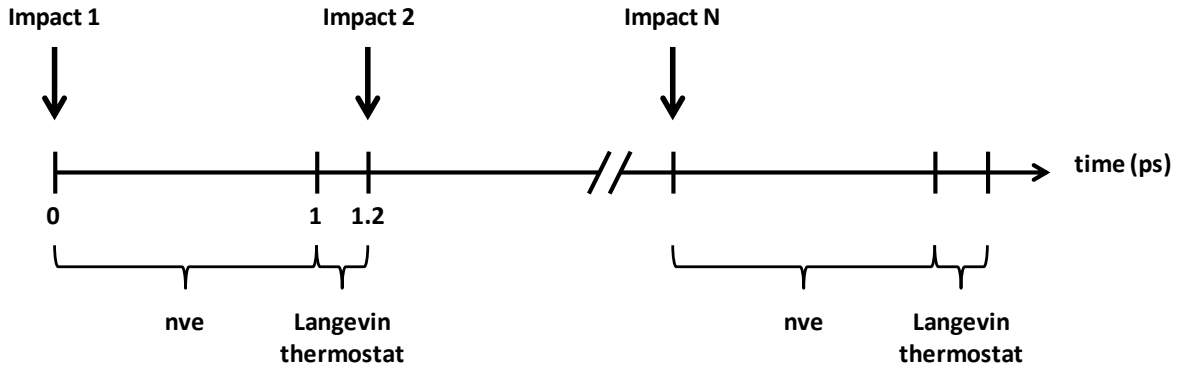

Figure 43: Sketch of the MD sputtering simulation target.

From impact, during NVE, the positions and the velocities of atoms are updated at each timestep according to the second law of Newton which preserve the total number of atoms (N), the volume of the system (V) and the total energy (E). The target temperature may rise due to collision cascade or ion implantation after impact. Therefore, the Langevin thermostat is then applied as heat bath to dissipate accumulated heat before the next impact.

4.4.Combining MD/MC simulations

By combining MD and MC, the simulations follow the following time scheme:

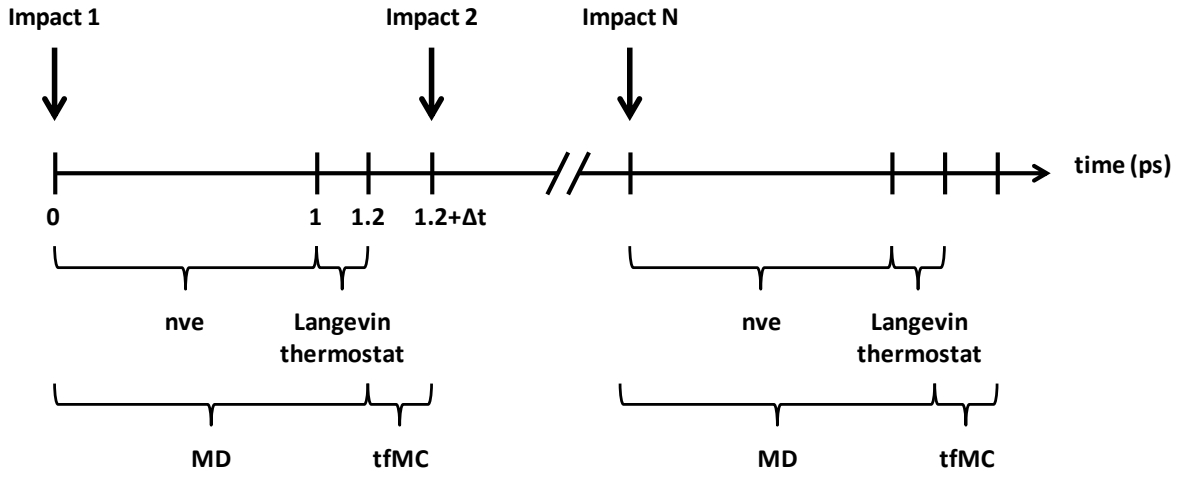

Figure 44: Sketch of the combined MD/MC simulation target.

The addition of a time-stamped force-bias Monte Carlo simulation then allows taking into account a longer time scale of thermal relaxation process after each impact. The value of Δ is chosen from 7% of the nearest neighbor distance i.e. for our model $\Delta = 0.20566$. The integration time step of tfMC simulations is calculated from the Equation III-38 and so is equal to 38.43 fs.

5. Results

The following results are presented according to studies such as titanium sputtering by argon ions bombardments, reactive sputtering of titanium and hot titanium target sputtering. The simulations are thus performed with two simulation box configurations, as previously presented, including or not a gas phase.
In these studies, we are interested on the determination of sputtering yields and retention rates considering the three incoming ions kinetic energies of 200, 300 and 400 eV.

5.1. Modelling of Ti sputtering by Ar^+

A simple model of titanium sputtering by argon ions is studied using molecular dynamics and by considering a longer thermal relaxation time scale by combining MD with MC simulations using time-stamped force bias Monte Carlo.

5.1.1. MD simulations

The molecular dynamics simulations of titanium sputtering by argon ions were performed for a total number of incoming ions of 105.

- Target temperature

In order to verify the treatment of the thermal relaxation of the target according to the simulations schemes presented previously, the figures below describe the evolution of the temperature in the region of thermostated atoms of the target during the first five impacts for the three considered energies.

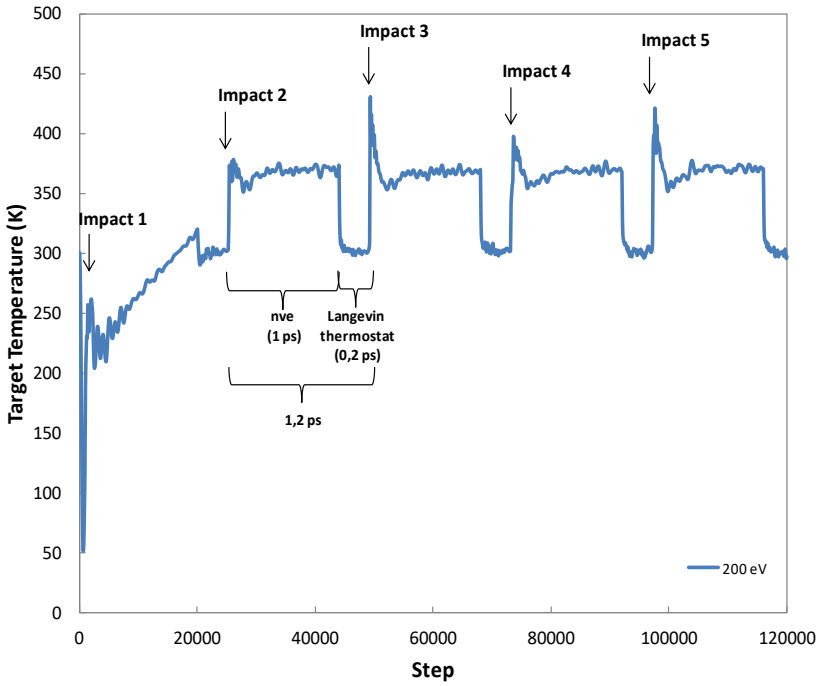

Figure 45: Evolution of the temperature in the thermostated region during 5 impacts of Ar^+ at 200 eV.

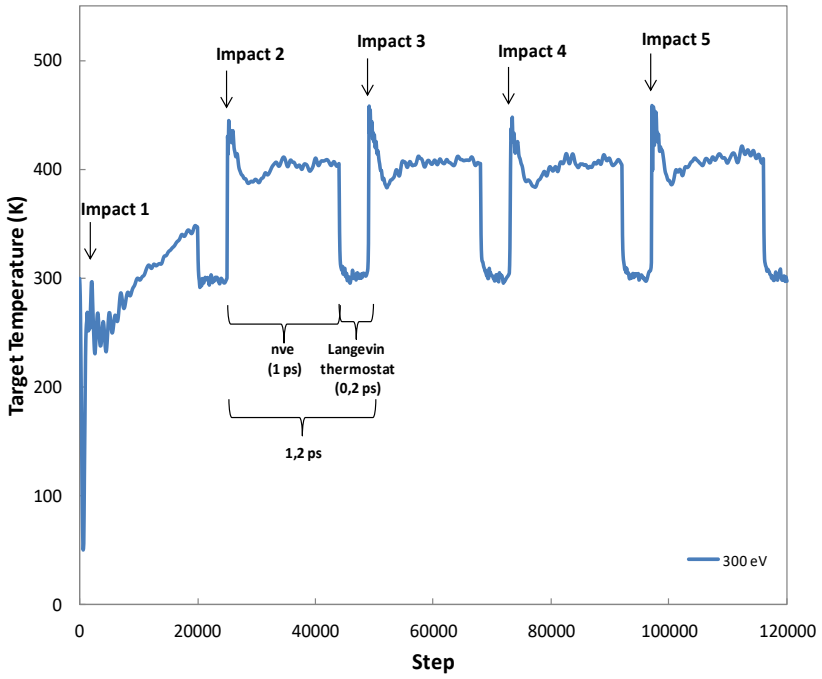

Figure 46: Evolution of the temperature in the thermostated region during 5 impacts of Ar^+ at 300 eV.

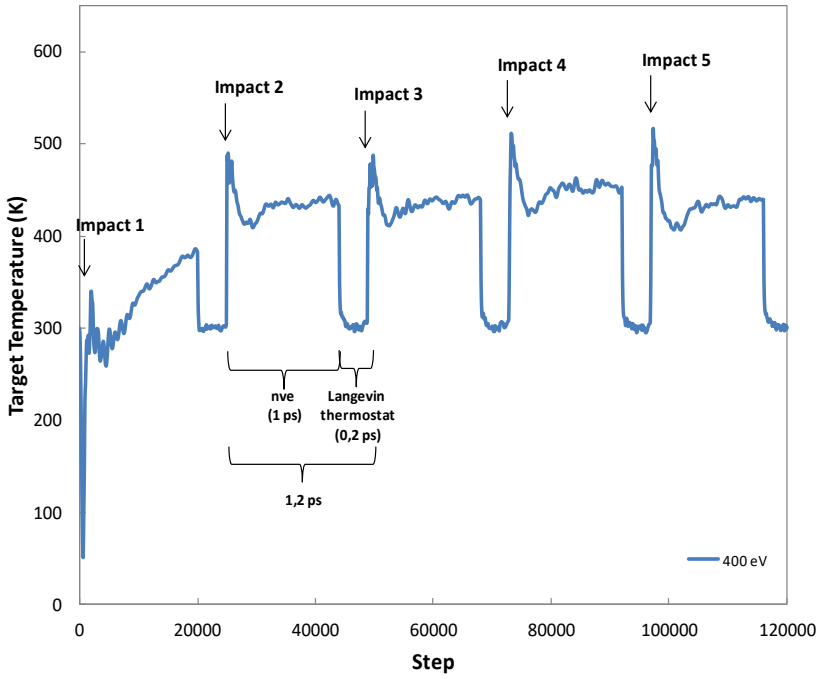

Figure 47: Evolution of the temperature in the thermostated region during 5 impacts of Ar^+ at 400 eV.

Every 24000 iterations i.e. every 1.2 ps an ion is injected and impacts the target. Then, the temperature increases due to ions and the Langevin thermostat acts as a heat bath to regularize the temperature of the target at the reference one of 300 K. The MD simulation scheme described in the **Figure 43** is therefore respected.

By comparing the three figures, the temperature of the thermostated atoms region increase with the kinetic ions energies. As mentioned previously, heat is then produced from the transferred energy by the ions and thus depends on their velocities. The application of a thermostat, such as the Langevin thermostat, is therefore necessary to dissipate the accumulated heat from impacts in order to correctly describe the sputtering process.

- Sputtering yield

The sputtering yield is calculated by the ratio of the number of sputtered atoms from the target surface per the number of incident ions:

$$Y = \frac{N_{sputtered\ target\ atoms}}{N_{incident\ ions}} \quad \text{(III-40)}$$

The resulting values of MD are close to those obtained using TRIM [178], ACAT program from Yamamura and Tawara [124] and to experimental measurements from Laegreid and Wehner [179]. The **Table 3** summarizes these results while the **Figure 48** displays the sputtering yields at various energies as a function of the number of ions impacts. In the case of energies of 200 and 300 eV, convergences are obtained after 40 to 60 impacts. However for energy of 400 eV, the convergence is obtained after 80 to 100 impacts.

	200 eV	300 eV	400 eV
TRIM	0.33	0.45	0.55
Yamamura formula	0.21	0.31	0.40
Laegreid and Wehner	0.22	0.33	0.44

Table 3: Sputtering yields of the various energies obtained with TRIM (considering 1000 incident ions), Yamamura formula and from Laegreid and Wehner experiments.

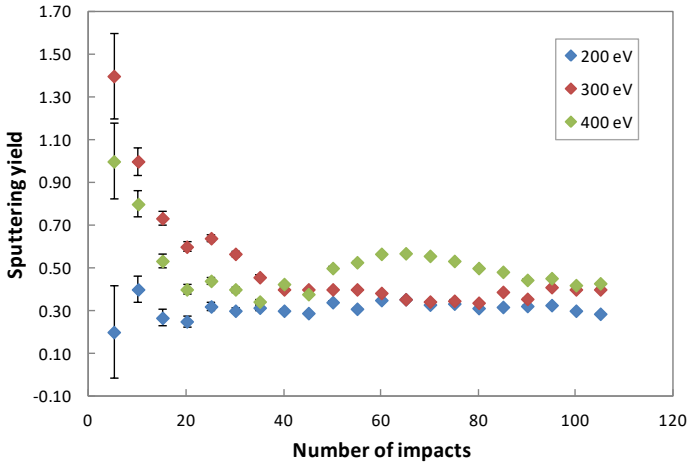

Figure 48: Sputtering yields obtained with MD simulations.

The sputtering yields will converge to values around 0.30 for 200 eV, 0.40 for 300 eV and 0.43 for 400 eV. This is close agreement with TRIM simulations.

- Retention rate

The retention rate is defined by the number of ions implanted in the target surface per the total number of incident ions:

$$\tau_{retention} = \frac{N_{implanted\ ions}}{N_{incident\ ions}} \quad \text{(III-41)}$$

The values of argon retention rate determined from MD are thus compared to those obtained using TRIM [178], presented in the **Table 4**.

	200 eV	300 eV	400 eV
TRIM	98%	98%	97%

Table 4: Argon retention rates of the various energies obtained with TRIM (considering 1000 incident ions).

The **Figure 49** below displays the argon retention rates at various energies according to the number of ions impacts. The retention rate is around 59% for 200 eV, 64% for 300 eV and 69% for 400 eV.

The MD calculated Ar retention rates are lower than TRIM simulations. Such a difference can originate from the different approaches implemented at the molecular scale between the two methods. Especially the many body nature of the potential will play a role.

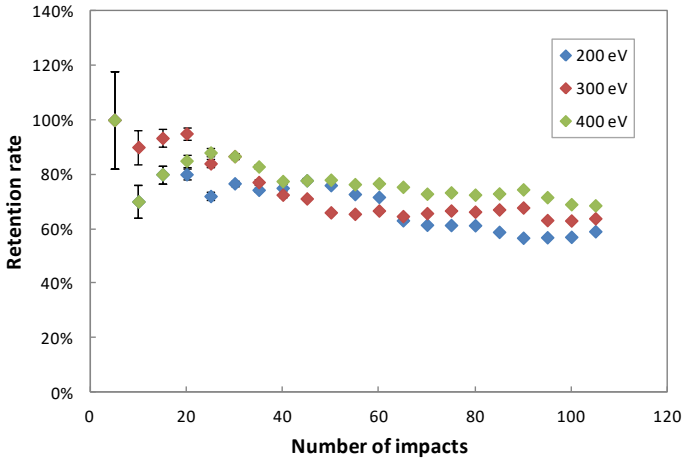

Figure 49: Retention rates obtained with MD simulations.

5.1.2. Combining MD/MC simulations

The molecular dynamics combined with time-stamped force-bias Monte Carlo simulations of titanium sputtering by argon ions were performed for a total number of incoming ions of 100.

- Target temperature

In the combined MD/MC simulations, during the first five impacts, the temperature of the target evolves as below:

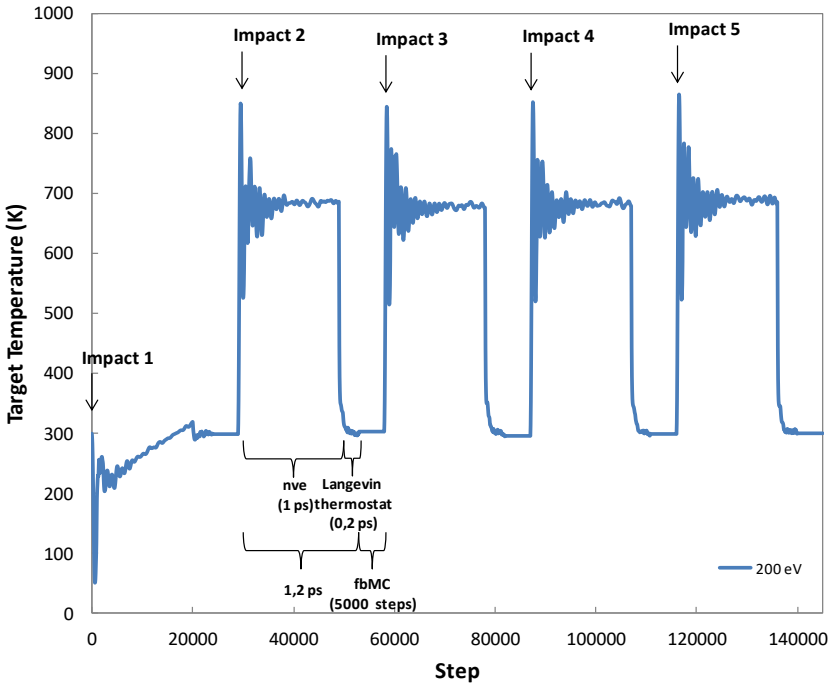

Figure 50: Evolution of the temperature in the thermostated region during 5 impacts of Ar^+ at 200 eV.

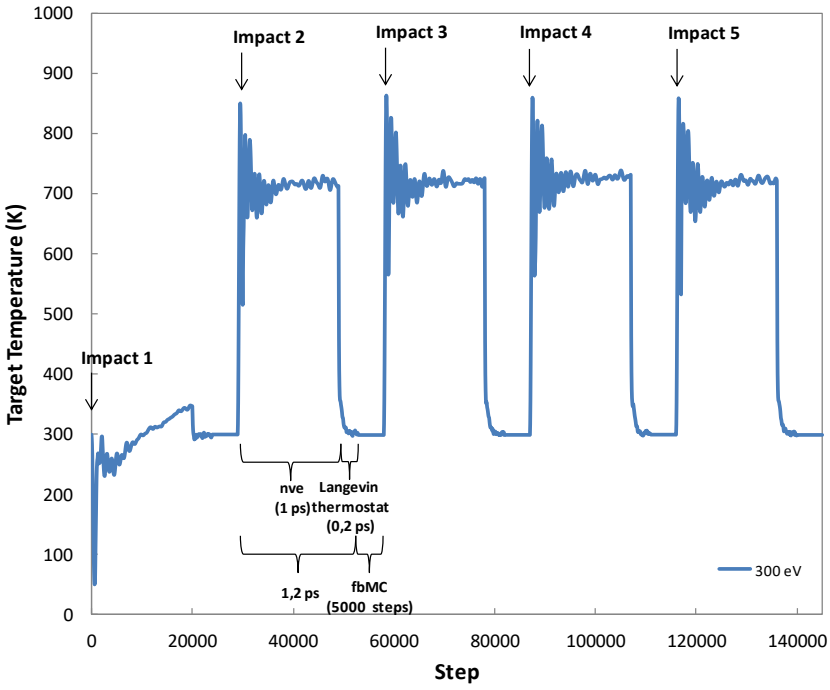

Figure 51: Evolution of the temperature in the thermostated region during 5 impacts of Ar^+ at 300 eV.

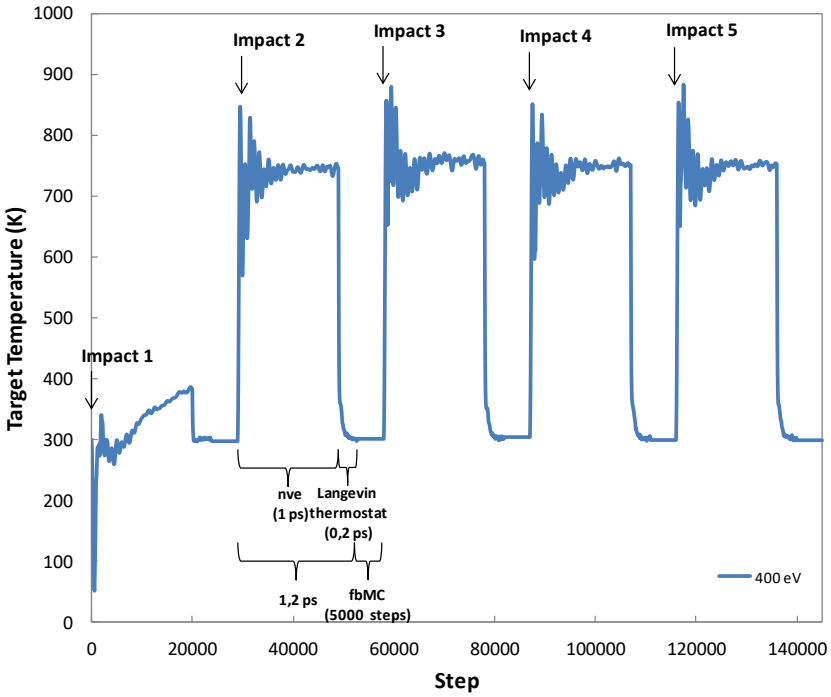

Figure 52: Evolution of the temperature in the thermostated region during 5 impacts of Ar^+ at 400 eV.

An ion is injected every 29000 iterations to impact the target. The Langevin thermostat is applied every 20000 iterations to dissipate accumulated energy from ions and set the temperature of the thermostated region at 300 K.

The temperatures after impact obtained by MD/tfMC are higher than those obtained by MD. However, the resulting yields are not affected by these different temperatures. It would also be interesting to study in more details the evolution of the target temperature in the MD/tfMC simulations.

According to the Equation III-38, the tfMC simulations allow to extend the thermal relaxation during 192 ps. Finally, in these simulations, using tfMC means a sputtering ion is injected every 193.2 ps instead of 1.45 ps. This allows to better account of the substrate relaxation upon Ar impacts.

- Target surface

The maximum displacement length Δ is chosen according to the condition that larger deformations of the target should not occur during the tfMC simulation [177].

Thus, in our models, the target structures obtained after the tfMC simulations are close to those of MD and the longer relaxation time scale can therefore be taken into account.

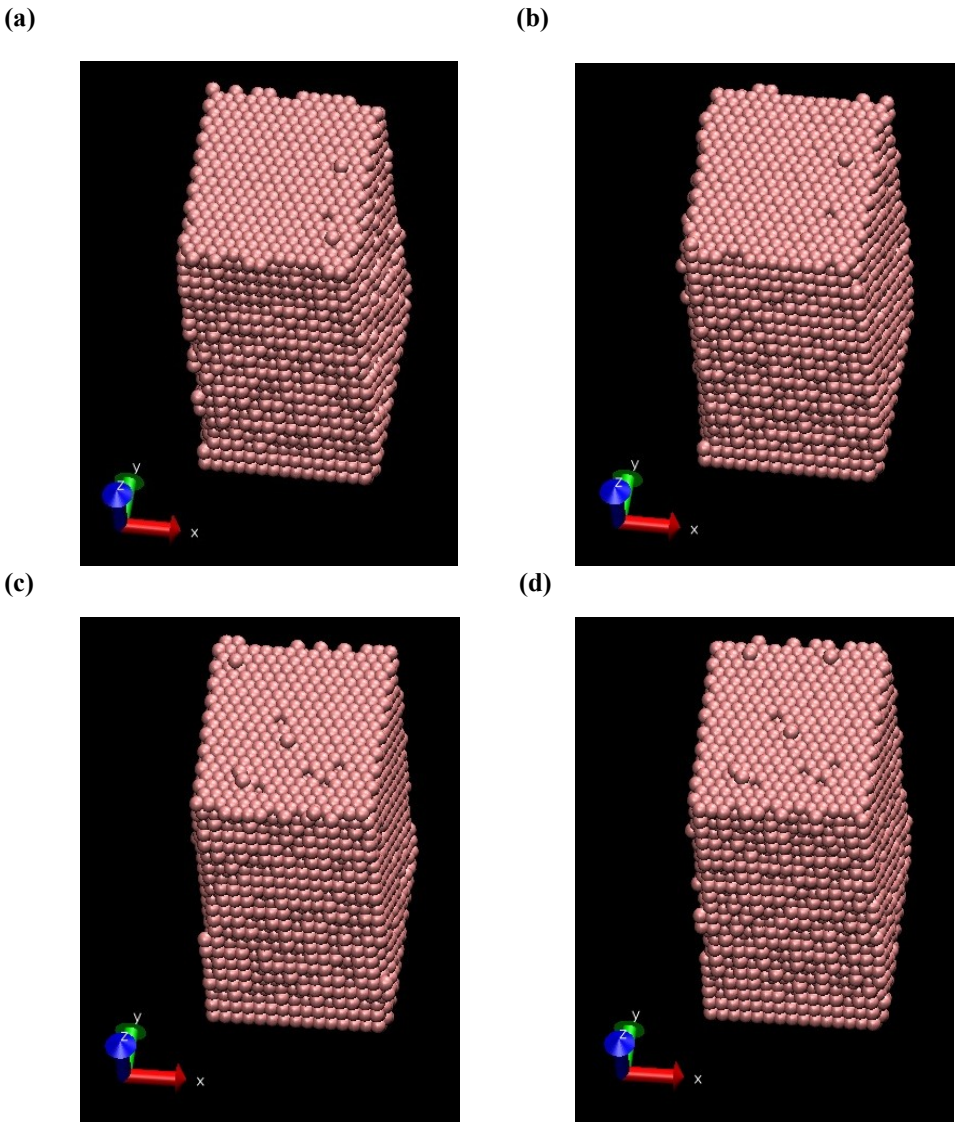

Figure 53: Surface of the target during sputtering by ions of 200 eV at 1.2 ps (a), 193.2 ps (b), 774 ps (c) and 966 ps (d).

- Sputtering yield

The sputtering yield is around 0.21 for 200 eV, 0.40 for 300 eV and 0.37 for 400 eV. In all cases, convergences are obtained after 40 to 60 impacts.

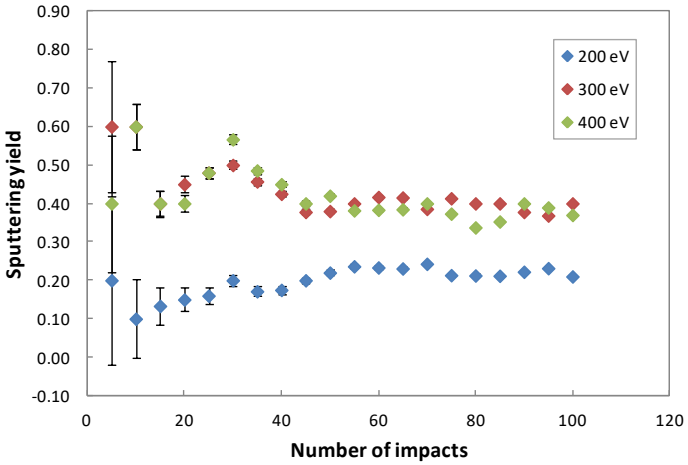

Figure 54: Sputtering yields of MD/tfMC simulations.

Typically, the sputtering should increase with the value of the incident ions kinetic energies. Concerning the comparison of the sputtering yields obtained with those of the others methods, the **Figure 55** show that values obtained by MD and by combining MD with tfMC simulations are between those obtained by TRIM and Yamamura formula, as well as the experimental results from Laegreid and Wehner.

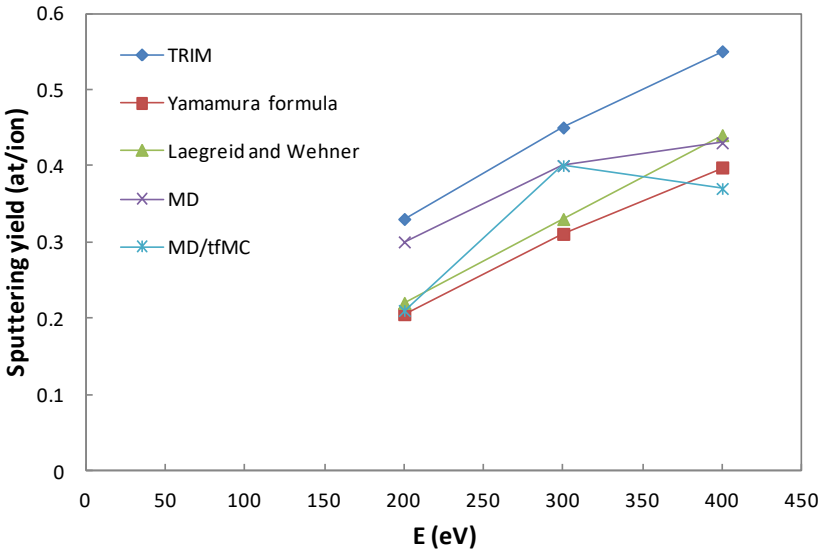

Figure 55: Ti sputtering yields as a function of Ar^+ energies.

Sputtering yields from MD are close to TRIM except for 400 eV, which is closer to Yamamura formula and sputtering yields from MD/tfMC are close to Yamamura formula, except for 300 eV, which is closer to TRIM.
Nevertheless, MD and MD/tfMC sputtering yields lie between TRIM and Yamamura formula. The improvement of MD/tfMC allows the results to move towards experimental results of Laegreid and Wehner.

- Retention rate

The different retention rates obtained by combining MD with tfMC are 66% for 200 eV, 72% for 300 eV and 68% for 400 eV.

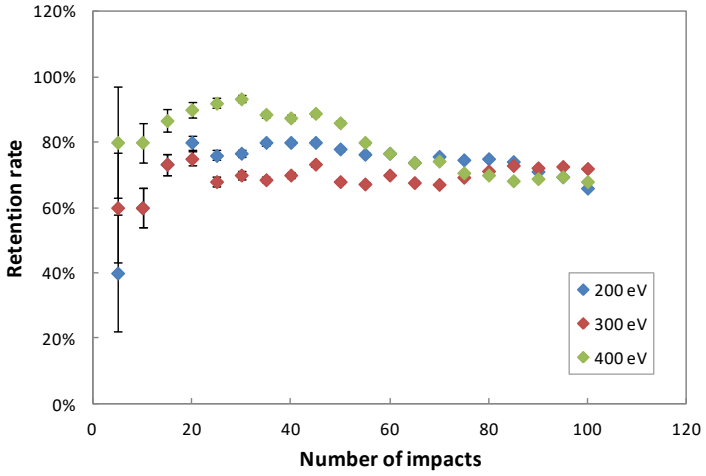

Figure 56: Retention rates of MD/tfMC simulations.

The **Figure 57** below compares the different argon retention rates resulting from TRIM, MD and by combining MD with tfMC simulations.
The results obtained by MD and by combining with tfMC simulations are much lower than those calculated by TRIM. The retention rate determined with TRIM simulations is almost constant according to the three kinetic energies. For 200 and 300 eV, the retention rates determined by combining MD/tfMC are higher than those from MD. For 400 eV the rates calculated for MD and by combining with tfMC are close. The retention rate from MD increases linearly with the kinetic energies. Therefore, in order to obtain results closer to TRIM simulations, higher energies must be applied [112]. Convergence to TRIM at highest energies has already been observed on Pt and Cu MD sputtering [112].

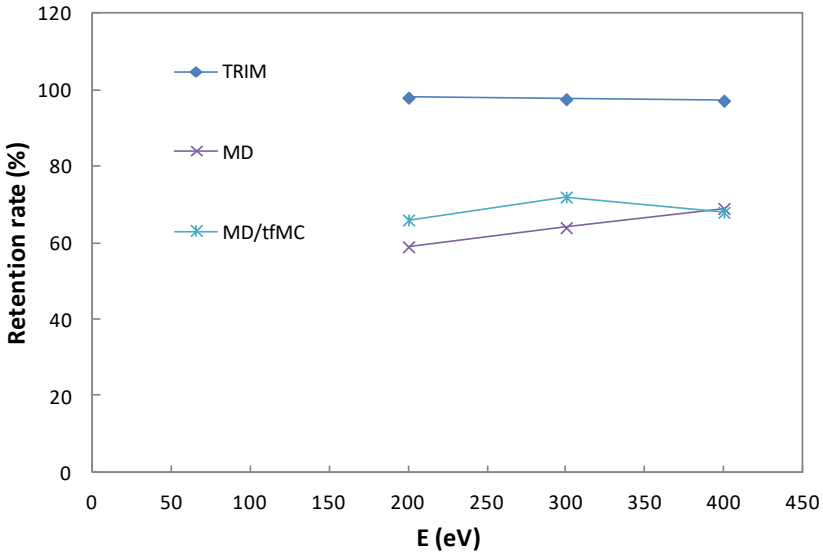

Figure 57: Ar^+ retention rate as a function of Ar^+ energies.

5.1.3. Conclusion

The maximum displacement length chosen for the tfMC simulations allows the determination of a time scale used to extend the thermal relaxation of the target after impact [177]. Moreover, the structures obtained with tfMC simulations are consistent with MD.

Sputtering yields and retention rates show some differences between MD and by combining MD with tfMC simulations. Nevertheless, the resulting sputtering yields of MD and MD/tfMC simulations for the three considered kinetic energies are in good agreement with results obtained by TRIM simulations, calculations from Yamamura formula and experiments by Laegreid and Wehner. The retention rates obtained are however lower than values from TRIM. TRIM is known to be suitable for simulation according to high energies [112]. It will be therefore interesting to study higher energies such as 1000 eV.

5.2. Molecular dynamics simulation of Ti sputtering by Ar^+ in reactive atmosphere

In this study, sputtering yields and retention rates are compared for three cases of simulation such as reactive sputtering in a gas mixture of 50% Ar – 50% O and according to two extreme

cases including non reactive sputtering in argon gas and reactive sputtering in a gas phase composed by oxygen.

Considering a gas phase comprising argon atoms make it possible to approach real sputtering conditions in which the ionisation rate is low. Indeed, the incident Ar^+ passing through the gas phase to impact the target surface may lose energy by collisions with Ar.

Due to the gas phase, the region where the Ar^+ are created is far from the target surface. Hence, the distance between this region and the surface of the target must be taken into account to respect the time development of the simulations. Thus, at the first ion injection, a number of iterations equivalent to the time that an ion takes to pass through the gas phase is applied.

For all cases, the total number of ions impacts considered in simulations is fixed to 100.

5.2.1. Ti sputtering by Ar^+ in Ar

- Sputtering yield

The **Figure 58** and the **Figure 59** display the sputtering yields determined by MD and by combining MD with tfMC for the three considered energies. The convergences are obtained after 40 and 60 impacts for most of the simulations.

The different results will then be compared to the sputtering yields presented in the previous study.

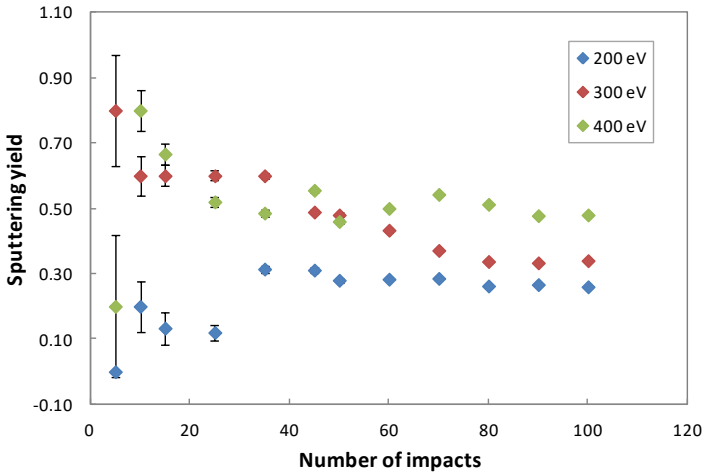

Figure 58: Sputtering yields of MD simulations with a gas phase of Ar.

The sputtering yields obtained by MD are 0.27 for 200 eV, 0.24 for 300 eV and 0.48 for 400 eV. These values are lower than those obtained in the previous study by MD except for the kinetic energy of 400 eV.

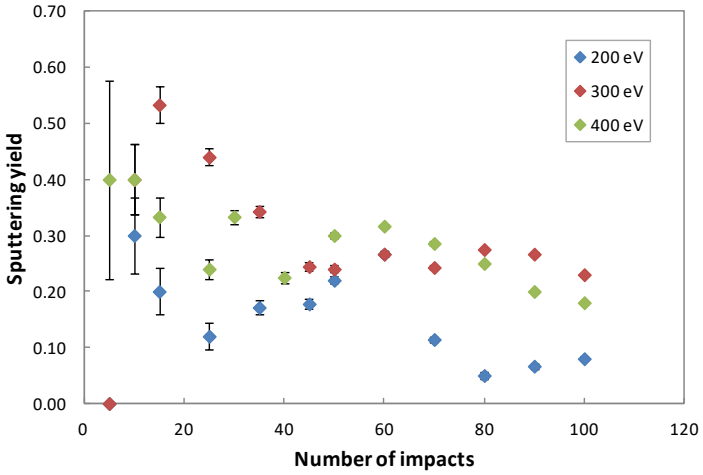

Figure 59: Sputtering yields of MD/tfMC simulations with a gas phase of Ar.

By combining with tfMC, the sputtering yields obtained are 0.08 for 200 eV at 100 impacts, 0.24 for 300 eV and 0.18 for 400 eV at 100 impacts. The low sputtering yield for 200 and 400 eV could be explained by the fall of several sputtered atoms on the target. Thus, this can distort the results.

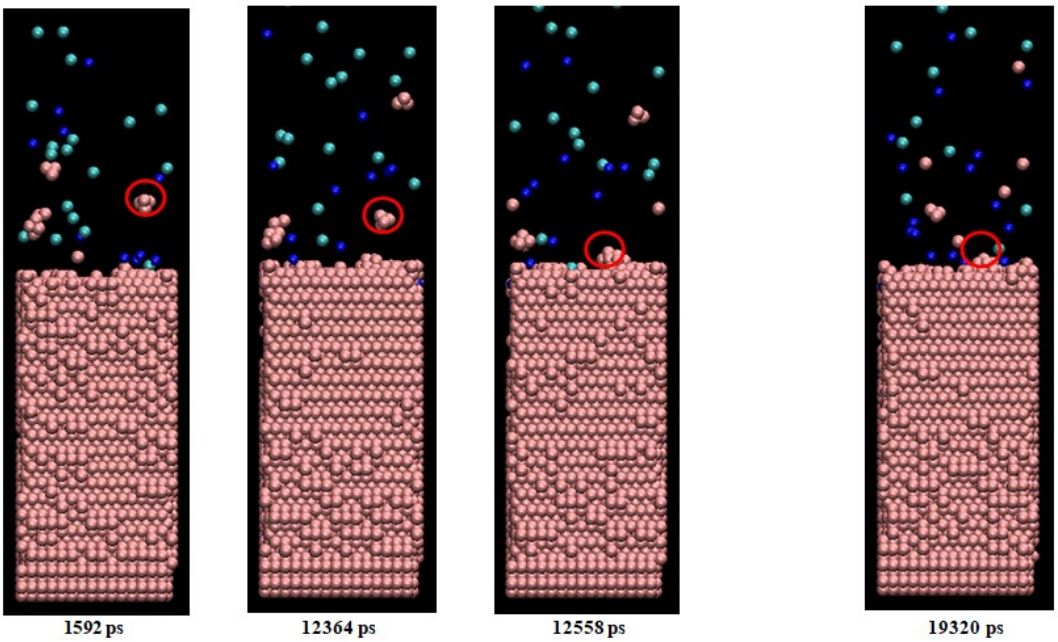

Figure 60: Example of falling sputtered Ti atoms after impacts of ions with a kinetic energy of 200 eV.

However, convergences are not obtained for energies of 200 and 400 eV. Therefore, these calculations require taking into account more ions impacts. Concerning the simulations for 300 eV, the sputtering yield obtained in this study is very low compared to the previous one. The results obtained for kinetic energies of 200 and 300 eV with a gas phase show that the sputtering yield are lower than those without a gas phase, and especially in combining MD/tfMC simulations. This can be explained by considering that the final kinetic energy of the ions at the Ti surface is lowered due to the collision with Ar atoms along the path to the substrate.

Finally, as presented in the following **Figure 61**, by considering a gas phase in MD simulations, the sputtering yields are lower than those calculated with TRIM and higher than those calculated with Yamamura formula. The sputtering yield obtained for 300 eV by combining MD with tfMC is the lowest.

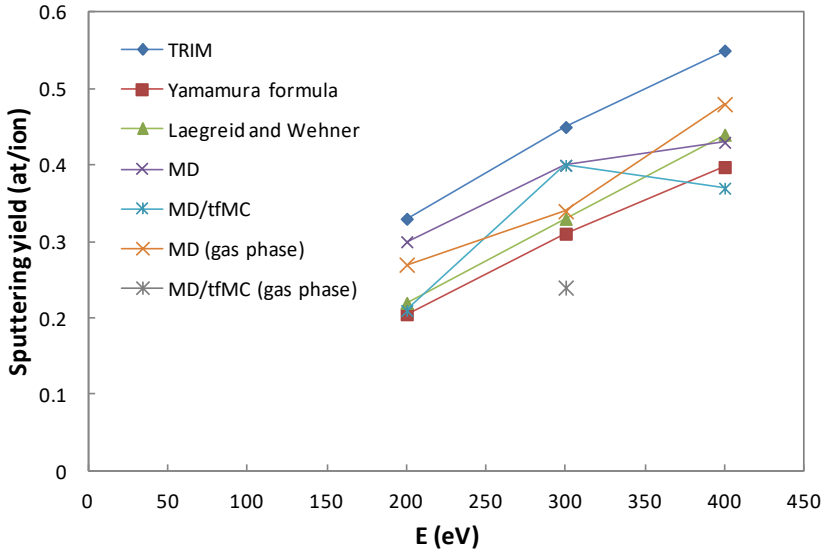

Figure 61: Ti sputtering yields as a function of Ar^+ energies.

- Retention rate

The argon retention rates obtained by MD and by combining MD with tfMC are presented in the **Figure 62** and the **Figure 63**. Normally, the rates obtained should be similar to the results of the previous study.

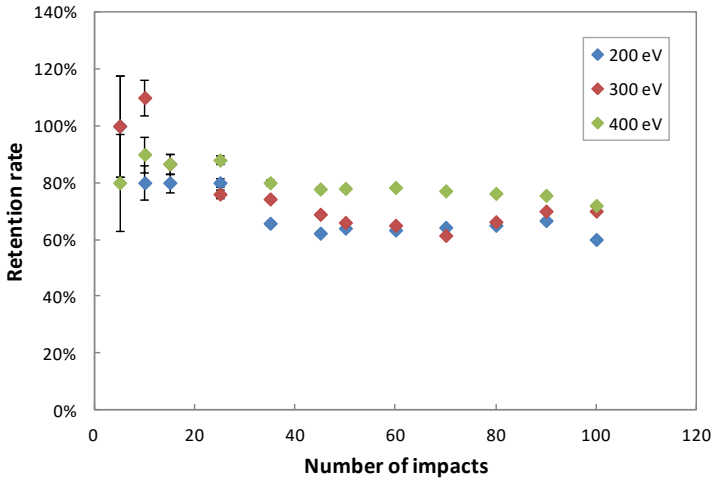

Figure 62: Retention rates of MD simulations with a gas phase of Ar.

The retention rate from MD simulations with a gas phase of argon is 60% for 200 eV, 70% for 300 eV and 72% for 400 eV.

Moreover, by combining MD with tfMC simulations, with a gas phase of argon, the retention rate is 57% for 200 eV, 68% for 300 eV and 71% for 400 eV.

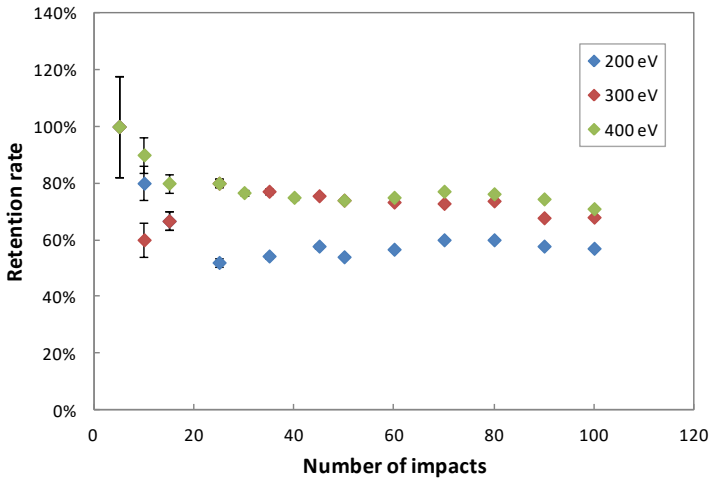

Figure 63: Retention rates of MD/tfMC simulations with a gas phase of Ar.

The **Figure 64** then compares these results with the rates calculated previously and with TRIM.

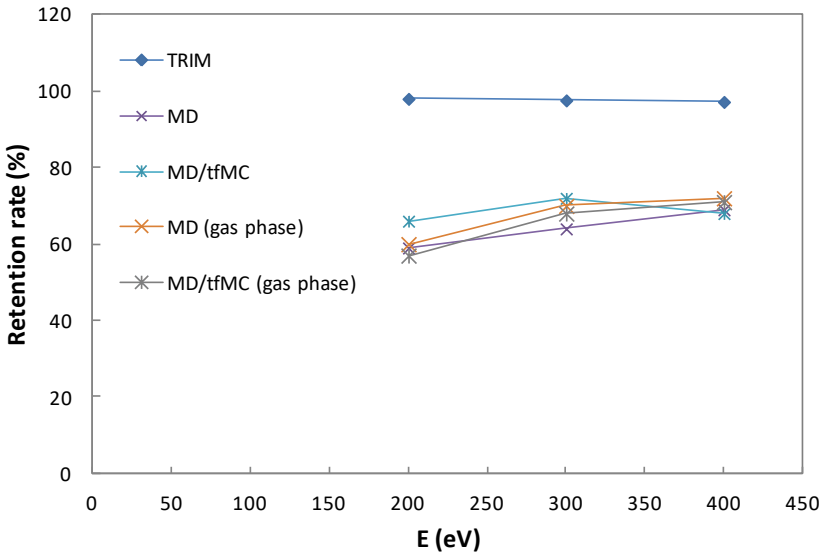

Figure 64: Ar^+ retention rate as a function of Ar^+ energies.

As expected, the argon retention rates obtained here are closer to those of the previous study and therefore lower than the retention rates calculated with TRIM.

5.2.2. Ti sputtering by Ar^+ in Ar-O

- Sputtering yield

The following figures display the sputtering yields resulting for the three considered energies. The convergences are obtained after 50 impacts for energies of 300 and 400 eV in MD simulations and after 40 to 60 impacts for all the combined MD/tfMC simulations.

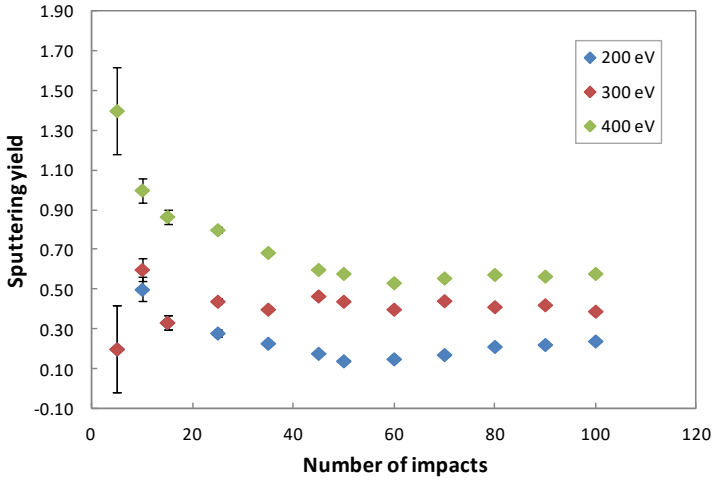

Figure 65: Sputtering yields of MD simulations with a gas phase of a 50% Ar - 50% O mixture.

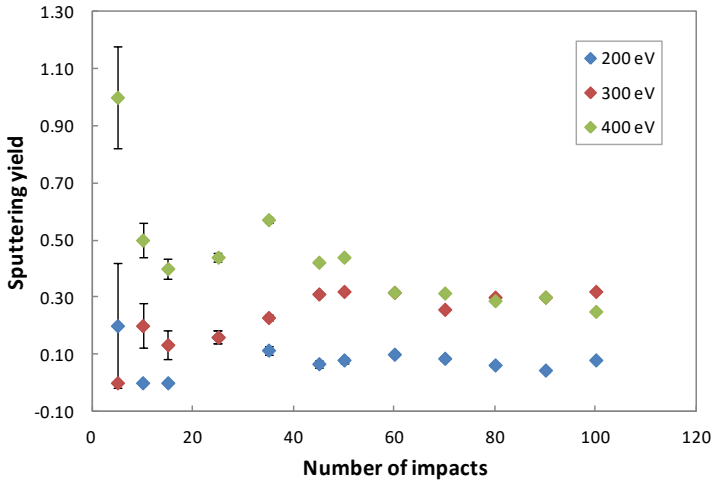

Figure 66: Sputtering yields of MD/tfMC simulations with a gas phase of a 50% Ar - 50% O mixture.

The sputtering yields obtained by MD are 0.39 and 0.58 for 300 and 400 eV. As the convergence is not obtained for 200 eV, the sputtering yield should be higher than 0.24. By combining MD with tfMC, the sputtering yields are 0.08 for 200 eV, 0.32 for 300 eV and 0.25 for 400 eV. In reactive sputtering, when the target is poisoned by reactive compounds, it is difficult to sputter target atoms. The yields should therefore be lower than those obtained in the case of non-reactive sputtering. However, the sputtering yields resulting using MD are high, mostly for 400 eV.

High sputtering yields were obtained by Kubart and co-workers in case of TiO_x sputtering in Ar due to lower Ti oxides (or suboxides) at targets surface. Indeed, it was observed that the hysteresis disappeared with the increase of oxides in the target [180, 181]. Therefore, these MD results can be explained by the formation of numerous oxides described as suboxides leading to sputtering yield close to the corresponding metal.

a) b)

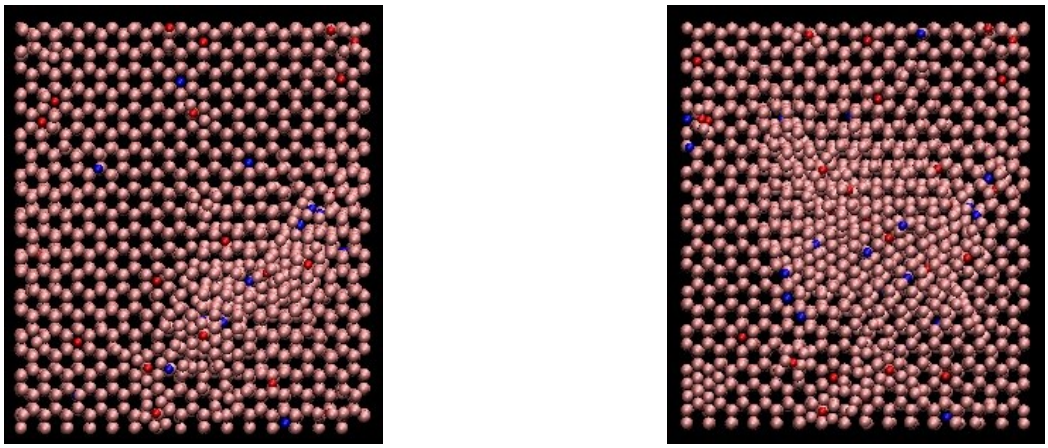

c) d)

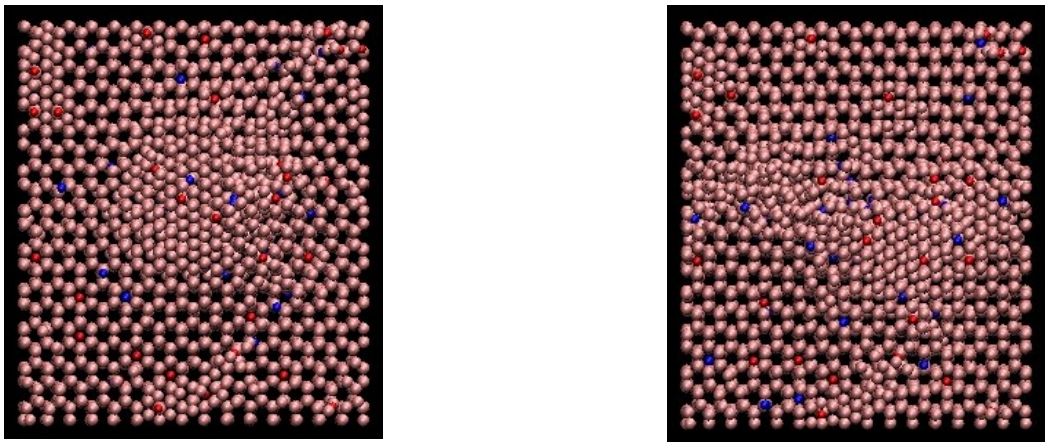

Figure 67: Target surface at 30 (a), 50 (b), 70 (c) and 100 (d) ions impacts of 400 eV. The color spheres of pink, red and blue represent Ti, O and Ar^+, respectively.

In the **Figure 67**, there are a few oxygen atoms in the target surface. Therefore a poisoning target cannot be considered. The low sputtering yields obtained should then be due to the gas which causes a reduction of the energy of the ions.

- Retention rate

The retention rates obtained for the three considered energies are given below for MD and by combining MD with tfMC simulations.

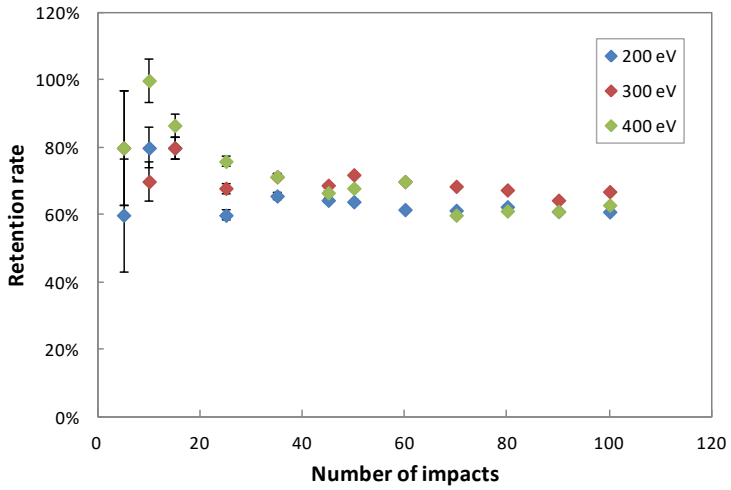

Figure 68: Retention rate of MD simulations with a gas phase of a 50% Ar - 50% O mixture.

The argon retention rate from MD simulations is 61% for 200 eV, 67% for 300 eV and 63% for 400 eV. These last two results are lower than those obtained in non-reactive sputtering.

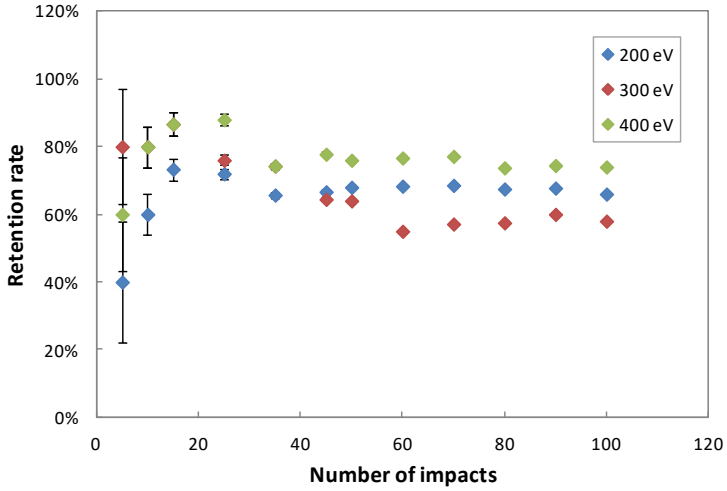

Figure 69: Retention rate of MD/tfMC simulations with a gas phase of a 50% Ar - 50% O mixture.

According to MD/tfMC simulations, the retention rates are 66% for 200 eV, 58% and 74 % for 300 and 400 eV respectively.

5.2.3. Ti sputtering by Ar^+ in O

- Sputtering yield

In order to compare the calculated yields in the case of sputtering in a reactive gas mixture of Ar-O, we consider Ti reactive sputtering in a gas phase entirely composed by O.

The convergences are obtained after 40 to 60 for all the simulations except for 400 eV by combining MD with tfMC where the convergence is not obtained.

The sputtering yields obtained in this case are 0.21 for 200 eV, 0.37 for 300 eV and 0.63 for 400 eV using MD. Once again, these yields are high in the case of reactive sputtering and reactive compounds are more formed with ions kinetic energy of 400 eV.

Concerning MD/tfMC simulations, the sputtering yields are 0.18 for 200 eV, 0.27 for 300 eV and 0.32 for 400 eV at 100 impacts. There is a major difference between MD and MD/tfMC for the 400 eV case, that is not fully understood at this step.

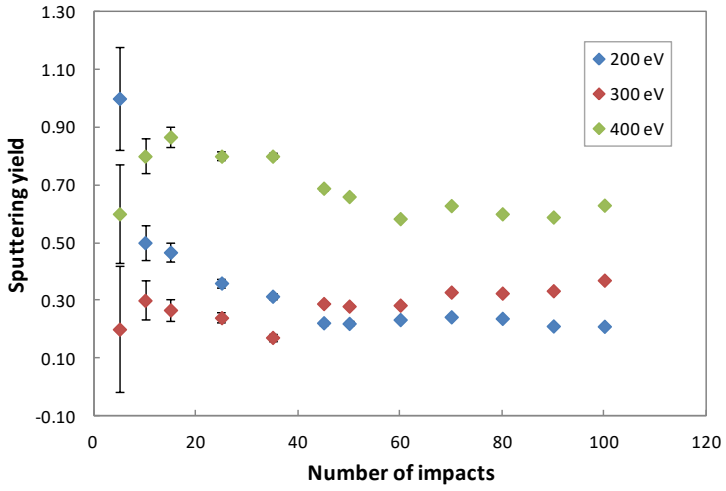

Figure 70: Sputtering yields of MD simulations with a gas phase of O.

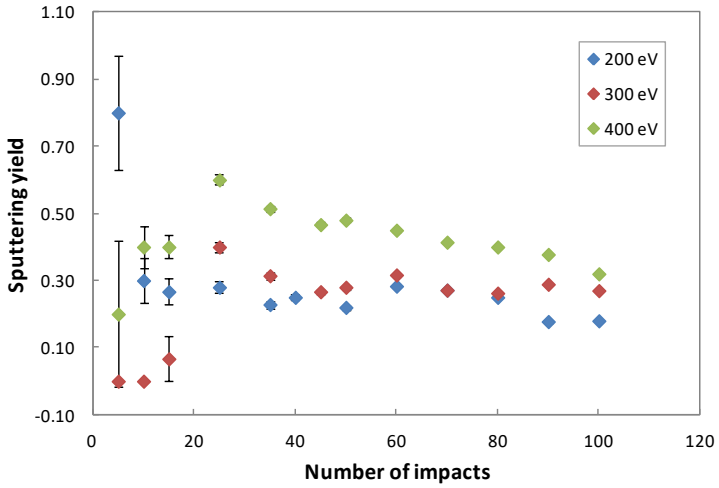

Figure 71: Sputtering yields of MD/tfMC simulations with a gas phase of O.

- Retention rate

The retention rates obtained in this case are 58% for 200 eV, 78% for 300 eV and 69% for 400 eV by MD, 40% for 200 eV, 56% and 66% for 300 and 400 eV by combining MD with tfMC simulations. But there are convergence problems for MD/tfMC at 200 and 300 eV.

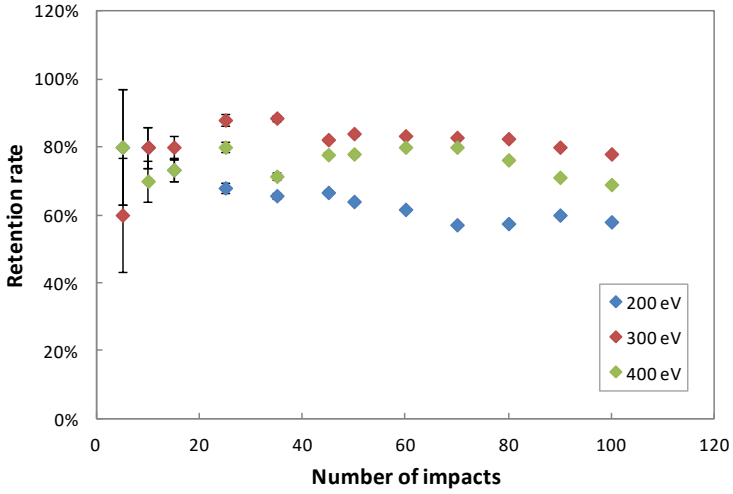

Figure 72: Retention rates of MD simulations with a gas phase of O.

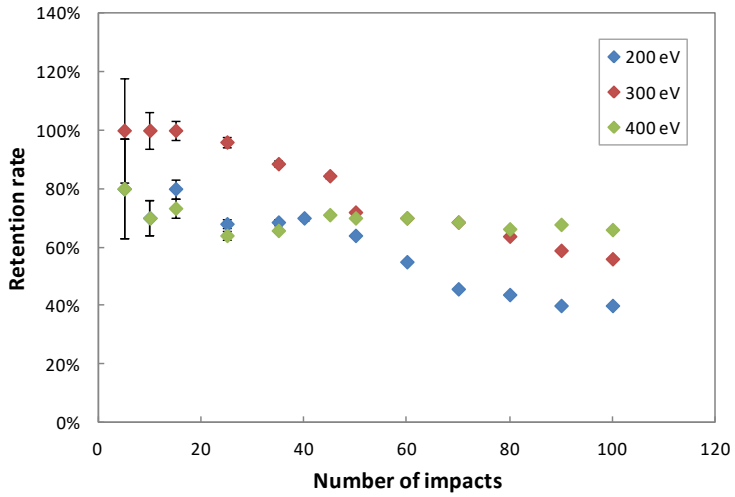

Figure 73: Retention rates of MD simulations with a gas phase of O.

5.2.4. Conclusion

In these three cases, the simulation box includes a gas phase allowing taking into account the reactive gas (here composed of oxygen) for the reactive sputtering of a pure titanium target and also being close to experiments by adding argon atoms.

Typically, the sputtering yields obtained in reactive sputtering are lower than those obtained in nonreactive sputtering due to poisoned target. By considering a gas phase of oxygen and an argon-oxygen mixture, the sputtering yields calculated by combining MD with tfMC thus are low. However, our reactive sputtering simulations based on MD showed sputtering yields slightly lower than those calculated in nonreactive sputtering for kinetic energies of 200 and 300 eV and very high for 400 eV.

The retention rates calculated in reactive sputtering is close to those obtained in nonreactive sputtering.

Finally, the results obtained with the two reactive gas phases of Ar-O (100-100) and of O (200) are similar. It could be thus interesting to consider more atoms in the gas.

5.3. Hot target sputtering simulations

In experiments, the use of a cooling system to the target allows avoiding target melting due to the heat transferred by the electric power. The hot target sputtering process consists on

reducing the cooling of the target in order to operate at elevated temperature. Thus, the increase of deposition rate has been observed by operating with a target temperature close to the melting point of the target material [31].

In this study, the target temperature is applied to 1000 and 2000 K in order to mimic hot targets. The simulations take into account only 50 impacts.

5.3.1. Ti sputtering by Ar^+

- Sputtering yield

The figures below display the sputtering yields calculated for MD and by combining MD with tfMC simulations. Convergences are obtained after 20 to 40 impacts for most simulations.

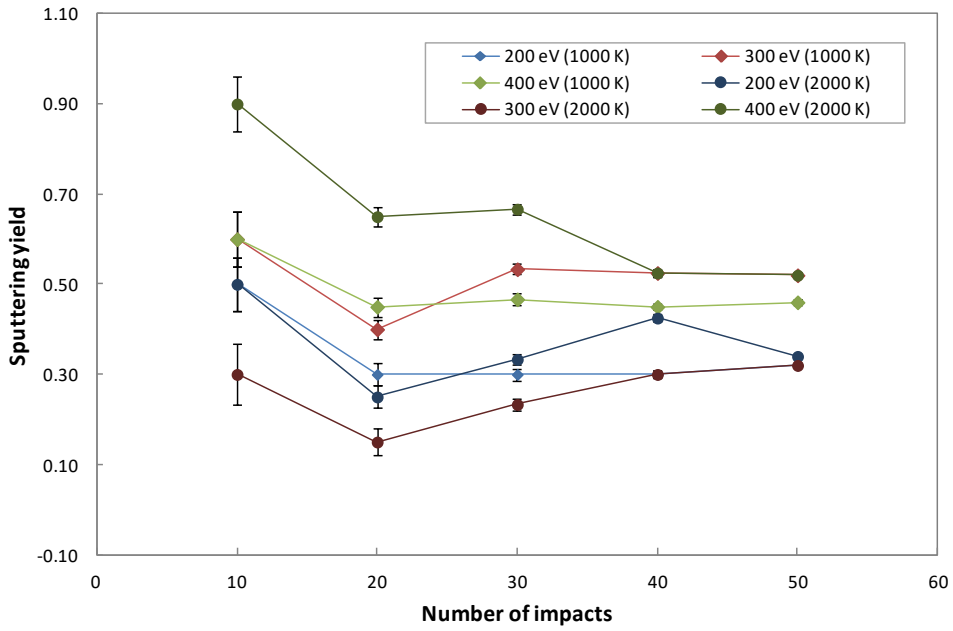

Figure 74: Sputtering yields of MD simulations for target temperatures of 1000 and 2000 K.

The sputtering yield calculated for MD simulations are 0.32 for 200 eV, 0.52 for 300 eV and 0.46 for 400 eV with a target temperature of 1000 K. The yields obtained at 50 impacts with a target temperature of 200 eV are 0.34 for 200 eV, 0.32 for 300 eV and 0.52 for 400 eV. These simulations require taking into account more impacts in order to obtain convergences for a target temperature of 2000 K.

Moreover, by combining MD with tfMC simulations, the sputtering yields are 0.18 for 200 eV at 50 impacts, 0.44 for 300 eV and 0.56 for 400 eV with a target temperature of 1000 K, 0.24 for 200 eV, 0.32 for 300 eV at 50 impacts and 0.48 for 400 eV with a target temperature of 2000 K.

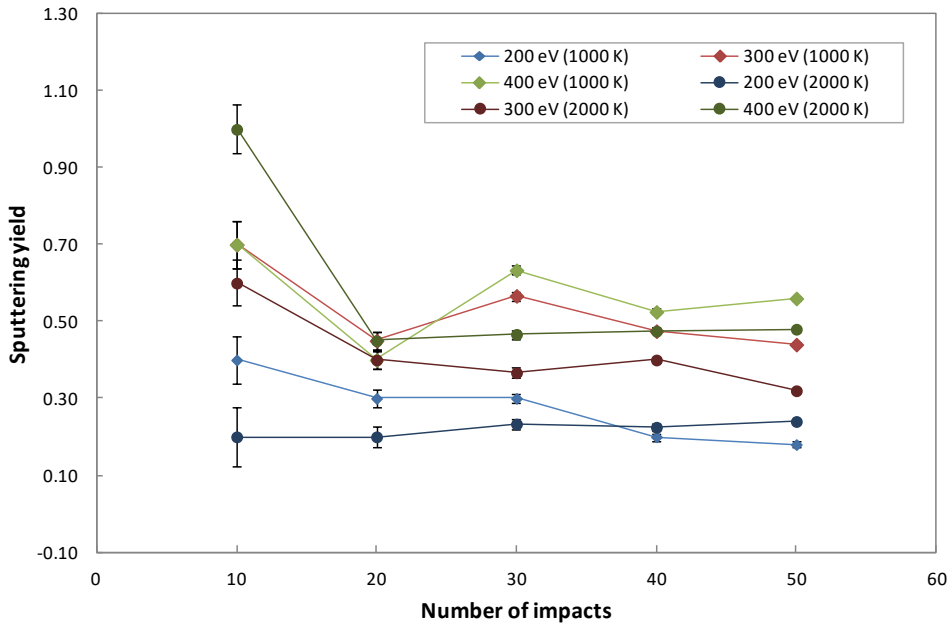

Figure 75: Sputtering yields of MD/tfMC simulations for target temperatures of 1000 and 2000 K.

The sputtering yields resulting with an elevated target temperature thus are higher than those obtained at 300 K.

- Retention rate

The retention rates using MD are 66% for 200 and 300 eV, 86% for 400 eV with a target temperature of 1000 K, 76% for 200 and 300 eV, 82% for 400 eV with a target temperature of 2000 K and by combining with tfMC, the rates are 60% for 200 eV, 76% for 300 eV and 82% for 400 eV at 1000 K, 64% for 200 eV, 78% for 300 eV and 72% for 400 eV at 2000 K.
Thus, with an elevated target temperature and by increasing the ion kinetic energy, more argon ions are implanted in the target surface.

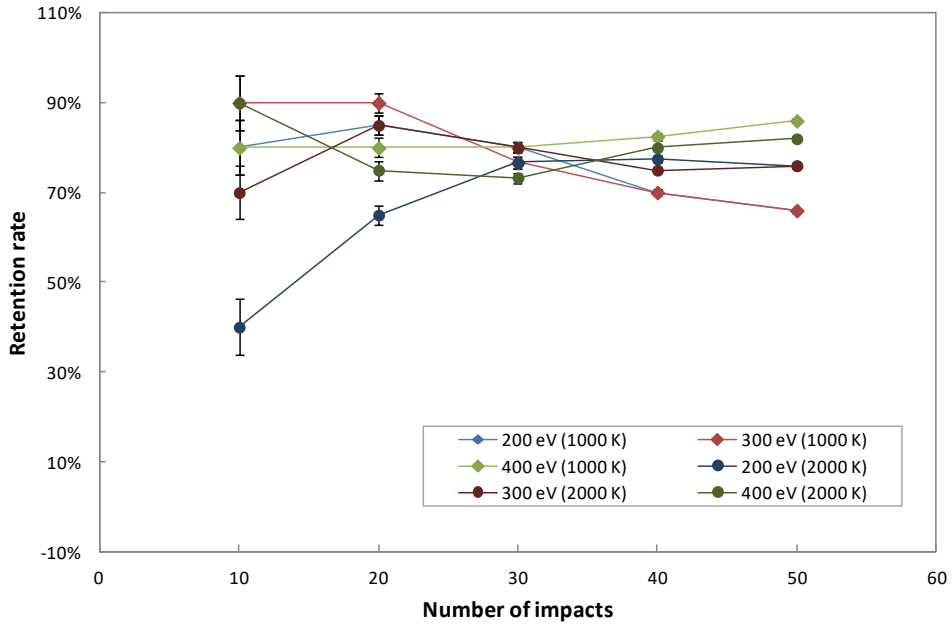

Figure 76: Retention rates of MD simulations for target temperatures of 1000 and 2000 K.

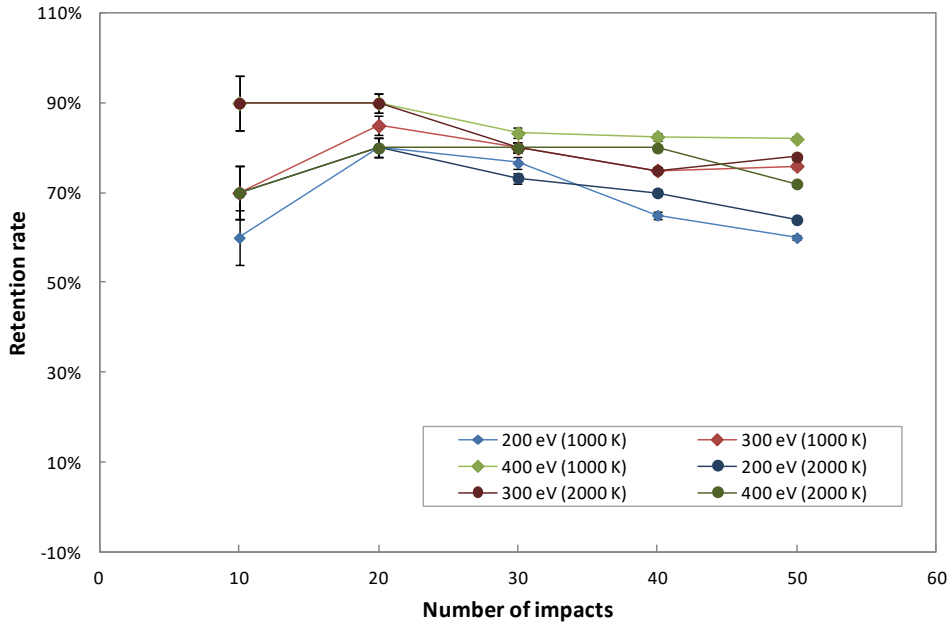

Figure 77: Retention rates of MD/tfMC simulations for target temperatures of 1000 and 2000 K.

5.3.2. Ti sputtering by Ar^+ in Ar, Ar-O and O

- Sputtering yield

The following figures present sputtering yields obtained with MD simulations according to the three considered gas phases.

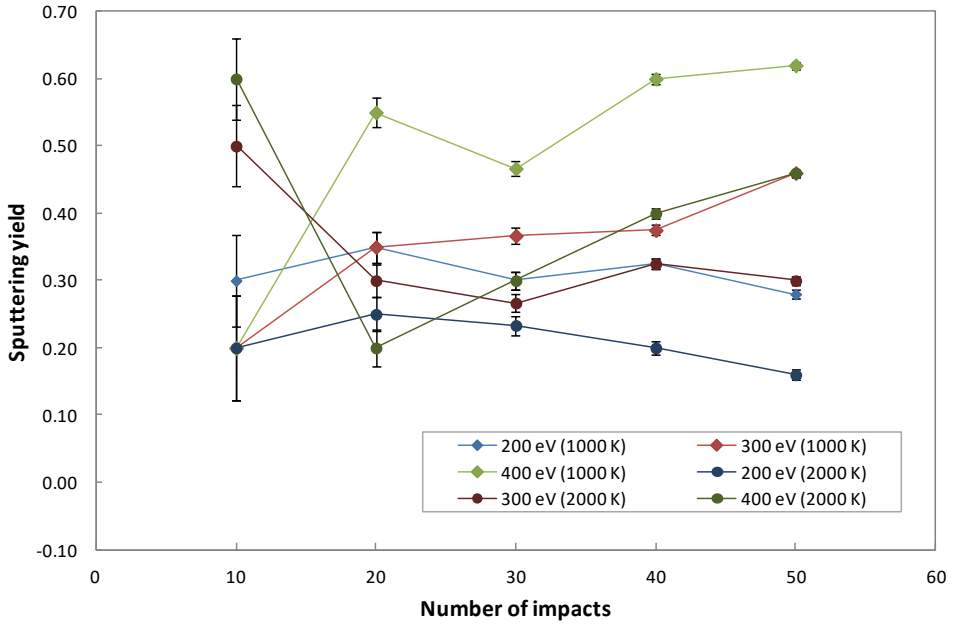

Figure 78: Sputtering yields in Ar gas for target temperatures of 1000 and 2000 K.

Convergences are not really obtained in most of these simulations. Therefore, at 50 impacts, the calculated sputtering yields are by including Ar gas 0.28 for 200 eV, 0.46 for 300 eV and 0.62 for 400 eV with a target temperature of 1000 K, and 0.16 for 200 eV, 0.30 for 300 eV and 0.46 for 400 eV with a target temperature of 2000 K. Then, in the case of Ar-O gas mixture, the sputtering yields are 0.12 for 200 eV, 0.26 and 0.34 for 300 and 400 eV at1000 K, 0.14 for 200 eV, 0.48 and 0.34 for 300 and 400 eV at 2000 K. By considering a gas phase of O, the yields are 0.12 for 200 eV, 0.30 for 300 eV and 0.64 for 400 eV at, 0.08 for 200 eV, 0.32 for 300 eV and 0.3 for 400 eV at 2000 K.

The sputtering yields obtained after 50 impacts in reactive sputtering are in most cases lower than those obtained in nonreactive sputtering. However, more ions impact should be taken into account.

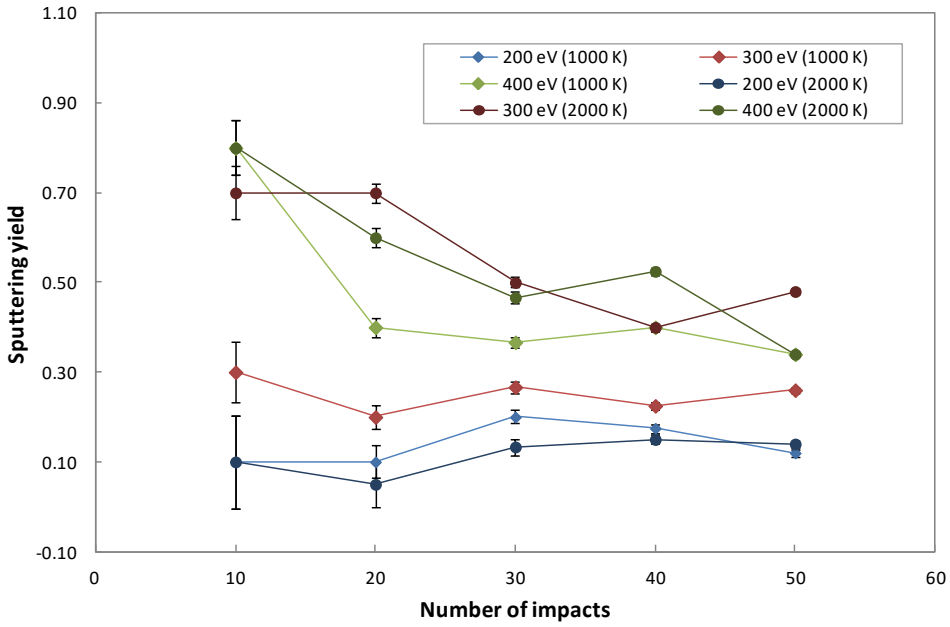

Figure 79: Sputtering yields in Ar-O gas for target temperatures of 1000 and 2000 K.

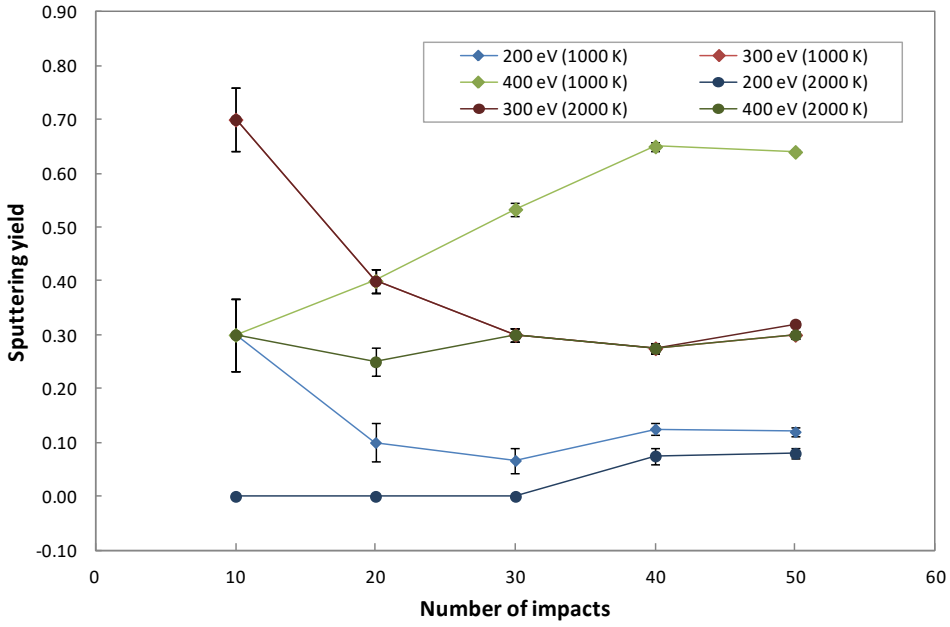

Figure 80: Sputtering yields in O gas for target temperatures of 1000 and 2000 K.

- Retention rate

According to the figures below, the elevated temperature increase argon retention compared to 300 K. Indeed, with a gas phase of Ar, the retention rates calculated are 68% for 200 eV, 58% for 300 eV and 86% for 400 eV with a target temperature of 1000 K, 50% for 200 eV, 82 and 86 % for 300 and 400 eV with a target temperature of 2000 K. By including a gas mixture o Ar-O, the rates are 60% for 200 eV, 68% for 300 eV and 70% for 400 eV at 1000 K, 60% for 200 eV, 70% for 300 eV and 64% for 400 eV at 2000 K. By considering a gas phase of O, the rates are 62% for 200 eV, 70% for 300 eV and 74% for 400 eV at 1000 K, 50% for 200 eV and 66% for 300 and 400 eV at 2000 K.

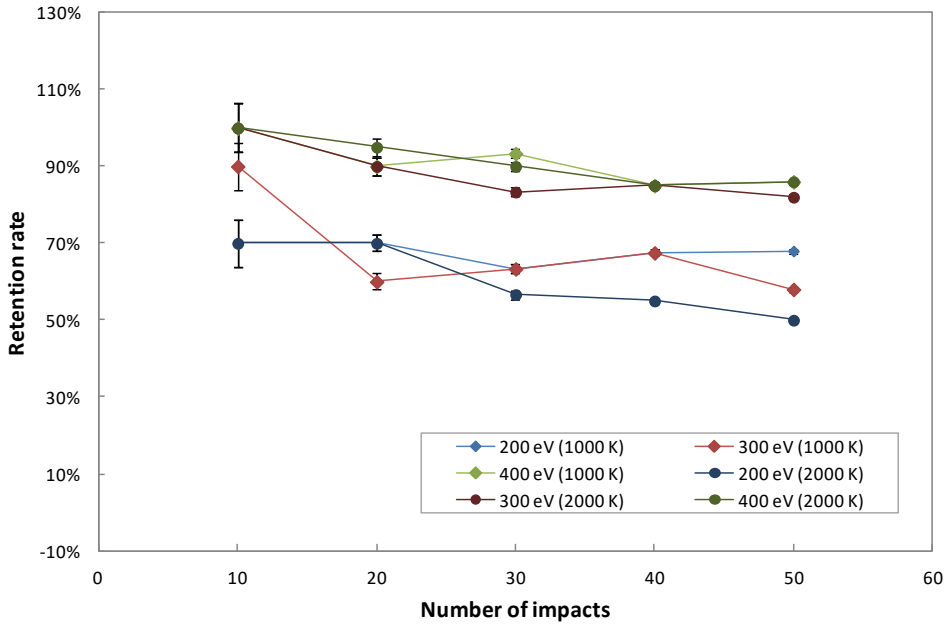

Figure 81: Retention rates in Ar gas for target temperatures of 1000 and 2000 K.

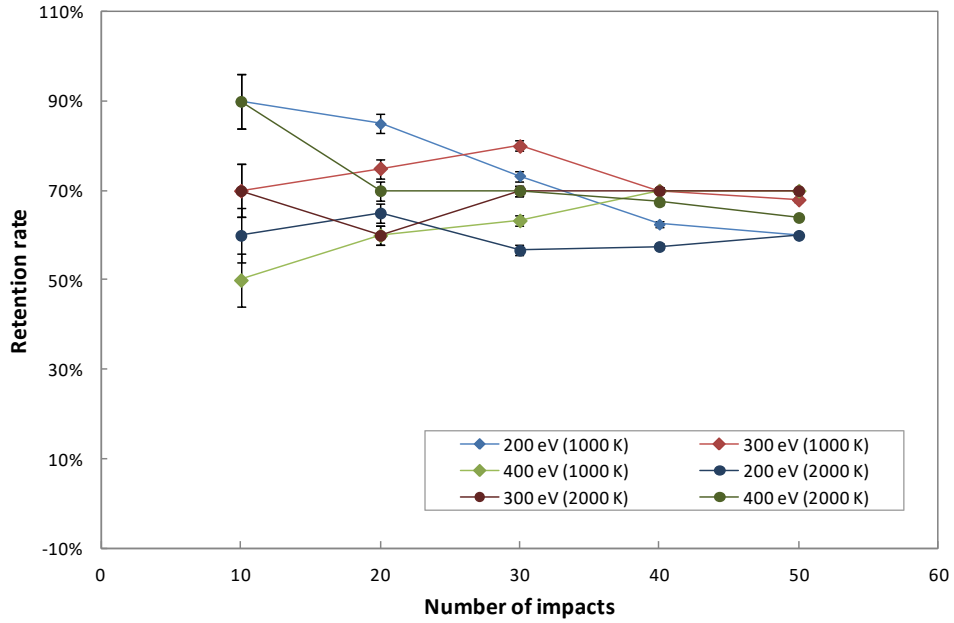

Figure 82: Retention rates in Ar-O gas for target temperatures of 1000 and 2000 K.

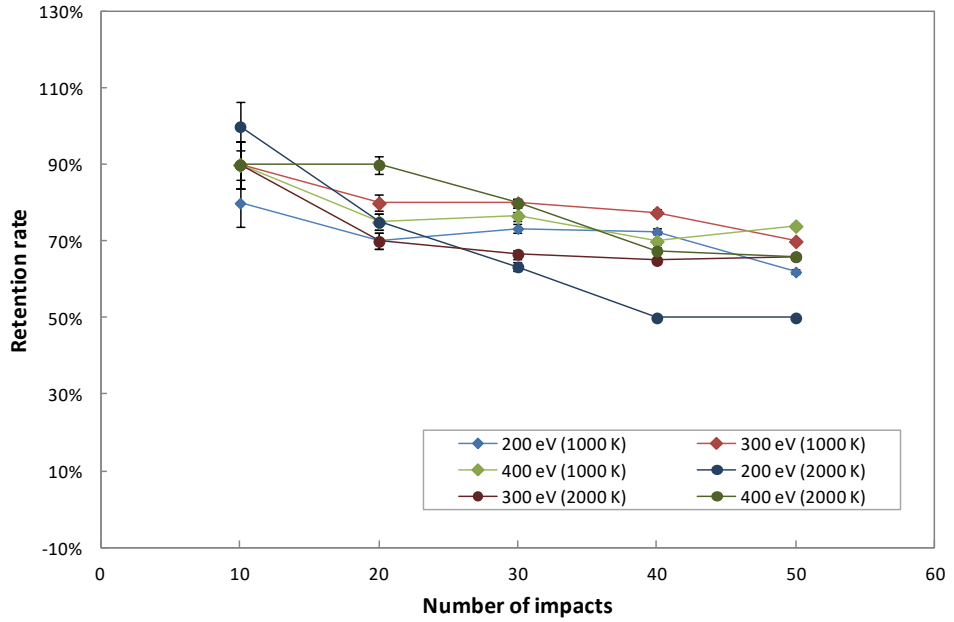

Figure 83: Retention rates in O gas for target temperatures of 1000 and 2000 K.

5.3.3. Conclusion

Non reactive and reactive hot target sputtering is investigated with two target temperatures of 1000 K and 2000 K. For some cases, convergences are obtained faster than simulations with a target temperature of 300 K. Sputtering yields and retention rates resulting with elevated target temperature are mostly higher than those with a temperature of 300 K. These simulations are therefore in good agreement with the process. However, more than 50 impacts should be taken into account to complete these results.

6. Conclusion

In this chapter, we are interested in modelling of titanium sputtering by argon ions bombardments and the calculation of sputtering and retention rates for three considered energies. Thus, molecular dynamics simulations are carried out to describe the interactions between the plasma species and the target surface. Moreover, in order to take into account longer thermal relaxation time of the system, it is possible to combine MD with MC simulations such as time-stamped force bias Monte Carlo. These tfMC simulations should not modify the target surface and can be compared to MD by quantifying a time scale.

Three studies are defined including the comparison of MD and tfMC simulations, non reactive and reactive sputtering and hot target sputtering. In the first study, the sputtering yields resulting from our MD and tfMC simulations are in good agreement with TRIM simulations [178] and Yamamura formula [124], as well as experimental results from Laegreid and Wehner [179]. However, the calculated retention rates are lower than those obtained with TRIM. This could be explained by the low considered energies. The second study shows low yields compared to the first study due to the gas phase and abnormally high reactive sputtering yields according to MD simulations which could be explained by low Ti oxides which cover the target [180, 181]. The sputtering yields and retention rates obtained by using elevated target temperature in the third study are high compared to the first one.

The following table groups the sputtering yields of titanium and argon retention rates determined from our calculations for the three considered kinetic energies.

Sputtering yields

Gas phase composition	No gas phase			Argon			Argon-Oxygen (50% - 50%)			Oxygen		
300 K												
Ion kinetic energy (eV)	**200**	**300**	**400**	**200**	**300**	**400**	**200**	**300**	**400**	**200**	**300**	**400**
MD	0.30	0.40	0.43	0.27	0.24	0.48	0.24	0.39	0.58	0.21	0.37	0.63
MD/tfMC	0.21	0.40	0.37	0.08	0.24	0.18	0.08	0.32	0.25	0.18	0.27	0.32
1000 K												
Ion kinetic energy (eV)	**200**	**300**	**400**	**200**	**300**	**400**	**200**	**300**	**400**	**200**	**300**	**400**
MD	0.32	0.52	0.46	0.28	0.46	0.62	0.12	0.26	0.34	0.12	0.30	0.64
MD/tfMC	0.18	0.44	0.56	-	-	-	-	-	-	-	-	-
2000 K												
Ion kinetic energy (eV)	**200**	**300**	**400**	**200**	**300**	**400**	**200**	**300**	**400**	**200**	**300**	**400**
MD	0.34	0.32	0.52	0.16	0.30	0.46	0.14	0.48	0.34	0.08	0.32	0.30
MD/tfMC	0.24	0.32	0.48	-	-	-	-	-	-	-	-	-

Retention rates (%)

Gas phase composition	No gas phase			Argon			Argon-Oxygen (50% - 50%)			Oxygen		
300 K												
Ion kinetic energy (eV)	**200**	**300**	**400**	**200**	**300**	**400**	**200**	**300**	**400**	**200**	**300**	**400**
MD	59	64	69	60	70	72	61	67	63	58	78	69
MD/tfMC	66	72	68	57	68	71	66	58	74	40	56	66
1000 K												
Ion kinetic energy (eV)	**200**	**300**	**400**	**200**	**300**	**400**	**200**	**300**	**400**	**200**	**300**	**400**
MD	66	66	86	68	58	86	60	68	70	62	70	74
MD/tfMC	60	76	82	-	-	-	-	-	-	-	-	-
2000 K												
Ion kinetic energy (eV)	**200**	**300**	**400**	**200**	**300**	**400**	**200**	**300**	**400**	**200**	**300**	**400**
MD	76	76	82	50	82	86	60	70	64	50	66	66
MD/tfMC	64	78	72	-	-	-	-	-	-	-	-	-

Table 5: Ti sputtering yields and Ar retention rates calculated from MD and MD /tfMC simulations.

Nevertheless, more ions impacts are required to obtain convergences for most simulations of our two last studies. Moreover, calculations according to lower and higher ions kinetic energy would complete our results.

Finally, it could be interesting to include the number of collisions that take place in the gas phase in order to model the entire sputtering deposition process [134].

IV. Conclusion

1. Summary

Magnetron sputtering is today a process widely used by industries to produce thin films and coatings for different domains of application. Thanks to higher ionization rate in the magnetic field region, it allows the synthesis of dense coatings and an increase of deposition velocity. Thus, due to the numerous advantages it offers and the possible improvements, this is the process chosen in GREMI to study growing films.

The study of growing films, and especially in the synthesis of more complex materials, requires an understanding of the mechanism involved in the process. To do this, numerical simulations are performed to complement experimental results.

The aim of this thesis work is to build a numerical model of the magnetron sputtering process by a multi-scale approach coupling CFD and MD simulations in order to obtain a representation of a real reactor system. This thesis is therefore divided in two main parts.

In the **Chapter 2**, the magnetron sputtering discharge modelling is studied according to a fluid approach using COMSOL Multiphysics® software.

Fluid approach is interesting to use due to a reasonable computation time. Moreover, our interest to use the commercial software of COMSOL Multiphysics®, in addition to the powerful solver it contains, is to allow applications of the model to different geometries such as those of GREMI reactors.

Nevertheless, the modelling of magnetron sputtering discharge using fluid approach is a key question in the case of using low pressures and strong magnetic fields. It is thus a priori not

recommended using COMSOL, since low pressures make it difficult to use a continuous medium approach.

We chose therefore to build our model on existing previous attempt, the theoretical model of Costin who obtained coherent results of the discharges characteristics with which we could compare our results. The obtained results will then give information such as incoming ions velocities transferable to our MD simulations.

The model consists on a macroscopic approach of a 2D axis-symmetric magnetron discharge in argon. The treatment of charged particles transport is described using classical drift-diffusion expression for fluxes based on Boltzmann continuity, momentum transfer and mean energy transfer. The electron flux includes also an additional flux containing the magnetic field. These equations are coupled with Poisson's equation used for the determination of the electric potential. An effective field is used for the treatment of ion transport, instead of electric field.

Solving this model is difficult due to the highly coupled non-linear equations. Hence, we chose to study the implementation and the resolution of each equation. The resulting magnetic field and electric potential are in good agreement with Costin's results. However, the resolution of charged particles transport encountered limitations in the calculation. We showed that it is mainly due to the contribution of a strong magnetic field to electrons transport equations that implies high values, especially for the values of electron mean energy, which lead to unrealistic results. By considering a weaker magnetization of the magnets giving a magnetic field a hundred times smaller at the cathode surface than that used by Costin, the electron mean energy obtained is similar to that presented by Costin.

The **Chapter 3** is focused on the microscopic approach of sputtering with the sputtering erosion of titanium by argon ions treatment in nonreactive or reactive atmosphere and by mimicking hot target, thanks to MD theory using LAMMPS code.

Molecular dynamics simulations allow the description of plasma-surface interactions that cannot be directly observable by experiments.

The results obtained are dependent on the accuracy of the interatomic potential or force field used in the simulation. Specific conditions must also be included to describe correctly the system, especially the application of a thermostat to dissipate the accumulated energy from incoming ions and the relaxation time of the target.

A hybrid approach, combining MD with Monte Carlo simulations, tfMC, has been introduced allowing considering long relaxation time. Moreover, the tfMC method makes it possible to

express the time to be compared with experiments. Two methods are thus studied: MD simulations and MD/tfMC simulations.

In this chapter, we are interested on the determination of the titanium sputtering yields and the argon retention rates for three considered energies of 200, 300 and 400 eV. The results are compared to results obtained from TRIM, ACAT program with Yamamura formula calculations and experimental measurements from Laegreid and Wehner.

Different studies are carried out considering different conditions. The first study compared MD calculations to MD/tfMC calculation for the sputtering of titanium by argon ions. The application of a longer thermal relaxation time of the target did not change the target surface morphology. Thus, the combination of MD with tfMC simulations is applicable. The resulting sputtering yields are close to TRIM, Yamamura formula as well as the experimental results from Laegreid and Wehner. The retention rates are lower than those obtained with TRIM. Typically, TRIM is expected to well work at energies above 1000 eV.

In the second study, a gas phase is added to the simulation box containing argon atoms, a mixture of argon and oxygen atoms (50% - 50%), and oxygen atoms. In most cases, low yields are obtained, compared to the first study, due to the gas phase that changes the ions incoming velocity. Abnormally high sputtering yield are also calculated in reactive sputtering according to MD simulations. Typically, in reactive sputtering, the sputtering yields should be lower than those obtained in non-reactive sputtering due to poisoning target by the formation of oxides compounds which covered the target surface. This can however be explained by the low titanium oxides target content, leading to sputtering yield close to the corresponding metal or by a very small number of oxygen atoms considered in the gas.

The third study takes into account hot target sputtering with a target temperature of 1000 and 2000 K where for most cases, the sputtering yields and retention rates calculated are high compared to those calculated at 300 K.

2. Future work

In order to improve the model and finally to reach the goal of this thesis, different studies are interesting to plan.

Indeed, the magnetron sputtering discharge modelling using COMSOL requires a comprehensive study for the resolution of the charged particles transport equations, especially

on solver settings. Actually, COMSOL solver remains a black box that makes adjustments difficult to help the system converge and avoid unrealistic results. The description of the magnetron discharge using a continuum approach allows an acceptable computation time and thus the application of the model on a real reactor configuration. It could therefore be interesting to use others types of solver. Moreover, COMSOL software is regularly improved and the future versions should be able to solve nonlinear systems as in this model.

Concerning the atomic scale of the model, and the sputtering of titanium, MD and combined MD/tfMC simulations can be completed by considering more ions impacts in order to obtain more accurate values of sputtering yields and retention rates. This will then allow us to determine the energy distribution of the sputtered titanium. Moreover, it is interesting to work with other energies lower and higher than the three considered energies of our calculations.

Hot target sputtering can also be simulated according to temperatures used experimentally.

The simulations boxes including a gas phase should take into account the number of collisions that take place in the gas phase to obtain a model close to the reality. Thus, we can determine the number of atoms in the gas phase according to the pressure applied by comparing with experiments. Then, the deposition process could be added to our model in order to model the entire sputtering deposition mechanism of titanium by argon ions bombardments.

References

[1] I. Langmuir, 'Oscillations in Ionized Gases', *Proc. Natl. Acad. Sci.*, vol. 14, no. 8, pp. 627–637, Aug. 1928.

[2] A. Bogaerts, E. Neyts, R. Gijbels, and J. Van Der Mullen, 'Gas discharge plasmas and their applications', *Spectrochimica Acta Part B : Atomic Spectroscopy*, vol. 57, 2002.

[3] G. E. Morfill, T. Shimizu, B. Steffes, and H.-U. Schmidt, 'Nosocomial infections—a new approach towards preventive medicine using plasmas', *New J. Phys.*, vol. 11, no. 11, p. 115019, Nov. 2009.

[4] J. Schlegel, J. Köritzer, and V. Boxhammer, 'Plasma in cancer treatment', *Clin. Plasma Med.*, vol. 1, no. 2, pp. 2–7, Dec. 2013.

[5] F. Fabry, C. Rehmet, V. Rohani, and L. Fulcheri, 'Waste Gasification by Thermal Plasma: A Review', *Waste Biomass Valorization*, vol. 4, no. 3, pp. 421–439, Sep. 2013.

[6] M. Magureanu *et al.*, 'Degradation of antibiotics in water by non-thermal plasma treatment', *Water Research*, vol. 45, 2011.

[7] J. Van Durme, J. Dewulf, C. Leys, and H. Van Langenhove, 'Combining non-thermal plasma with heterogeneous catalysis in waste gas treatment: A review', *Appl. Catal. B Environ.*, vol. 78, no. 3, pp. 324–333, Feb. 2008.

[8] J. Jiang *et al.*, 'Effect of Cold Plasma Treatment on Seed Germination and Growth of Wheat', *Plasma Sci. Technol.*, vol. 16, no. 1, pp. 54–58, Jan. 2014.

[9] R. R. Boyer, 'An overview on the use of titanium in the aerospace industry', *Mater. Sci. Eng. A*, vol. 213, no. 1, pp. 103–114, Aug. 1996.

[10] K. Reichelt and X. Jiang, 'The preparation of thin films by physical vapour deposition methods', *Thin Solid Films*, vol. 191, no. 1, pp. 91–126, Oct. 1990.

[11] A. Billard and F. Perry, *Pulverisation cathodique magnetron*. Ed. Techniques Ingénieur.

[12] S. Takeda, S. Suzuki, H. Odaka, and H. Hosono, 'Photocatalytic TiO2 thin film deposited onto glass by DC magnetron sputtering', *Thin Solid Films*, vol. 392, no. 2, pp. 338–344, Jul. 2001.

[13] K. Ellmer, 'Magnetron sputtering of transparent conductive zinc oxide: relation between the sputtering parameters and the electronic properties', *J. Phys. Appl. Phys.*, vol. 33, no. 4, pp. R17–R32, Feb. 2000.

[14] A. K. Menon and B. K. Gupta, 'Nanotechnology: a data storage perspective', *Nanostructured Mater.*, vol. 11, no. 8, pp. 965–986, Nov. 1999.

[15] E. Budke, J. Krempel-Hesse, H. Maidhof, and H. Schüssler, 'Decorative hard coatings with improved corrosion resistance', *Surf. Coat. Technol.*, vol. 112, no. 1, pp. 108–113, Feb. 1999.

[16] P. Sigmund, *Element of Sputtering Theory - Chapter 1 from Nanofabrication by Ion-Beam Sputtering: Fundamentals and Appications*. Som Tapobrata, Kanjilal Dinakar - CRC Press, 2012.

[17] J. Musil, 'Recent advances in magnetron sputtering technology', *Surf. Coat. Technol.*, vol. 100–101, pp. 280–286, Mar. 1998.

[18] M. M. Waite, S. Ismat Shah, and D. A. Glocker, *Sputtering Sources - Chapter 15 from 50 Years of VacuumCoating Technology and the growth of the Society of Vacuum Coaters*. Donald M. Mattox and Vivienne Harwood Mattox, eds., Society of Vacuum Coaters, 2007.

[19] J. van Dijk, G. M. W. Kroesen, and A. Bogaerts, 'Plasma modelling and numerical simulation', *J. Phys. Appl. Phys.*, vol. 42, no. 19, p. 190301, Sep. 2009.

[20] W. R. Grove, 'On the Electro-Chemical Polarity of Gases', *Philos. Trans. R. Soc. Lond.*, vol. 142, pp. 87–101, 1852.

[21] P. Sigmund, 'Sputtering by ion bombardment theoretical concepts', in *Sputtering by Particle Bombardment I: Physical Sputtering of Single-Element Solids*, R. Behrisch, Ed. Berlin, Heidelberg: Springer Berlin Heidelberg, 1981, pp. 9–71.

[22] M. W. Thompson, 'Physical mechanisms of sputtering', *Phys. Rep.*, vol. 69, no. 4, pp. 335–371, Mar. 1981.

[23] F. M. Penning, 'Die glimmentladung bei niedrigem druck zwischen koaxialen zylindern in einem axialen magnetfeld', *Physica*, vol. 3, no. 9, pp. 873–894, Nov. 1936.

[24] A. W. Hull, 'The magnetron', *J. Am. Inst. Electr. Eng.*, vol. 40, no. 9, pp. 715–723, Sep. 1921.

[25] J. S. Chapin, 'Sputtering process and apparatus', US4166018A, 28-Aug-1979.

[26] A. S. Penfold, 'Early days of magnetron sputtering—an enigma', *Thin Solid Films*, vol. 171, no. 1, pp. 99–108, Apr. 1989.

[27] R. Kukla, 'Magnetron sputtering on large scale substrates: an overview on the state of the art', *Surf. Coat. Technol.*, vol. 93, no. 1, pp. 1–6, Aug. 1997.

[28] S. Swann, 'Magnetron sputtering', *Phys. Technol.*, vol. 19, no. 2, p. 67, 1988.

[29] J. A. Thornton, 'Substrate heating in cylindrical magnetron sputtering sources', *Thin Solid Films*, vol. 54, no. 1, pp. 23–31, Oct. 1978.

[30] P. J. Kelly and R. D. Arnell, 'Magnetron sputtering: a review of recent developments and applications', *Vacuum*, vol. 56, no. 3, pp. 159–172, Mar. 2000.

[31] G. Bräuer, B. Szyszka, M. Vergöhl, and R. Bandorf, 'Magnetron sputtering – Milestones of 30 years', *Vacuum*, vol. 84, no. 12, pp. 1354–1359, Jun. 2010.

[32] R. D. Arnell and P. J. Kelly, 'Recent advances in magnetron sputtering', *Surf. Coat. Technol.*, vol. 112, no. 1–3, pp. 170–176, Feb. 1999.

[33] J. Musil, 'Low-pressure magnetron sputtering', *Vacuum*, vol. 50, no. 3–4, pp. 363–372, Jul. 1998.

[34] J. S. Logan, 'R.F. diode sputtering', *Thin Solid Films*, vol. 188, no. 2, pp. 307–321, Jul. 1990.

[35] J. F. Pierson, D. Wiederkehr, and A. Billard, 'Reactive magnetron sputtering of copper, silver, and gold', *Thin Solid Films*, vol. 478, no. 1, pp. 196–205, May 2005.

[36] J. Musil, P. Baroch, J. Vlček, K. H. Nam, and J. G. Han, 'Reactive magnetron sputtering of thin films: present status and trends', *Thin Solid Films*, vol. 475, no. 1, pp. 208–218, Mar. 2005.

[37] G. Bräuer, J. Szczyrbowski, and G. Teschner, 'Mid frequency sputtering — a novel tool for large area coating', *Surf. Coat. Technol.*, vol. 94–95, pp. 658–662, Oct. 1997.

[38] S. Berg and T. Nyberg, 'Fundamental understanding and modeling of reactive sputtering processes', *Thin Solid Films*, vol. 476, no. 2, pp. 215–230, Apr. 2005.

[39] G. Golan and A. Axelevitch, 'Novel method of low-vacuum plasma triode sputtering', *Microelectron. J.*, vol. 33, no. 8, pp. 651–657, Aug. 2002.

[40] J. Musil, S. Kadlec, V. Valvoda, R. Kužel, and R. Černý, 'Ion-assisted sputtering of TiN films', *Surf. Coat. Technol.*, vol. 43–44, pp. 259–269, Dec. 1990.

[41] W.-D. Münz, ‘The unbalanced magnetron: current status of development’, *Surf. Coat. Technol.*, vol. 48, no. 1, pp. 81–94, Oct. 1991.

[42] J. S. Colligon, ‘Ion–assisted sputter deposition’, *Philos. Trans. R. Soc. Lond. Ser. Math. Phys. Eng. Sci.*, vol. 362, no. 1814, pp. 103–116, Jan. 2004.

[43] C. Weissmantel *et al.*, ‘Preparation of hard coatings by ion beam methods’, *Thin Solid Films*, vol. 63, no. 2, pp. 315–325, Nov. 1979.

[44] J. Musil and J. Vlček, ‘Magnetron sputtering of films with controlled texture and grain size’, *Mater. Chem. Phys.*, vol. 54, no. 1–3, pp. 116–122, Jul. 1998.

[45] W. D. Sproul, ‘Multi-cathode unbalanced magnetron sputtering systems’, *Surf. Coat. Technol.*, vol. 49, no. 1, pp. 284–289, Dec. 1991.

[46] R. L. Cormia, T. A. Trumbly, and S. Andresen, ‘Method for coating a substrate’, US4046659A, 06-Sep-1977.

[47] R. J. Hill and F. Jansen, ‘The use of ac power on cylindrical magnetrons’, *J. Non-Cryst. Solids*, vol. 218, pp. 35–37, Sep. 1997.

[48] J. Szczyrbowski, G. Bräuer, G. Teschner, and A. Zmelty, ‘Antireflective coatings on large scale substrates produced by reactive twin-magnetron sputtering’, *J. Non-Cryst. Solids*, vol. 218, pp. 25–29, Sep. 1997.

[49] S. Schiller, K. Goedicke, J. Reschke, V. Kirchhoff, S. Schneider, and F. Milde, ‘Pulsed magnetron sputter technology’, *Surf. Coat. Technol.*, vol. 61, no. 1, pp. 331–337, Dec. 1993.

[50] V. Kirchhoff, T. Kopte, T. Winkler, M. Schulze, and P. Wiedemuth, ‘Dual magnetron sputtering (DMS) system with sine-wave power supply for large-area coating’, *Surf. Coat. Technol.*, vol. 98, no. 1, pp. 828–833, Jan. 1998.

[51] M. S. Wong, W. J. Chia, P. Yashar, J. M. Schneider, W. D. Sproul, and S. A. Barnett, ‘High-rate reactive d.c. magnetron sputtering of ZrOx coatings’, *Surf. Coat. Technol.*, vol. 86–87, pp. 381–387, Dec. 1996.

[52] I. K. Fetisov, A. A. Filippov, G. V. Khodachenko, D. V. Mozgrin, and A. A. Pisarev, ‘Impulse irradiation plasma technology for film deposition’, *Vacuum*, vol. 53, no. 1, pp. 133–136, May 1999.

[53] V. Kouznetsov, K. Macák, J. M. Schneider, U. Helmersson, and I. Petrov, ‘A novel pulsed magnetron sputter technique utilizing very high target power densities’, *Surf. Coat. Technol.*, vol. 122, no. 2, pp. 290–293, Dec. 1999.

[54] K. Sarakinos, J. Alami, and S. Konstantinidis, ‘High power pulsed magnetron sputtering: A review on scientific and engineering state of the art’, *Surf. Coat. Technol.*, vol. 204, no. 11, pp. 1661–1684, Feb. 2010.

[55] W.-D. Münz, M. Schenkel, S. Kunkel, J. Paulitsch, and K. Bewilogua, ‘Industrial applications of HIPIMS’, *J. Phys. Conf. Ser.*, vol. 100, no. 8, p. 082001, Mar. 2008.

[56] E. Wallin and U. Helmersson, ‘Hysteresis-free reactive high power impulse magnetron sputtering’, *Thin Solid Films*, vol. 516, no. 18, pp. 6398–6401, Jul. 2008.

[57] M. Audronis, V. Bellido-Gonzalez, and B. Daniel, ‘Control of reactive high power impulse magnetron sputtering processes’, *Surf. Coat. Technol.*, vol. 204, no. 14, pp. 2159–2164, Apr. 2010.

[58] M. Audronis and V. Bellido-Gonzalez, ‘Hysteresis behaviour of reactive high power impulse magnetron sputtering’, *Thin Solid Films*, vol. 518, no. 8, pp. 1962–1965, Feb. 2010.

[59] T. Kubart, M. Aiempanakit, J. Andersson, T. Nyberg, S. Berg, and U. Helmersson, ‘Studies of hysteresis effect in reactive HiPIMS deposition of oxides’, *Surf. Coat. Technol.*, vol. 205, pp. S303–S306, Jul. 2011.

[60] M. Aiempanakit, T. Kubart, P. Larsson, K. Sarakinos, J. Jensen, and U. Helmersson, 'Hysteresis and process stability in reactive high power impulse magnetron sputtering of metal oxides', *Thin Solid Films*, vol. 519, no. 22, pp. 7779–7784, Sep. 2011.

[61] D. A. Golosov, 'Balanced magnetic field in magnetron sputtering systems', *Vacuum*, vol. 139, pp. 109–116, May 2017.

[62] P. J. Kelly, R. D. Arnell, W. Ahmed, and A. Afzal, 'Novel engineering coatings produced by closed-field unbalanced magnetron sputtering', *Mater. Des.*, vol. 17, no. 4, pp. 215–219, Jan. 1996.

[63] D. P. Monaghan, D. G. Teer, K. C. Laing, I. Efeoglu, and R. D. Arnell, 'Deposition of graded alloy nitride films by closed field unbalanced magnetron sputtering', *Surf. Coat. Technol.*, vol. 59, no. 1, pp. 21–25, Oct. 1993.

[64] D. P. Monaghan, D. G. Teer, P. A. Logan, I. Efeoglu, and R. D. Arnell, 'Deposition of wear resistant coatings based on diamond like carbon by unbalanced magnetron sputtering', *Surf. Coat. Technol.*, vol. 60, no. 1, pp. 525–530, Oct. 1993.

[65] U. H. Kwon, S. H. Choi, Y. H. Park, and W. J. Lee, 'Multi-scale simulation of plasma generation and film deposition in a circular type DC magnetron sputtering system', *Thin Solid Films*, vol. 475, no. 1–2, pp. 17–23, Mar. 2005.

[66] S. Kadlec, 'Computer simulation of magnetron sputtering — Experience from the industry', *Surf. Coat. Technol.*, vol. 202, no. 4–7, pp. 895–903, Dec. 2007.

[67] A. Bogaerts, I. Kolev, and G. Buyle, 'Modeling of the Magnetron Discharge', in *Reactive Sputter Deposition*, D. Depla and S. Mahieu, Eds. Berlin, Heidelberg: Springer Berlin Heidelberg, 2008, pp. 61–130.

[68] A. Bogaerts *et al.*, 'Computer modelling of magnetron discharges', *J. Phys. Appl. Phys.*, vol. 42, no. 19, p. 194018, Sep. 2009.

[69] J. Kageyama, M. Yoshimoto, A. Matsuda, Y. Akao, and E. Shidoji, 'Numerical simulation of plasma confinement in DC magnetron sputtering under different magnetic fields and anode structures', *Jpn. J. Appl. Phys.*, vol. 53, no. 8, p. 088001, Jul. 2014.

[70] S. Kondo and K. Nanbu, 'A self-consistent numerical analysis of a planar dc magnetron discharge by the particle-in-cell/Monte Carlo method', *J. Phys. Appl. Phys.*, vol. 32, no. 10, pp. 1142–1152, Jan. 1999.

[71] C. Costin, L. Marques, G. Popa, and G. Gousset, 'Two-dimensional fluid approach to the dc magnetron discharge', *Plasma Sources Sci. Technol.*, vol. 14, no. 1, p. 168, 2005.

[72] I. Kolev and A. Bogaerts, 'PIC – MCC Numerical Simulation of a DC Planar Magnetron', *Plasma Process. Polym.*, vol. 3, no. 2, pp. 127–134, Feb. 2006.

[73] E. Bultinck and A. Bogaerts, 'Characterization of an Ar/O 2 magnetron plasma by a multi-species Monte Carlo model', *Plasma Sources Sci. Technol.*, vol. 20, no. 4, p. 045013, 2011.

[74] K. Nanbu, S. Segawa, and S. Kondo, 'Self-consistent particle simulation of three-dimensional dc magnetron discharge', *Vacuum*, vol. 47, no. 6, pp. 1013–1016, Jun. 1996.

[75] *COMSOL Multiphysics Reference Manual*, vol. 5.2. COMSOL Multiphysics.

[76] C. K. Birdsall, 'Particle-in-cell charged-particle simulations, plus Monte Carlo collisions with neutral atoms, PIC-MCC', *IEEE Trans. Plasma Sci.*, vol. 19, no. 2, pp. 65–85, Apr. 1991.

[77] K. Nanbu and S. Kondo, 'Analysis of three-dimensional DC magnetron discharge by Particle-in-Cell/Monte Carlo Method', *Jpn. J. Appl. Phys.*, vol. 36, pp. 4808–4814, 1997.

[78] T. A. van der Straaten, N. F. Cramer, I. S. Falconer, and B. W. James, 'The cylindrical DC magnetron discharge: I. Particle-in-cell simulation', *J. Phys. Appl. Phys.*, vol. 31, no. 2, p. 177, 1998.

[79] C. H. Shon and J. K. Lee, 'Modeling of magnetron sputtering plasmas', *Appl. Surf. Sci.*, vol. 192, no. 1–4, pp. 258–269, May 2002.

[80] F. Guimaraes and J. Bretagne, 'Study of an argon magnetron discharge used for molybdenum sputtering. I. Collisional radiative model', *Plasma Sources Sci. Technol.*, vol. 2, no. 3, pp. 127–137, Aug. 1993.

[81] F. Guimaraes, J. B. Almeida, and J. Bretagne, 'Study of an argon magnetron discharge used for molybdenum sputtering. II. Spectroscopic analysis and comparison with the model', *Plasma Sources Sci. Technol.*, vol. 2, no. 3, pp. 138–144, Aug. 1993.

[82] W. Trennepohl, J. Bretagne, G. Gousset, D. Pagnon, and M. Touzeau, 'Modelling of an reactive magnetron discharge used for deposition of chromium oxide', *Plasma Sources Sci. Technol.*, vol. 5, no. 4, pp. 607–621, Nov. 1996.

[83] C. Costin, *Modélisation d'une décharge magnétron DC dans l'argon et en mélanges argon-oxygène par un modèle fluide*. Paris 11, 2005.

[84] J. W. Bradley, 'The plasma properties adjacent to the target in a magnetron sputtering source', *Plasma Sources Sci. Technol.*, vol. 5, no. 4, pp. 622–631, 1996.

[85] J. W. Bradley and G. Lister, 'Model of the cathode fall region in magnetron discharges', *Plasma Sources Sci. Technol.*, vol. 6, no. 4, p. 524, 1997.

[86] C. Costin, G. Gousset, and G. Popa, 'Modélisation d'une décharge magnétron dc dans l'Argon par un modèle fluide', *Le Vide*, vol. 57, no. 304, pp. 308–315, 2002.

[87] I. Kolev and A. Bogaerts, 'Numerical Models of the Planar Magnetron Glow Discharges', *Contrib. Plasma Phys.*, vol. 44, no. 7–8, pp. 582–588, 2004.

[88] E. Shidoji, N. Nakano, and T. Makabe, 'Numerical simulation of the discharge in d.c. magnetron sputtering', *Thin Solid Films*, vol. 351, no. 1, pp. 37–41, Aug. 1999.

[89] E. Shidoji, K. Ness, and T. Makabe, 'Influence of gas pressure and magnetic field upon dc magnetron discharge', *Vacuum*, vol. 60, no. 3, pp. 299–306, Mar. 2001.

[90] E. Shidoji and T. Makabe, 'Magnetron plasma structure with strong magnetic field', *Thin Solid Films*, vol. 442, no. 1, pp. 27–31, Oct. 2003.

[91] Jimenez, F., Ekpe, S. D., and Dew, S. K., 'Modeling of Low Pressure Magnetron Plasma Discharge', *Excerpt Proc. COMSOL Conf. 2007 Boston*.

[92] W. Eckstein, 'Sputtering Yields', in *Sputtering by Particle Bombardment: Experiments and Computer Calculations from Threshold to MeV Energies*, Berlin, Heidelberg: Springer Berlin Heidelberg, 2007, pp. 33–187.

[93] J. Stark, *Die elektrizität in gasen*. J.A. Barth, 1902.

[94] P. Sigmund, 'Mechanisms and theory of physical sputtering by particle impact', *Nucl. Instrum. Methods Phys. Res. Sect. B Beam Interact. Mater. At.*, vol. 27, no. 1, pp. 1–20, Jun. 1987.

[95] R. Behrisch and W. Eckstein, *Sputtering by Particle Bombardment: Experiments and Computer Calculations from Threshold to MeV Energies*. Springer Science & Business Media, 2007.

[96] G. Falcone, 'Theory of collisional sputtering', *Surf. Sci.*, vol. 187, no. 1, pp. 212–222, Aug. 1987.

[97] W. Brandt and R. Laubert, 'Unified sputtering theory', *Nucl. Instrum. Methods*, vol. 47, no. 2, pp. 201–209, Feb. 1967.

[98] P. Sigmund, 'Theory of Sputtering. I. Sputtering Yield of Amorphous and Polycrystalline Targets', *Phys. Rev.*, vol. 184, no. 2, pp. 383–416, Aug. 1969.

[99] W. Eckstein and H. M. Urbassek, 'Computer Simulation of the Sputtering Process', in *Sputtering by Particle Bonbardment*, vol. 110, Springer, Berlin, Heidelberg, 2007, pp. 22–31.

[100] W. Möller, W. Eckstein, and J. P. Biersack, ‘Tridyn-binary collision simulation of atomic collisions and dynamic composition changes in solids’, *Comput. Phys. Commun.*, vol. 51, no. 3, pp. 355–368, Nov. 1988.

[101] L. Bukonte, F. Djurabekova, J. Samela, K. Nordlund, S. A. Norris, and M. J. Aziz, ‘Comparison of molecular dynamics and binary collision approximation simulations for atom displacement analysis’, *Nucl. Instrum. Methods Phys. Res. Sect. B Beam Interact. Mater. At.*, vol. 297, pp. 23–28, Feb. 2013.

[102] Y. Yamamura and W. Takeuchi, ‘Monocrystal sputtering by the computer simulation code acoct’, *Nucl. Instrum. Methods Phys. Res. Sect. B Beam Interact. Mater. At.*, vol. 29, no. 3, pp. 461–470, Dec. 1987.

[103] M. M. Jakas and D. E. Harrison, ‘Many-body effects in atomic-collision cascades’, *Phys. Rev. Lett.*, vol. 55, no. 17, pp. 1782–1785, Oct. 1985.

[104] Y. Yamamura, ‘Sputtering by cluster ions’, *Nucl. Instrum. Methods Phys. Res. Sect. B Beam Interact. Mater. At.*, vol. 33, no. 1, pp. 493–496, Jun. 1988.

[105] W. Möller and W. Eckstein, ‘Tridyn — A TRIM simulation code including dynamic composition changes’, *Nucl. Instrum. Methods Phys. Res. Sect. B Beam Interact. Mater. At.*, vol. 2, no. 1, pp. 814–818, Mar. 1984.

[106] H. Hofsäss, K. Zhang, and A. Mutzke, ‘Simulation of ion beam sputtering with SDTrimSP, TRIDYN and SRIM’, *Appl. Surf. Sci.*, vol. 310, pp. 134–141, Aug. 2014.

[107] W. Eckstein, R. Dohmen, A. Mutzke, and R. Schneider, ‘SDTrimSP: A Monte-Carlo Code for Calculating Collision Phenomena in Randomized Targets’, *IPP Rep.*, 2007.

[108] A. Mutzke, W. Eckstein, R. Schneider, and R. Dohmen, ‘SDTrimSP: Version 5.00’, *IPP Rep.*, 2011.

[109] R. P. Webb and D. E. Harrison, ‘A computer simulation of high energy density cascades’, *Nucl. Instrum. Methods Phys. Res. Sect. B Beam Interact. Mater. At.*, vol. 2, no. 1, pp. 660–665, Mar. 1984.

[110] H. M. Urbassek, ‘Molecular-dynamics simulation of sputtering’, *Nucl. Instrum. Methods Phys. Res. Sect. B Beam Interact. Mater. At.*, vol. 122, no. 3, pp. 427–441, Feb. 1997.

[111] S. Plimpton, ‘Fast Parallel Algorithms for Short-Range Molecular Dynamics’, *J. Comput. Phys.*, vol. 117, no. 1, pp. 1–19, Mar. 1995.

[112] P. Brault, S. Chuon, and J.-M. Bauchire, ‘Molecular Dynamics Simulations of Platinum Plasma Sputtering: A Comparative Case Study’, *Plasma Phys.*, p. 20, 2016.

[113] J. M. Haile, *Molecular Dynamics Simulation: Elementary Methods*, 1st ed. New York, NY, USA: John Wiley & Sons, Inc., 1992.

[114] E. C. Neyts and P. Brault, ‘Molecular Dynamics Simulations for Plasma-Surface Interactions’, *Plasma Process. Polym.*, vol. 14, no. 1–2, p. 1600145, 2017.

[115] P. Brault and E. C. Neyts, ‘Molecular dynamics simulations of supported metal nanocatalyst formation by plasma sputtering’, *Catal. Today*, vol. 256, pp. 3–12, Nov. 2015.

[116] D. B. Graves and P. Brault, ‘Molecular dynamics for low temperature plasma–surface interaction studies’, *J. Phys. Appl. Phys.*, vol. 42, no. 19, p. 194011, 2009.

[117] Yamazaki, T, Matsuda, K, and Nakatani, H, ‘Effect of Angular Distribution of Ejected Atoms from a Target on the Uniformity of Thickness and Composition of MoSix Sputtering Films’, *Jpn. J. Appl. Phys.*, vol. 29, no. 7, 1990.

[118] H. H. Andersen, B. Stenum, T. Sørensen, and H. J. Whitlow, ‘Angular distribution of particles sputtered from Cu, Pt and Ge targets by keV Ar+ ion bombardment’, *Nucl. Instrum. Methods Phys. Res. Sect. B Beam Interact. Mater. At.*, vol. 6, no. 3, pp. 459–465, Feb. 1985.

[119] H. H. Andersen, ‘Sputtering from atomic-collision cascades’, *Nucl. Instrum. Methods Phys. Res. Sect. B Beam Interact. Mater. At.*, vol. 33, no. 1, pp. 466–473, Jun. 1988.

[120] J. Bohdansky, ‘A universal relation for the sputtering yield of monatomic solids at normal ion incidence’, *Nucl. Instrum. Methods Phys. Res. Sect. B Beam Interact. Mater. At.*, vol. 2, no. 1, pp. 587–591, Mar. 1984.

[121] Y. Yamamura and J. Bohdansky, ‘Few collisions approach for threshold sputtering’, *Vacuum*, vol. 35, no. 12, pp. 561–571, Dec. 1985.

[122] Y. Yamamura, ‘Theory of sputtering and comparison to experimental data’, *Nucl. Instrum. Methods Phys. Res.*, vol. 194, no. 1–3, pp. 515–522, Mar. 1982.

[123] N. Matsunami *et al.*, ‘Energy dependence of the ion-induced sputtering yields of monatomic solids’, *At. Data Nucl. Data Tables*, vol. 31, no. 1, pp. 1–80, Jul. 1984.

[124] Y. Yamamura and H. Tawara, ‘Energy dependence of ion-induced sputtering yields from monatomic solids at normal incidence’, *At. Data Nucl. Data Tables*, vol. 62, no. 2, pp. 149–253, Mar. 1996.

[125] W. Eckstein and R. Preuss, ‘New fit formulae for the sputtering yield’, *J. Nucl. Mater.*, vol. 320, no. 3, pp. 209–213, Aug. 2003.

[126] L. Xie, ‘Simulations du dépôt par pulvérisation plasma et de la croissance de couches minces’, thesis, Orléans, 2013.

[127] L. L. Alves, G. Gousset, and C. M. Ferreira, ‘Self-contained solution to the spatially inhomogeneous electron Boltzmann equation in a cylindrical plasma positive column’, *Phys. Rev. E*, vol. 55, no. 1, pp. 890–906, Jan. 1997.

[128] E. Kawamura, D. B. Graves, and M. A. Lieberman, ‘Fast 2D hybrid fluid-analytical simulation of inductive/capacitive discharges’, *Plasma Sources Sci. Technol.*, vol. 20, no. 3, p. 035009, 2011.

[129] R. Courant, ‘Variational methods for the solution of problems of equilibrium and vibrations’, *Bull. Am. Math. Soc.*, vol. 49, no. 1, pp. 1–23, Jan. 1943.

[130] F. Williamson, ‘Richard courant and the finite element method: A further look’, *Hist. Math.*, vol. 7, no. 4, pp. 369–378, Nov. 1980.

[131] G. Pelosi, ‘The finite-element method, Part I: R. L. Courant [Historical Corner]’, *IEEE Antennas Propag. Mag.*, vol. 49, no. 2, pp. 180–182, Apr. 2007.

[132] Multiphysics Cyclopedia, https://www.comsol.com/multiphysics.

[133] L. Xie, P. Brault, J.-M. Bauchire, A.-L. Thomann, and L. Bedra, ‘Molecular dynamics simulations of clusters and thin film growth in the context of plasma sputtering deposition’, *J. Phys. Appl. Phys.*, vol. 47, no. 22, p. 224004, May 2014.

[134] P. Brault, ‘Multiscale Molecular Dynamics Simulation of Plasma Processing: Application to Plasma Sputtering’, *Front. Phys.*, vol. 6, p. 59 (7 pages), Jun. 2018.

[135] D. M. Brunette, P. Tengvall, M. Textor, and P. Thomsen, *Titanium in Medicine: Material Science, Surface Science, Engineering, Biological Responses and Medical Applications*. Springer Science & Business Media, 2012.

[136] Ph. Roquiny, F. Bodart, and G. Terwagne, ‘Colour control of titanium nitride coatings produced by reactive magnetron sputtering at temperature less than 100°C’, *Surf. Coat. Technol.*, vol. 116–119, pp. 278–283, Sep. 1999.

[137] S. B. Amor, G. Baud, J. P. Besse, and M. Jacquet, ‘Structural and optical properties of sputtered Titania films’, *Mater. Sci. Eng. B*, vol. 47, no. 2, pp. 110–118, Jun. 1997.

[138] S. K. Zheng, T. M. Wang, G. Xiang, and C. Wang, ‘Photocatalytic activity of nanostructured TiO2 thin films prepared by dc magnetron sputtering method’, *Vacuum*, vol. 62, no. 4, pp. 361–366, Jun. 2001.

[139] F.-M. Liu and T.-M. Wang, ‘Surface and optical properties of nanocrystalline anatase titania films grown by radio frequency reactive magnetron sputtering’, *Appl. Surf. Sci.*, vol. 195, no. 1, pp. 284–290, Jul. 2002.

[140] P. J. Kelly, C. F. Beevers, P. S. Henderson, R. D. Arnell, J. W. Bradley, and H. Bäcker, ‘A comparison of the properties of titanium-based films produced by pulsed and continuous DC magnetron sputtering’, *Surf. Coat. Technol.*, vol. 174–175, pp. 795–800, Sep. 2003.

[141] B. Karunagaran, K. Kim, D. Mangalaraj, J. Yi, and S. Velumani, ‘Structural, optical and Raman scattering studies on DC magnetron sputtered titanium dioxide thin films’, *Sol. Energy Mater. Sol. Cells*, vol. 88, no. 2, pp. 199–208, Jul. 2005.

[142] S. Konstantinidis, J. P. Dauchot, and M. Hecq, ‘Titanium oxide thin films deposited by high-power impulse magnetron sputtering’, *Thin Solid Films*, vol. 515, no. 3, pp. 1182–1186, Nov. 2006.

[143] C. J. Tavares *et al.*, ‘Reactive sputtering deposition of photocatalytic TiO2 thin films on glass substrates’, *Mater. Sci. Eng. B*, vol. 138, no. 2, pp. 139–143, Mar. 2007.

[144] B. Karunagaran, P. Uthirakumar, S. J. Chung, S. Velumani, and E.-K. Suh, ‘TiO2 thin film gas sensor for monitoring ammonia’, *Mater. Charact.*, vol. 58, no. 8, pp. 680–684, Aug. 2007.

[145] P. J. Kelly *et al.*, ‘Deposition of photocatalytic titania coatings on polymeric substrates by HiPIMS’, *Vacuum*, vol. 86, no. 12, pp. 1880–1882, Jul. 2012.

[146] Q. M. Wang, S.-H. Kwon, K. N. Hui, D.-I. Kim, K. S. Hui, and K. H. Kim, ‘Synthesis and properties of crystalline TiO2 films deposited by a HIPIMS+ technique’, *Vacuum*, vol. 89, pp. 90–95, Mar. 2013.

[147] D. Mercs, F. Perry, and A. Billard, ‘Hot target sputtering: A new way for high-rate deposition of stoichiometric ceramic films’, *Surf. Coat. Technol.*, vol. 201, no. 6, pp. 2276–2281, Dec. 2006.

[148] J. Domaradzki, D. Kaczmarek, E. L. Prociow, A. Borkowska, D. Schmeisser, and G. Beuckert, ‘Microstructure and optical properties of TiO2 thin films prepared by low pressure hot target reactive magnetron sputtering’, *Thin Solid Films*, vol. 513, no. 1, pp. 269–274, Aug. 2006.

[149] B. J. Alder and T. E. Wainwright, ‘Phase Transition for a Hard Sphere System’, *J. Chem. Phys.*, vol. 27, no. 5, pp. 1208–1209, Nov. 1957.

[150] B. J. Alder and T. E. Wainwright, ‘Studies in Molecular Dynamics. I. General Method’, *J. Chem. Phys.*, vol. 31, no. 2, pp. 459–466, Aug. 1959.

[151] M. P. Allen and D. J. Tildesley, *Computer Simulation of Liquids*. Oxford University Press, 1991.

[152] D. E. Harrison, N. S. Levy, J. P. Johnson, and H. M. Effron, ‘Computer Simulation of Sputtering’, *J. Appl. Phys.*, vol. 39, no. 8, pp. 3742–3761, Jul. 1968.

[153] L. Verlet, ‘Computer “Experiments” on Classical Fluids. I. Thermodynamical Properties of Lennard-Jones Molecules’, *Phys. Rev.*, vol. 159, no. 1, pp. 98–103, Jul. 1967.

[154] W. Swope, H. Andersen, P. Berens, and K. Wilson, ‘A Computer-Simulation Method fo the Calculation of Equilibrium-Constants for the Formation o Physical Clusters of Molecules - Application to Small Water Clusters’, *The Journal of Chemical Physics*, vol. 76, Jan. 1982.

[155] T. Liang *et al.*, ‘Reactive Potentials for Advanced Atomistic Simulations’, *Annu. Rev. Mater. Res.*, vol. 43, no. 1, pp. 109–129, 2013.

[156] G. Bourque and B. Terreault, ‘Low-energy random and channeled H ion ranges in Si: Measurements, simulation, and interpretation’, *Nucl. Instrum. Methods Phys. Res. Sect. B Beam Interact. Mater. At.*, vol. 140, no. 1, pp. 13–26, Apr. 1998.

[157] S. J. Plimpton and A. P. Thompson, ‘Computational aspects of many-body potentials’, *MRS Bull.*, vol. 37, no. 5, pp. 513–521, May 2012.

[158] A. V. Duin and S. R. Larter, ‘Application of molecular dynamics calculations in the prediction of dynamical molecular properties’, in *Organic Geochemistry*, 1998, vol. 29, pp. 1043–1050.

[159] A. C. T. van Duin and S. R. Larter, ‘Molecular dynamics investigation into the adsorption of organic compounds on kaolinite surfaces’, *Org. Geochem.*, vol. 32, no. 1, pp. 143–150, Jan. 2001.

[160] K. Chenoweth, A. C. T. van Duin, and W. A. Goddard, ‘ReaxFF Reactive Force Field for Molecular Dynamics Simulations of Hydrocarbon Oxidation’, *J. Phys. Chem. A*, vol. 112, no. 5, pp. 1040–1053, Feb. 2008.

[161] S.-Y. Kim, A. C. T. van Duin, and J. D. Kubicki, ‘Molecular dynamics simulations of the interactions between TiO2 nanoparticles and water with Na+ and Cl−, methanol, and formic acid using a reactive force field’, *J. Mater. Res.*, vol. 28, no. 3, pp. 513–520, Feb. 2013.

[162] S. Monti, A. C. T. van Duin, S.-Y. Kim, and V. Barone, ‘Exploration of the Conformational and Reactive Dynamics of Glycine and Diglycine on TiO2: Computational Investigations in the Gas Phase and in Solution’, *J. Phys. Chem. C*, vol. 116, no. 8, pp. 5141–5150, Mar. 2012.

[163] S. Huygh, A. Bogaerts, A. C. T. van Duin, and E. C. Neyts, ‘Development of a ReaxFF reactive force field for intrinsic point defects in titanium dioxide’, *Comput. Mater. Sci.*, vol. 95, pp. 579–591, Dec. 2014.

[164] T. Schneider and E. Stoll, ‘Molecular-dynamics study of a three-dimensional one-component model for distortive phase transitions’, *Phys. Rev. B*, vol. 17, no. 3, pp. 1302–1322, Feb. 1978.

[165] Y. Hiwatari, E. Stoll, and T. Schneider, ‘Molecular-dynamics investigation of solid–liquid coexistence’, *J. Chem. Phys.*, vol. 68, no. 8, pp. 3401–3404, Apr. 1978.

[166] H. J. C. Berendsen, J. P. M. Postma, W. F. van Gunsteren, A. D. Nola, and J. R. Haak, ‘Molecular dynamics with coupling to an external bath’, *J. Chem. Phys.*, vol. 81, no. 8, pp. 3684–3690, 1984.

[167] T. Schneider and E. Stoll, ‘Molecular-dynamics study of structural-phase transitions. I. One-component displacement models’, *Phys. Rev. B*, vol. 13, no. 3, pp. 1216–1237, Feb. 1976.

[168] Q. Hou, M. Hou, L. Bardotti, B. Prével, P. Mélinon, and A. Perez, ‘Deposition of Au-N clusters on Au(111) surfaces. I. Atomic-scale modeling’, *Phys. Rev. B*, vol. 62, no. 4, pp. 2825–2834, Jul. 2000.

[169] E. C. Neyts and A. Bogaerts, ‘Combining molecular dynamics with Monte Carlo simulations: implementations and applications’, *Theor. Chem. Acc.*, vol. 132, no. 2, p. 1320, Dec. 2012.

[170] C. Pangali, M. Rao, and B. J. Berne, ‘On a novel Monte Carlo scheme for simulating water and aqueous solutions’, *Chem. Phys. Lett.*, vol. 55, no. 3, pp. 413–417, May 1978.

[171] G. Dereli, ‘Stillinger-Weber Type Potentials in Monte Carlo Simulation of Amorphous Silicon’, *Mol. Simul.*, vol. 8, no. 6, pp. 351–360, Jan. 1992.

[172] C. H. Grein, R. Benedek, and T. de la Rubia, ‘Epitaxial growth simulation employing a combined molecular dynamics and Monte Carlo approach’, *Comput. Mater. Sci.*, vol. 6, no. 2, pp. 123–126, Aug. 1996.

[173] M. Timonova, J. Groenewegen, and B. J. Thijsse, ‘Modeling diffusion and phase transitions by a uniform-acceptance force-bias Monte Carlo method’, *Phys. Rev. B*, vol. 81, no. 14, p. 144107, Apr. 2010.

[174] E. C. Neyts, Y. Shibuta, A. C. T. van Duin, and A. Bogaerts, ‘Catalyzed Growth of Carbon Nanotube with Definable Chirality by Hybrid Molecular Dynamics−Force Biased Monte Carlo Simulations’, *ACS Nano*, vol. 4, no. 11, pp. 6665–6672, Nov. 2010.

[175] E. C. Neyts, A. C. T. van Duin, and A. Bogaerts, ‘Changing Chirality during Single-Walled Carbon Nanotube Growth: A Reactive Molecular Dynamics/Monte Carlo Study’, *J. Am. Chem. Soc.*, vol. 133, no. 43, pp. 17225–17231, Nov. 2011.

[176] M. J. Mees, G. Pourtois, E. C. Neyts, B. J. Thijsse, and A. Stesmans, 'Uniform-acceptance force-bias Monte Carlo method with time scale to study solid-state diffusion', *Phys. Rev. B*, vol. 85, no. 13, p. 134301, Apr. 2012.

[177] K. M. Bal and E. C. Neyts, 'On the time scale associated with Monte Carlo simulations', *J. Chem. Phys.*, vol. 141, no. 20, p. 204104, Nov. 2014.

[178] J. F. Ziegler and J. M. Manoyan, 'The stopping of ions in compounds', *Nucl. Instrum. Methods Phys. Res. Sect. B Beam Interact. Mater. At.*, vol. 35, no. 3, pp. 215–228, Dec. 1988.

[179] N. Laegreid and G. K. Wehner, 'Sputtering Yields of Metals for Ar+ and Ne+ Ions with Energies from 50 to 600 ev', *J. Appl. Phys.*, vol. 32, no. 3, pp. 365–369, Mar. 1961.

[180] T. Kubart, D. Depla, D. M. Martin, T. Nyberg, and S. Berg, 'High rate reactive magnetron sputter deposition of titanium oxide', *Appl. Phys. Lett.*, vol. 92, no. 22, p. 221501, Jun. 2008.

[181] T. Kubart, T. Nyberg, and S. Berg, 'Modelling of low energy ion sputtering from oxide surfaces', *Journal of Physics D : Applied Physics*, vol. 43, no. 20, 2010.

Résumé

Le procédé de pulvérisation cathodique magnétron est une technique de dépôt physique en phase vapeur (PVD pour Physical Vapour Deposition en anglais) utilisant des plasmas basse pression, aujourd'hui très employée dans l'industrie pour la synthèse de couches minces dans des domaines d'application tels que la mécanique, l'optique, l'électronique, le stockage de données ou également la décoration. Cette méthode consiste à produire une couche mince ou un film sur la surface d'un matériau, appelé 'substrat', afin de lui donner les propriétés du matériau pulvérisé, la 'cible'.

De nombreuses recherches ont porté sur la compréhension du phénomène mis en jeu lors du mécanisme de pulvérisation afin d'améliorer la production de couches minces en termes de composition, de qualité, des taux de pulvérisation et de déposition. Ainsi, la volonté de synthétiser des matériaux de plus en plus complexes en présence du plasma nécessite une compréhension du mécanisme à l'échelle atomique concernant la croissance du dépôt et les interactions plasma-surface qui ne peuvent être observées expérimentalement. Ces dernières peuvent cependant être étudiées par la Dynamique Moléculaire (DM), un outil numérique puissant dans la simulation à l'échelle microscopique permettant la description des interactions plasma-surface.

Pour compléter les mesures expérimentales, l'utilisation des simulations numériques a permis une meilleure compréhension des phénomènes de la décharge plasma et par conséquent de prédire différentes évolutions afin d'optimiser les conditions opératoires du procédé étudié.
Au GREMI (Groupe de Recherche sur l'Energétique des Milieux Ionisés), la technique de dépôt par pulvérisation magnétron est celle utilisée pour les études de croissance de couches minces.

Les travaux de cette thèse ont été réalisés au sein des groupes de recherche GREMI et PLASMANT (Plasma, Laser Ablation & Surface Modelling ANTwerp). L'objectif est de construire un model numérique multi-échelle, représentant un système complet de ce procédé, en couplant une approche fluide avec une approche microscopique par l'utilisation de la DM.

Ce manuscrit se compose de quatre chapitres :

Le premier chapitre introduit la pulvérisation cathodique magnétron et présente les différentes méthodes de simulation numérique utilisées pour décrire la décharge plasma et le mécanisme de pulvérisation.

Le second chapitre étudie la résolution d'un modèle fluide à deux dimension (r,z) et dépendant du temps, d'une décharge magnétron DC plane à symétrie cylindrique, à l'aide du logiciel COMSOL Multiphysics®.

Le troisième chapitre porte sur la pulvérisation d'une cible de titane (Ti) par des ions d'argon (Ar^+) par dynamique moléculaire ainsi que par combinaison MD/MC utilisant des simulations tfMC (pour time-stamped force-bias Monte Carlo en anglais) sur LAMMPS. La pulvérisation du titane est également étudiée incluant une phase gazeuse telle que dans une atmosphère neutre composée d'argon (Ar) et réactive composée d'oxygène (O) et d'un mélange argon-oxygène (50% Ar-50% O), ainsi qu'en considérant une cible chaude (1000 K et 2000 K).

Le quatrième et dernier chapitre résume les principaux résultats obtenus et présente d'éventuelles perspectives suite à ces travaux de thèse.

Chapitre 1

Les nombreuses recherches portées sur les plasmas et leurs propriétés ont permis de développer différentes techniques et applications telles que celle de la pulvérisation, utilisée pour le traitement de surface.

La méthode de pulvérisation consiste à appliquer un champ électrique entre deux électrodes dans un gaz à basse pression. Les électrons provenant de la cathode sont accélérés pour ioniser le gaz, habituellement composé d'argon. Ainsi, les collisions entre les électrons et les neutres créent des ions positifs d'argon qui vont être accélérés vers la cathode et impacter la cible. Suite aux impacts, des atomes qui composent la cible peuvent être libérés et se déposer sur le substrat pour former une couche.
Des électrons secondaires sont également créés par les impacts avec la cible et vont collisionner avec les neutres. Ces électrons secondaires permettent le maintient de la décharge plasma suivant un mécanisme d'avalanche électronique.

La pulvérisation cathodique magnétron utilise un système d'aimants permanents, placé sous la cible, généralement caractérisé par des lignes de champs qui se referment sur elles-mêmes afin de confiner les électrons près de la cathode. Les électrons sont 'piégés' par les lignes de champ permettant ainsi d'augmenter les collisions avec les neutres et par conséquent d'augmenter la production d'ions.
Le procédé de pulvérisation cathodique magnétron a montré de nombreux avantages tels que dans le contrôle de la composition et de la microstructure des couches déposées et des vitesses de déposition élevées. Il est alors intéressant de comprendre les mécanismes mis en jeu dans le système afin d'optimiser le procédé.

Plusieurs modèles 1D, 2D et 3D ont été développés selon différentes approches telles que des approches analytique, continue ou fluide, cinétique, particulaire, microscopique et également une approche hybride combinant différentes méthodes.
La modélisation complète du procédé de pulvérisation magnétron se compose de différentes parties incluant :

- le champ magnétique,
- la décharge magnétron,

- les interactions particules-cible et la pulvérisation,
- le transport des particules pulvérisées dans la phase gazeuse,
- la déposition et la croissance de la couche sur le substrat.

Ces dernières peuvent également être regroupées selon les modèles de la décharge magnétron et du mécanisme de pulvérisation et de déposition.

La modélisation de la décharge magnétron consiste à obtenir des informations sur les paramètres basics du plasma. Celle-ci inclue l'étude du potentiel électrique, de la densité du plasma, de la densité des particules chargées, et de leurs distributions en températures et en énergies dans le champ magnétique. Des modèles de la décharge magnétron ont été développés selon des approches continue ou fluide, cinétique, particulaire et hybride.
Parmi ces méthodes, le PIC/MCC (pour Particle-In-Cell Monte Carlo Collision en anglais), qui consiste au traitement individuel de chaque particule, est l'approche la plus utilisée malgré des temps de calculs très longs.
Très peu de modèles utilisent une approche continue ou fluide. En effet, l'application d'un champ magnétique fort peut rendre le modèle difficile à résoudre. De plus, l'applicabilité de l'approche fluide peut également être limitée par les basses pressions telles que le mTorr. Cependant la résolution d'un modèle fluide permet des temps de calcul moins long comparé à une approche particulaire.

La pulvérisation est décrite par un processus de collisions suite à un impact entre une particule incidente et la surface de la cible impliquant le déplacement des atomes de cette dernière suivant une cascade. Le phénomène de pulvérisation peut être décrit analytiquement ainsi que par des simulations numériques basées sur des modèles de BCA (pour Binary Collision Approximation en anglais) ou de DM.
La méthode BCA décrit la cascade de collisions comme une suite de collisions binaire indépendantes entre deux particules. Les simulations basées sur du calcul Monte Carlo ont un temps de calcul court et peuvent être appliquées à une grande échelle spatiale et temporelle.
Contrairement à la méthode BCA, la dynamique moléculaire permet de prendre en compte l'évolution du système durant le calcul. Les déplacements des particules ainsi que les changements de la cible sont alors conservés. Les calculs basés sur la MD correspondent à des temps allant de la femtoseconde à la nanoseconde, parfois la microseconde et restent limités

par la taille du modèle. En effet, un grand nombre de particules considéré dans le système nécessite un temps de calcul long.
Les résultats obtenus à partir de ces calculs permettent la détermination du taux de pulvérisation du matériau de la cible utilisée comme mesuré expérimentalement.

Chapitre 2

La première partie des travaux de cette thèse correspond à la partie macroscopique de notre modèle multi-échelles du procédé de pulvérisation cathodique magnétron par la modélisation de la décharge. L'objectif est d'obtenir des informations sur les paramètres plasma d'un réacteur réel avec un temps de calcul acceptable. Ainsi, nous nous intéressons à la modélisation d'une décharge magnétron, basée sur une méthode fluide à partir du modèle théorique des travaux de thèse de Costin, à l'aide du logiciel COMSOL Multiphysics®.

L'utilisation d'un logiciel commercial tel que COMSOL Multiphysics® permet de résoudre le modèle à partir d'un puissant solveur et également d'appliquer ce modèle sur différentes géométries telles que des géométries de réacteurs réels. Cependant, il n'est pas recommandé de simuler la décharge magnétron avec ce logiciel. Par conséquent nous avons choisi de basé notre modèle sur un modèle existant tel que celui de Costin. L'intérêt d'utiliser le model de Costin est qu'il présente, en plus d'une description détaillée du modèle, un certain nombre de résultats avec lesquels nous pourrons comparer nos résultats calculés et ainsi valider l'implémentation et la résolution du modèle avec COMSOL.

Le modèle fluide de la décharge magnétron consiste au traitement du transport des particules chargées et des neutres par la résolution des trois premiers moments de l'équation de Boltzmann couplés avec l'équation de Poisson :

- la continuité :

$$\frac{\partial n_s}{\partial t} + \nabla . \overrightarrow{\Gamma_s} = S_s$$

s correspond au type de particule ($s = e$ pour électron et i pour ion), n_s à la densité de particule, t au temps, $\overrightarrow{\Gamma_s} = n_s \overrightarrow{v_s}$ au flux de particule, $\overrightarrow{v_s}$ à la vitesse, et $S_s$au terme source.

- le transfert de mouvement :

$$m_s n_s \left[\frac{\partial \overrightarrow{v_s}}{\partial t} + (\overrightarrow{v_s}.\nabla)\overrightarrow{v_s}\right] = q_s n_s\left(\vec{E} + \overrightarrow{v_s} \times \vec{B}\right) - \nabla\overrightarrow{\overrightarrow{P_0}} - m_s n_s f_{ms}\overrightarrow{v_s}\left(1 + \frac{S_s}{n_s f_{ms}}\right)$$

m_s correspond à la masse, q_s à la charge de la particule, $\vec{E}$ au champ électrique, $\vec{B}$ au champ magnétique, $\overrightarrow{\overrightarrow{P_0}}$ au tenseur de pression et f_{ms} à la fréquence totale de transfert de mouvement pour la collision s-neutre.

- le transfert de l'énergie moyenne :

$$\frac{\partial(n_s\varepsilon_s)}{\partial t} + \nabla.\overrightarrow{\Gamma_{\varepsilon s}} = -\overrightarrow{\Gamma_s}.\vec{E} - \theta_s n_s$$

ε_s correspond à l'énergie moyenne, $\overrightarrow{\Gamma_{\varepsilon s}} = n_s\langle\varepsilon_s\overrightarrow{v_s}\rangle$ au flux d'énergie et θ_s: au taux de perte en énergie par collision s-neutre.

- équation de Poisson :

$$\Delta V = -\frac{e}{\varepsilon_0}(n_i - n_e)$$

V correspond au potentiel électrique, e à la constant de charge élémentaire et ε_0 à la permittivité du vide.

Le modèle de Costin, selon lequel nous nous basons, décrit une décharge magnétron plane DC dans l'argon d'un réacteur à symétrie cylindrique permettant une représentation 2D axis-symétrique du système.
Dans ce modèle, deux types de particules chargées sont traités, les électrons et les ions. La modélisation de la décharge dans une région proche de la cathode permet une représentation macroscopique des particules. Le transfert de l'énergie moyenne est calculé seulement pour les électrons. L'expression du flux des électrons est séparée en deux parties incluant un flux classique de dérive-diffusion et un flux contenant le champ magnétique. L'application d'un champ effectif permet l'expression classique de dérive-diffusion pour le flux des ions.

La résolution des équations est présentée selon deux études :

- une étude stationnaire pour le calcul du champ magnétique et
- une étude dépendante du temps pour le potentiel électrique et le transport des particules chargées.

Le modèle est caractérisé par des équations fortement non-linéaires et fortement couplées, rendant le modèle difficile à résoudre. Par conséquent, nous avons choisi d'étudier l'implémentation et la résolution de chacune des équations indépendamment.
Le champ magnétique ainsi que le potentiel électrique sont en bon accord avec les résultats présentés dans les travaux de Costin. La résolution du transport des particules présente cependant des limitations dans le calcul. Ceci peut être expliqué par la contribution d'un fort champ magnétique dans les équations de transport des électrons.

Chapitre 3

La seconde partie des travaux de cette thèse étudie la partie microscopique de notre modèle multi-échelles par la simulation du mécanisme de pulvérisation avec des codes LAMMPS (pour Large-Atomic/ Molecular Massively Parallel Simulator) à partir d'un modèle basé sur la DM, ainsi que par un modèle hybride combinant la DM et des calculs Monte Carlo, selon la méthode tfMC.

La méthode de dynamique moléculaire consiste à la résolution des équations de Newton pour chaque particule du système :

$$\overrightarrow{F_i} = m_i \overrightarrow{a_i} = m_i \frac{d\overrightarrow{v_i}}{dt} = m_i \frac{d^2\overrightarrow{r_i}}{dt^2}$$

$\overrightarrow{F_i}$ correspond à la force appliqué sur un atome i, m_i à la masse de l'atome, $\overrightarrow{a_i}$ à l'accélération, $\overrightarrow{v_i}$ à la vitesse et $\overrightarrow{r_i}$ à la position

Les résultats obtenus dépendent de la précision du potentiel interatomique ou du champ de force utilisé dans les simulations. De plus, pour décrire correctement le système de pulvérisation, des conditions particulières doivent être respectée. Ces conditions concernent l'application d'un thermostat utilisé pour dissiper l'énergie transmise par les ions incidents,

accumulée dans la cible et le temps de relaxation de la cible. La combinaison des simulations DM/tfMC permet de considérer un temps de relaxation de la cible plus long avec un temps de calcul court comparé à la DM.

Pour ces simulations, nous avons choisi de travailler avec une cible pure de titane. Le titane est un matériau intéressant par les différentes propriétés qu'il contient. Les couches minces composées de titane, telles que les oxydes de titanes (TiO_x) et nitrures de titanes (TiN_x) ont montré des propriétés intéressantes pour des champs d'application tels que l'optique, l'électronique, la mécanique ou également la décoration.

Dans ce chapitre, nous nous intéressons à la détermination des taux de pulvérisation et de rétention obtenus pour trois énergies d'ions incidents considérées (200, 300 et 400 eV), selon différentes études :

- la première étude compare les calculs basés sur la DM à des calculs de MD /tfMC pour la pulvérisation du titane par des ions d'argon
- dans la seconde étude, la pulvérisation non-réactive est comparée à la pulvérisation réactive avec l'ajout d'une phase gazeuse dans la boîte de simulation contenant alors trois types de gaz composés d'atomes d'argon, d'une mixture d'argon et d'oxygène (50% Ar – 50% O) et d'atomes d'oxygène.
- la troisième étude introduit l'utilisation d'une cible chaude avec deux températures élevées (1000 et 2000 K).

Les taux pulvérisations du titane résultants de la première étude sont également comparés aux résultats de simulations TRIM, du calcul de la formule de Yamamura ainsi qu'avec les réultats expérimentaux obtenus par Laegreid et Wehner. Les taux de rétention de l'argon sont comparés avec les simulations TRIM.
Les taux de pulvérisations obtenus sont proches des différents résultats présentés et les taux de rétention reste en dessous de ceux calculés avec TRIM.
Dans la seconde étude, les taux de pulvérisation obtenus sont plus faibles que ceux de la première étude due à la présence de la phase gazeuse qui peut avoir un effet sur la vitesse des ions. De plus, des taux de pulvérisation anormalement élevés ont également été obtenus dans le cas de pulvérisation réactive selon les simulations de dynamique moléculaire. En effet, la présence d'oxygène conduit normalement à la formation d'oxydes de titane qui couvrent la

cible et diminue les taux de pulvérisation. Cependant nos résultats peuvent être expliqués par la formation de faibles oxydes de titanes conduisant à des taux de pulvérisation élevés.
Les taux de pulvérisations calculés dans le cas de cible chaudes à 1000 et 2000 K, dans la troisième étude, présentent pour la plupart des simulations des taux de pulvérisation et de rétention supérieurs à ceux obtenus pour une température de la cible à 300 K.

Chapitre 4

L'objectif de cette thèse intitulée « Simulation numérique multi-échelles du procédé de dépôt par pulvérisation cathodique magnétron », consiste au développement d'une modèle simulant la pulvérisation cathodique magnétron dans un réacteur plasma en reliant une approche fluide, pour le modèle macroscopique de la décharge magnétron, et la dynamique moléculaire, pour la description microscopique du mécanisme de pulvérisation.
La simulation de la décharge magnétron par une approche fluide est basée sur le transport des espèces et permet d'obtenir des paramètres d'entrée pour les simulations de dynamique moléculaire qui s'intéressent aux taux de pulvérisation et aux fonctions de distribution des espèces pulvérisées, ainsi qu'à la croissance du dépôt.

Dans le **Chapitre 2**, la résolution du modèle de la décharge magnétron basé sur le modèle théorique de Costin a montré une bonne résolution du champ magnétique et de l'équation de Poisson pour la détermination du potentiel électrique. Des limitations dans le calcul du transport des électrons et des ions ont également été rencontrées durant nos calculs avec COMSOL Multiphysics®. Le solveur du logiciel COMSOL Multiphysics® est notamment caractériser comme une boîte noire et il est alors difficile de faire certains ajustements pour aider le modèle à converger correctement.
De plus, la modélisation d'une décharge magnétron utilisant une approche fluide est aujourd'hui encore discutable dans le cas de basses pressions et de forts champs magnétiques.
Notre intérêt d'utiliser ce type d'approche reste d'obtenir les paramètres du plasma avec un temps de calcul acceptable comparé à des simulations Monte Carlo.

Dans la continuité de ces travaux, il pourrait être intéressant d'utiliser d'autres types de solveur pouvant résoudre des modèles d'approche continue.

Le logiciel COMSOL évoluant régulièrement, les prochaines versions du logiciel pourront peut-être permettre de résoudre des systèmes non-linéaires comme le présente ce modèle.

Dans le **Chapitre 3**, la dynamique moléculaire est un outil puissant pour la description des interactions plasma-surface. Ainsi, nous étudions la pulvérisation du titane par des impacts d'ions d'argon selon différents modèles et les deux méthodes de calcul basées sur la DM et l'approche hybride combinant la DM aux simulations tfMC.
La comparaison des simulations DM et DM/tfMC a permis de valider l'application de l'approche hybride pour notre modèle.
De plus, dans le cas de la simulation de la pulvérisation du titane par les ions d'argon, les taux de pulvérisation du titane sont proches des résultats obtenus avec d'autres méthodes.
L'introduction d'une phase gazeuse a un effet sur la vitesse des ions incidents et par conséquent sur le taux de pulvérisation résultant.
La pulvérisation réactive du titane montre un taux élevé de pulvérisation du titane dans le cas des simulations de dynamique moléculaire.
Les taux de pulvérisation et de rétention obtenus dans le cas d'une cible chaude sont supérieurs comparés à une cible à 300 K.

La suite de ces travaux serait de compléter les résultats obtenus selon un plus grand nombre d'impacts considérés afin d'obtenir des valeurs plus précises des taux de pulvérisation et de rétention et également d'étudier la distribution en énergie des atomes pulvérisés.
Il serait intéressant de travailler selon des énergies des énergies plus basses et plus fortes et d'autres températures de cible élevées correspondantes aux valeurs expérimentales.
La prise en compte du nombre de collisions contenues dans la phase gazeuse peut nous permettre d'obtenir un model proche de la réalité.
Finalement, le procédé de déposition pourrait être ajouté au model afin d'obtenir un model complet du mécanisme de pulvérisation et de déposition du titane.

Sotheara CHUON

Simulation numérique multi-échelles du procédé de dépôt par pulvérisation cathodique magnétron

Résumé :
Le procédé de pulvérisation cathodique magnétron est un procédé utilisant des plasmas basse pression, très employé pour la synthèse de couches minces dans l'industrie. De nombreuses recherches ont porté sur la compréhension des phénomènes mis en jeu dans le mécanisme de pulvérisation dans le but d'améliorer le procédé. Les simulations numériques associées à des résultats expérimentaux permettent aujourd'hui une meilleure compréhension des phénomènes de la décharge plasma et par conséquent de prédire différente évolution du système afin d'optimiser les conditions opératoires du procédé.
L'objectif de cette thèse est de construire un modèle multi-échelles du procédé de pulvérisation cathodique magnétron en couplant une approche fluide avec une approche microscopique basée sur la Dynamique Moléculaire (DM).
La première partie étudie la résolution du modèle fluide d'une décharge magnétron DC plane à partir du modèle théorique de Costin, afin de déterminer des paramètres d'entrée pour les simulations de dynamique moléculaire.
Les résultats du champ magnétique et du potentiel électrique sont en bon accord avec ceux présentés par Costin. Cependant le calcul du transport des espèces a montré des limitations.
La seconde partie s'intéresse à la pulvérisation du titane (Ti) par des ions d'argon (Ar^+) pour trois énergies considérées (200, 300 et 400 eV) dans une atmosphère neutre et une atmosphère réactive, ainsi qu'en reproduisant des cibles chaudes (1000 et 2000 K) par des simulations de DM et en combinant avec des simulations Monte Carlo.
Les résultats obtenus ont ainsi permis la détermination de taux de pulvérisation du titane et de rétention de l'argon.

Mots clés : Simulation multi-échelles, CFD, Dynamique Moléculaire, Plasma, Magnétron

Multiscale modelling of cathodic magnetron sputtering

Summary:
Cathodic magnetron sputtering is a low pressure plasma process, very employed for the synthesis of coatings by industries. Numerous researches have been focused on understanding the phenomena involved in sputtering mechanism to improve the process. Numerical simulations associated with experimental results allow today a better understanding of the plasma discharge phenomena and thus to predict evolutions of the system in order to optimize the operating conditions of the process.
The goal of this thesis is to build a multiscale model of magnetron sputtering process by coupling fluid approach with microscopic approach based on Molecular Dynamics (MD).
The first part studies the solving of the fluid model of a DC planar magnetron discharge from the theoretical model of Costin, in order to determine the input parameters for the molecular dynamics simulations.
The results of the magnetic field and the electric potential are in good agreement with those presented by Costin. Nevertheless, the calculation of the particle transport showed limitations.
The second part is interested in the sputtering of titanium (Ti) by argon ions (Ar^+) for three considered energies (200, 300 and 400 eV) in neutral atmosphere and in reactive atmosphere, also by mimicking hot targets (1000 and 2000 K) by MD simulations and by combining with Monte Carlo simulations.
The obtained results thus allowed the determination of titanium sputtering yields and argon retention rates.

Keywords: Multiscale simulation, CFD, Molecular Dynamics, Plasma, Magnetron

Groupe de Recherches sur l'Energetique des Milieux Ionisés
14 rue d'Issoudun BP6744 - 45067 Orléans Cedex 2, France

Plasma, Laser Ablation and Surface Modelling – ANTwerp
University of Antwerp, Dept. Chemistry - Campus Drie Eiken
Universiteitsplein 1 - 2610 Antwerpen-Wilrijk, Belgium